

AD-A035 478

XONICS INC VAN NUYS CALIF
RESEARCH ON CRYSTAL CHEMISTRY STUDIES.(U)
NOV 76 M SPARKS, C J DUTHLER

F/6 7/4

UNCLASSIFIED

RADC-TR-76-343

F19628-75-C-0123
NL

1 OF 2
AD
A035478



ADA035478

RADC-TR-76-343
FINAL TECHNICAL REPORT
30 NOVEMBER 1976

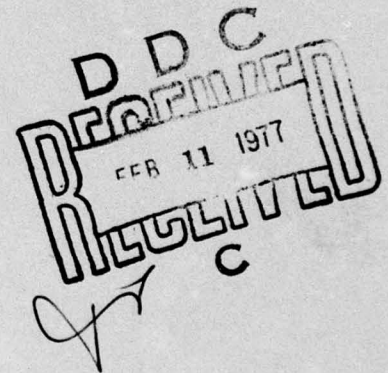
12



RESEARCH ON CRYSTAL CHEMISTRY STUDIES

XONICS, INCORPORATED
VAN NUYS, CALIFORNIA 91406

APPROVED FOR PUBLIC RELEASE;
DISTRIBUTION UNLIMITED

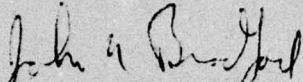


ROME AIR DEVELOPMENT CENTER
AIR FORCE SYSTEMS COMMAND
GRIFFISS AIR FORCE BASE, NEW YORK 13441

COPY AVAILABLE TO DDC DOES NOT
PERMIT FULLY LEGIBLE PRODUCTION

This report has been reviewed by the RADC Information Office (OI) and is releasable to the National Technical Information Service including foreign nations.

This technical report has been reviewed and is approved.


JOHN N. BRADFORD
Contract Monitor

Unclassified

SECURITY CLASSIFICATION OF THIS PAGE (When Data Entered)

19 REPORT DOCUMENTATION PAGE		READ INSTRUCTIONS BEFORE COMPLETING FORM	
1. REPORT NUMBER RADC-TR-76-343	2. GOVT ACCESSION NO.	3. RECIPIENT'S CATALOG NUMBER	
4. TITLE (and Subtitle) RESEARCH ON CRYSTAL CHEMISTRY STUDIES		5. TYPE OF REPORT & PERIOD COVERED Final Report - Period 28 March 1975 through 30 June 1976	
7. AUTHOR(s) M. Sparks and C. J. Duthler		8. CONTRACT OR GRANT NUMBER(s) F19628-75-C-0123	
9. PERFORMING ORGANIZATION NAME AND ADDRESS Xonics, Inc. 6849 Hayvenhurst Avenue Van Nuys, California 91406		10. PROGRAM ELEMENT, PROJECT, TASK AREA & WORK UNIT NUMBERS 61102F 56200911	
11. CONTROLLING OFFICE NAME AND ADDRESS Deputy for Electronic Technology (RADC) Hanscom AFB, Massachusetts 01731 Monitor/ETSP/John Larkin		12. REPORT DATE 30 November 1976	
14. MONITORING AGENCY NAME & ADDRESS (if different from Controlling Office)		13. NUMBER OF PAGES 159	
15. SECURITY CLASS. (of this report) Unclassified		15a. DECLASSIFICATION/DOWNGRADING SCHEDULE	
16. DISTRIBUTION STATEMENT (of this Report) A - Approved for public release; distribution unlimited.			
17. DISTRIBUTION STATEMENT (of the abstract entered in Block 20, if different from Report)			
18. SUPPLEMENTARY NOTES Work partially supported by SAMSO.			
19. KEY WORDS (Continue on reverse side if necessary and identify by block number) Scattering, Cohesion, Coatings			
20. ABSTRACT (Continue on reverse side if necessary and identify by block number) The cohesion and light scattering properties of metallic spheres have been examined. Preliminary results for the cohesion of coated spheres, obtained during the present contractual period, are: (1) The dominant mechanism for sphere cohesion is molecular binding with the cohesive force being dependent on the chemical bonding mechanism of the sphere material or the coating material for coated spheres. Molecular binding is expected to be greatest for pure metal surfaces and smallest for spheres coated with nonpolar molecular solids with oxidized metals having intermediate strength binding.			

DD FORM 1 JAN 73 1473 EDITION OF 1 NOV 65 IS OBSOLETE

Unclassified

SECURITY CLASSIFICATION OF THIS PAGE (When Data Entered)

* discussed

406514

1B

Unclassified

SECURITY CLASSIFICATION OF THIS PAGE(When Data Entered)

(2) An examination of the spatial range of the molecular binding forces indicates that a uniform coating one or two molecular layers thick is sufficient to saturate the molecular forces so that the cohesion is determined entirely by the coating. (3) Binding from capillary forces of a liquid bridge linking two spheres, if it occurs, is comparable to, or greater than, molecular attractive forces. However, such liquid bridges may not be formed under the experimental conditions of interest. (4) Electrostatic binding appears to be negligible except under special circumstances or for statistically few particles in a large collection. (5) Desirable coating materials are fatty acids, such as stearic acid, and fluorinated hydrocarbons and polymers, such as teflon. Light scattering from metallic spheres coated with various nonabsorbing and absorbing coatings has been calculated with dispersion included in the optical constants of both the metallic core and the absorbing coatings. The principal results of this study are: (1) The scattering from an uncoated metallic sphere is, on the average, within three percent of the scattering from a perfectly conducting sphere of the same radius. (2) For a broad range of coating thicknesses and refractive indices greater than approximately 1.6, the scattering from the coated sphere is similar to that from a perfectly conducting sphere having a radius equal to the total of the metallic sphere radius plus the coating thickness. (3) With thin coatings the change in the scattering due to the coating is linear in the coating thickness and less than three percent for coatings having a ratio of the total coated sphere radius to the core sphere radius equal to 1.004. (4) Absorption bands in coating materials have been investigated by the use of Lorentzian lines of varying linewidths. A Lorentzian absorption line results in a localized perturbation in the scattering curve with the width of the perturbation approximately equal to the absorption linewidth and the magnitude of the perturbation determined by the coating thickness. (5) Scattering from an actual metal-oxide coating has been examined. Large magnitude localized deviations in the scattering curve are observed at points where the real part of the coating refractive index is small and the imaginary part is large. (6) Scattering from small dielectric particles is less efficient than from metallic particles of the same size. A localized valley in the scattering is found at a point where the imaginary part of the refractive index changes abruptly from one slowly varying value to another.

Form with fields for:

- ATC
- NTS
- U.C.
- REMARKS
- JUSTIFICATION
- BY
- DISTRIBUTION AVAILABILITY CODES
- U.S.C.
- MAIL
- END OF SPECIAL
- Large letter 'A' in a box


Unclassified

SECURITY CLASSIFICATION OF THIS PAGE(When Data Entered)

EVALUATION

1. This report is the Final Technical Report on the contract. It covers theoretical research done on mechanisms for particle agglomeration and optical scattering. The objective of the research was to establish the nature of the most probable cohesive forces between small particles and to predict techniques with which these cohesive forces could be minimized. This involved calculating the effect of thin coatings and intermixed particles on the optical scattering spectra of spherical particles. Since the most likely attractive force between the particles arises from molecular interactions, the contractor recommended either thin coatings of a van der Waals bonded solid such as stearic acid or admixtures of even smaller spacer particles to prevent the scattering particles from coming into physical contact. Extensive calculations showed that neither solution would extensively affect the optical scattering spectrum. Experiments at RADC/ET support these results.

2. The above work is of value since it provides a model of particle interactions and particle/light interactions necessary to optimize materials for Penaid's ECM/ECCM applications.


JOHN J. LARKIN
Contract Monitor
Solid State Sciences Division

SUMMARY OF RESULTS

An analysis of the mechanisms for the cohesion of small metallic particles suggests that the binding of metallic particles can be reduced by coating with one of several different dielectric materials. The effects of dielectric coatings on the light-scattering properties of metallic spheres is determined.

Mechanisms for the cohesion of particles can be divided into three categories: (1) If two particles are linked by a liquid bridge that wets both particles, the surface tension of the liquid can yield an attractive force between the particles. (2) Two particles in close proximity experience molecular attraction and molecular binding. The cold-welding of metals at points of intimate contact is an example. (3) Electrically charged particles are attracted to oppositely charged particles and to image charges in uncharged particles.

The principal results of the cohesion study are:

- The molecular-attraction mechanism appears to be the dominant mechanism, with the strength of the binding dependent on the chemical-bonding mechanism appropriate to the coating material. Pure metals are expected to have the largest binding forces, and nonpolar molecular solids the smallest. Intuitively, covalent and ionic materials, such as metal oxides, are expected to have binding forces that are sensitive to the alignment of the lattices on the two particles and, hence, to have intermediate strength forces.
- The range of molecular forces has been examined. It is estimated that a uniform coating one or two molecular layers in thickness should be sufficient to saturate the forces so that the cohesion is determined entirely by the coating rather than the core.
- The electrostatic binding mechanism appears to be negligible except under such special circumstances as those in a corona discharge or for statistically few particles in a large collection of particles.

- Attractive forces from the liquid-bridge mechanism, if it occurs, are greater than the molecular-attraction mechanism. However, liquid bridges may not be formed under the experimental conditions of interest since negative pressures (tensile forces) within the liquid are predicted for a broad range of particle sizes and wetting angles.

Coating materials should be hygrophobic and should have nonpolar molecular binding. These conditions are satisfied by several polymers, of which such fluorinated hydrocarbons as teflon are notable because of their small polarizabilities and resulting small binding forces. Another group of desirable materials is the fatty-acid group including stearic acid. These acids are long, linear molecules having one reactive end and an inert tail. Under favorable reaction conditions, these acids form an aligned monomolecular layer on metal substrates, with the inert nonpolar tails aligned normal to the surface.

Light scattering from metallic spheres coated with various absorbing and non-absorbing coatings has been examined qualitatively and quantitatively. The present study is of scattering from actual metallic spheres, in contrast to previous studies which considered perfectly conducting spheres. The use of an actual metal is necessary because the effects of many coatings are less than the differences between a metal and a perfect conductor. Means of overcoming the difficulties that arise in the Mie-theory calculation of an actual metal and descriptions of the calculation procedure are given in the body and appendices of this report. The principal results of the light-scattering study are:

- The scattering efficiency of an uncoated metallic sphere is, on the average, within three percent of that for a perfectly conducting sphere of the same radius. In the wavelength range of interest, the maximum deviation is less than ten percent.
- With nondispersive absorbing and transparent coatings having refractive indices greater than approximately 1.6, the scattering is qualitatively similar to that from a perfectly conducting sphere having a radius equal to the total of the core sphere radius plus the coating thickness. With smaller magnitude coating refractive indices, the scattering is better approximated by that from a perfectly conducting sphere having the core radius.

- Quantitative effects of nondispersive coatings were evaluated by calculating the root-mean-square percent (RMS %) deviation of the coated metallic sphere from the uncoated metallic sphere over a portion of the scattering range. With thin coatings, the RMS % deviation is linear in the coating thickness at a fixed refractive index. For coating refractive indices in the range from approximately 1.6 to 4.0, the RMS % deviation is insensitive to the refractive index and is less than 0.3 % for a radius ratio of the coated to the uncoated sphere of 1.0004. For thicker coatings having radius ratios 1.004 and 1.04, the RMS % deviations are less than 3% and 30%, respectively.
- Dispersive absorption bands were investigated by considering a model coating having a single Lorentzian absorption line of various frequencies and various linewidths. The absorption lines result in localized deviations in the scattering curve centered approximately one linewidth toward higher frequencies from the absorption line and having a width comparable to the absorption linewidth. The shape of the localized deviation is primarily dependent on the absorption frequency and is a localized valley near the first maximum in the scattering curve, a localized shoulder near the midpoint between the first maximum and first minimum, and a localized peak near the first minimum. For an absorption coefficient of 10^4 cm^{-1} at the line center and a radius ratio of 1.04, the localized deviations have a magnitude of approximately 10 % of the local value of the scattering.
- Scattering from an actual metal-oxide coating was examined. The localized deviations in the scattering curve do not correlate well with the absorption bands in the coating. Rather, the most severe effects occur at points where the real part of the refractive index is small and the imaginary part is large.
- Scattering from homogeneous dielectric particles smaller in size than the primary particles was examined. On the average the scattering is less efficient than from metallic particles of the same size. There is one localized valley in the scattering curve at a point where the real part of the refractive index is slowly varying and the imaginary part changes abruptly from one slowly varying value to another.

PREFACE

This final report covers research on crystal chemistry studies performed on Contract No. F19628-75-C-0123 during the period from March 28, 1975 through June 30, 1976. The following investigators contributed to the research: Dr. M. Sparks, principal investigator; Dr. C. J. Duthler, research scientist; Dr. R. Sherman, research associate; and Mr. M. Flannery, research associate.

TABLE OF CONTENTS

<u>Section</u>		<u>Page</u>
	SUMMARY OF RESULTS.....	1
	PREFACE.....	4
I	INTRODUCTION	13
II	COHESION MECHANISMS	14
	A. Liquid Bridge.....	14
	B. Electrostatic.....	24
	C. Molecular Attraction	29
	D. Summary and Conclusions of Cohesion Study.....	37
III	LIGHT SCATTERING FROM COATED SPHERES	42
	A. Theory.....	42
	B. Practical Computational Considerations	48
	C. Tests of Program Accuracy	55
	D. Results.....	58
	E. Summary and Conclusions of Scattering Study	119
	REFERENCES.....	127
Appendix A	DESCRIPTION OF THE SUBROUTINES AND THEIR FUNCTION	129
Appendix B	INPUT DATA CARD DESCRIPTION	132
Appendix C	LIST OF VARIABLES	136
Appendix D	COMPUTER CODE LISTINGS	139

LIST OF ILLUSTRATIONS

<u>Figure</u>	<u>Title</u>	<u>Page</u>
2.1	Two spheres of radius a wet by a liquid out to an angle θ from the line connecting the sphere centers. The liquid has a contact angle ϕ with the sphere surfaces and has a radius of curvature r .	15
2.2	Dependence of the liquid pressure differential on wetting angle.	18
2.3	Dependence of the attractive force components on wetting angle.	20
2.4	Dependence of the critical wetting angle on sphere radius.	21
2.5	Dependence of the liquid-bridge attractive forces on sphere radius.	22
2.6	A charge of magnitude ne at a distance of $2a$ from a conducting sphere of radius a , induces an image charge of magnitude $-ne/2$ in the conducting sphere.	27
2.7	Dependence of the molecular attractive force on coating thickness.	32
2.8	Separation h of the sphere surfaces at a distance ρ from the line between sphere centers.	35
2.9	Comparison of cohesion mechanisms.	38
2.10	Aligned monolayer of fatty acid.	41
3.1	Radiation propagating in the z direction is scattered from a spherically symmetric object at the origin to the observation point (r, θ, ϕ) .	43
3.2	Coated sphere having core radius, a , and total radius, b .	47
3.3	Magnitude of the electric-multipole scattering coefficients a_n of a perfectly conducting sphere as a function of the sphere size parameter ka .	49
3.4	Magnitude of the magnetic-multipole scattering coefficients b_n of a perfectly conducting sphere as a function of the sphere size parameter ka .	50
3.5	Comparison of the scattering from a perfectly conducting sphere (symbols) and a metallic sphere (solid curve).	60

LIST OF ILLUSTRATIONS (Cont'd)

<u>Figure</u>	<u>Title</u>	<u>Page</u>
3.6	Scattering from a coated metallic sphere normalized to the total cross-sectional area (solid curve) and scattering from a perfectly conducting sphere of radius b (symbols).	62
3.7	Scattering from a coated metallic sphere normalized to the core cross-sectional area (solid curve) and scattering from a perfectly conducting sphere of radius a (symbols).	63
3.8	Scattering from a coated metallic sphere normalized to the total cross-sectional area (solid curve) and scattering from a perfectly conducting sphere of radius b (symbols).	64
3.9	Scattering from a coated metallic sphere normalized to the core cross-sectional area (solid curve) and scattering from a perfectly conducting sphere of radius a (symbols).	65
3.10	Scattering from a coated metallic sphere normalized to the total cross-sectional area (solid curve) and scattering from a perfectly conducting sphere of radius b (symbols).	66
3.11	Scattering from a coated metallic sphere normalized to the core cross-sectional area (solid curve) and scattering from a perfectly conducting sphere of radius a (symbols).	67
3.12	Scattering from a coated metallic sphere normalized to the total cross-sectional area (solid curve) and scattering from a perfectly conducting sphere of radius b (symbols).	68
3.13	Scattering from a coated metallic sphere normalized to the core cross-sectional area (solid curve) and scattering from a perfectly conducting sphere of radius a (symbols).	69
3.14	Scattering from a coated metallic sphere normalized to the total cross-sectional area (solid curve) and scattering from a perfectly conducting sphere of radius b (symbols).	70
3.15	Scattering from a coated metallic sphere normalized to the core cross-sectional area (solid curve) and scattering from a perfectly conducting sphere of radius a (symbols).	71
3.16	Scattering from a coated metallic sphere normalized to the total cross-sectional area (solid curve) and scattering from a perfectly conducting sphere of radius b (symbols).	72

LIST OF ILLUSTRATIONS (Cont'd)

<u>Figure</u>	<u>Title</u>	<u>Page</u>
3.17	Scattering from a coated metallic sphere normalized to the core cross-sectional area (solid curve) and scattering from a perfectly conducting sphere of radius a (symbols).	73
3.18	Scattering from a coated metallic sphere normalized to the total cross-sectional area (solid curve) and scattering from a perfectly conducting sphere of radius b (symbols).	74
3.19	Scattering from a coated metallic sphere normalized to the core cross-sectional area (solid curve) and scattering from a perfectly conducting sphere of radius a (symbols).	75
3.20	Scattering from a coated metallic sphere normalized to the total cross-sectional area (solid curve) and scattering from a perfectly conducting sphere of radius b (symbols).	78
3.21	Scattering from a coated metallic sphere normalized to the core cross-sectional area (solid curve) and scattering from a perfectly conducting sphere of radius a (symbols).	79
3.22	Scattering from a coated metallic sphere normalized to the total cross-sectional area (solid curve) and scattering from a perfectly conducting sphere of radius b (symbols).	80
3.23	Scattering from a coated metallic sphere normalized to the core cross-sectional area (solid curve) and scattering from a perfectly conducting sphere of radius a (symbols).	81
3.24	Scattering from a coated metallic sphere normalized to the total cross-sectional area (solid curve) and scattering from a perfectly conducting sphere of radius b (symbols).	82
3.25	Scattering from a coated metallic sphere normalized to the core cross-sectional area (solid curve) and scattering from a perfectly conducting sphere of radius a (symbols).	83
3.26	Scattering from a coated metallic sphere normalized to the total cross-sectional area (solid curve) and scattering from a perfectly conducting sphere of radius b (symbols).	84
3.27	Scattering from a coated metallic sphere normalized to the core cross-sectional area (solid curve) and scattering from a perfectly conducting sphere of radius a (symbols).	85

LIST OF ILLUSTRATIONS (Cont'd)

<u>Figure</u>	<u>Title</u>	<u>Page</u>
3.28	Scattering from a coated metallic sphere normalized to the total cross-sectional area (solid curve) and scattering from a perfectly conducting sphere of radius b (symbols).	86
3.29	Scattering from a coated metallic sphere normalized to the core cross-sectional area (solid curve) and scattering from a perfectly conducting sphere of radius a (symbols).	87
3.30	Root-mean-square percent deviation of the scattering of a coated metallic sphere from that of the uncoated sphere as a function of the coating refractive index for various coating thicknesses.	90
3.31	Contours of constant root-mean-square percent deviation of the scattering of a coated metallic sphere from that of the uncoated sphere as a function of the coating thickness and coating refractive index.	92
3.32	Real part ϵ_R and imaginary part ϵ_I of the dielectric constant of a coating having a Lorentzian absorption line with a full width at half maximum of 50 cm^{-1} (a). Scattering from a coated metallic sphere in the vicinity of the absorption line (b).	94
3.33	Real part ϵ_R and imaginary part ϵ_I of the dielectric constant of a coating having a Lorentzian absorption line with a full width at half maximum of 20 cm^{-1} (a). Scattering from a coated metallic sphere in the vicinity of the absorption line (b).	95
3.34	Real part ϵ_R and imaginary part ϵ_I of the dielectric constant of a coating having a Lorentzian absorption line with a full width at half maximum of 10 cm^{-1} (a). Scattering from a coated metallic sphere in the vicinity of the absorption line (b).	96
3.35	Scattering from a coated metallic sphere having a 10 cm^{-1} fwhm absorption line at $ka = 1.01$ (solid curve). Results are normalized to the core cross-sectional area and compared to a perfectly conducting sphere of radius b (symbols).	97
3.36	Scattering from a coated metallic sphere having a 10 cm^{-1} fwhm absorption line at $ka = 1.12$ (solid curve). Results are normalized to the core cross-sectional area and compared to a perfectly conducting sphere of radius b (symbols).	98
3.37	Scattering from a coated metallic sphere having a 10 cm^{-1} fwhm absorption line at $ka = 1.26$ (solid curve). Results are normalized to the core cross-sectional area and compared to a perfectly conducting sphere of radius b (symbols).	99

LIST OF ILLUSTRATIONS (Cont'd)

<u>Figure</u>	<u>Title</u>	<u>Page</u>
3.38	Scattering from a coated metallic sphere having a 10 cm^{-1} fwhm absorption line at $ka = 1.43$ (solid curve). Results are normalized to the core cross-sectional area and compared to a perfectly conducting sphere of radius b (symbols).	100
3.39	Scattering from a coated metallic sphere having a 10 cm^{-1} fwhm absorption line at $ka = 1.65$ (solid curve). Results are normalized to the core cross-sectional area and compared to a perfectly conducting sphere of radius b (symbols).	101
3.40	Scattering from a coated metallic sphere having a 20 cm^{-1} fwhm absorption line at $ka = 1.01$ (solid curve). Results are normalized to the core cross-sectional area and compared to a perfectly conducting sphere of radius b (symbols).	102
3.41	Scattering from a coated metallic sphere having a 20 cm^{-1} fwhm absorption line at $ka = 1.12$ (solid curve). Results are normalized to the core cross-sectional area and compared to a perfectly conducting sphere of radius b (symbols).	103
3.42	Scattering from a coated metallic sphere having a 20 cm^{-1} fwhm absorption line at $ka = 1.26$ (solid curve). Results are normalized to the core cross-sectional area and compared to a perfectly conducting sphere of radius b (symbols).	104
3.43	Scattering from a coated metallic sphere having a 20 cm^{-1} fwhm absorption line at $ka = 1.43$ (solid curve). Results are normalized to the core cross-sectional area and compared to a perfectly conducting sphere of radius b (symbols).	105
3.44	Scattering from a coated metallic sphere having a 20 cm^{-1} fwhm absorption line at $ka = 1.65$ (solid curve). Results are normalized to the core cross-sectional area and compared to a perfectly conducting sphere of radius b (symbols).	106
3.45	Scattering from a coated metallic sphere having a 50 cm^{-1} fwhm absorption line at $ka = 1.01$ (solid curve). Results are normalized to the core cross-sectional area and compared to a perfectly conducting sphere of radius b (symbols).	107
3.46	Scattering from a coated metallic sphere having a 50 cm^{-1} fwhm absorption line at $ka = 1.12$ (solid curve). Results are normalized to the core cross-sectional area and compared to a perfectly conducting sphere of radius b (symbols).	108

LIST OF ILLUSTRATIONS (Cont'd)

<u>Figure</u>	<u>Title</u>	<u>Page</u>
3.47	Scattering from a coated metallic sphere having a 50 cm^{-1} fwhm absorption line at $ka = 1.26$ (solid curve). Results are normalized to the core cross-sectional area and compared to a perfectly conducting sphere of radius b (symbols).	109
3.48	Scattering from a coated metallic sphere having a 50 cm^{-1} fwhm absorption line at $ka = 1.43$ (solid curve). Results are normalized to the core cross-sectional area and compared to a perfectly conducting sphere of radius b (symbols).	110
3.49	Scattering from a coated metallic sphere having a 50 cm^{-1} fwhm absorption line at $ka = 1.65$ (solid curve). Results are normalized to the core cross-sectional area and compared to a perfectly conducting sphere of radius b (symbols).	111
3.50	Scattering from a coated metallic sphere having a 10 cm^{-1} fwhm absorption line (solid curve). Results are normalized to the total cross-sectional area and compared to a perfectly conducting sphere of radius b (symbols).	113
3.51	Scattering from a coated metallic sphere having a 10 cm^{-1} fwhm absorption line (solid curve). Results are normalized to the core cross-sectional area and compared to a perfectly conducting sphere of radius a (symbols).	114
3.52	Real part n of the refractive index of a metal-oxide coating.	116
3.53	Imaginary part k of the refractive index of a metal-oxide coating.	117
3.54	Scattering from a metallic sphere coated with a metal-oxide coating.	118
3.55	Real part n of the refractive index of an absorbing dielectric material.	120
3.56	Imaginary part k of the refractive index of an absorbing dielectric material.	121
3.57	Scattering from a small, homogeneous sphere of absorbing dielectric material.	122
B.1	Typical set of data cards for the coated sphere scattering program.	135

LIST OF TABLES

<u>Table</u>	<u>Title</u>	<u>Page</u>
2.1	The attractive force F and components of the attractive force F_p , from the pressure differential, and F_τ , from the direct pull of the liquid, for several sphere radii, a . The critical wetting angle is θ_0 .	23
2.2	Equilibrium number of excess or deficient electron charges $\langle n \rangle$, sphere potential Φ , electric field E , and attractive force F for several sphere radii, a . F_{\max} is the force obtained for an electric field of 3×10^4 V/cm at the sphere surface.	26
2.3	Molecular attractive forces for spheres of various radii, a , coated with a nonpolar, dielectric coating.	34
C.1	Description of program variables.	137

I. INTRODUCTION

↓ This
Our research program is presently concerned with light scattering from dispersed metallic spheres that have been coated with a passive layer to reduce cohesion and to prevent excessive material degradation. ~~In Section II,~~ various mechanisms for the cohesion of spheres are investigated and the conditions under which particular mechanisms become dominant are determined. Using the Lenard-Jones potential as a mathematically convenient model potential for the molecular attraction of spheres, the thickness of a molecular-solid coating required to saturate the molecular binding from strong metallic binding to relatively weak van der Waals binding is estimated.

~~In Section III,~~ the theory of light scattering from coated spheres is investigated. The qualitative relationship between actual metallic spheres and perfectly conducting spheres is explored along with the qualitative similarity of coated metallic spheres and perfectly conducting spheres. Quantitative effects of nondispersive, absorbing, and nonabsorbing coatings of various thicknesses are determined. In the final part of this section, Lorentzian absorption lines of various linewidths are used as models for absorption and dispersion in actual coatings. A listing of the computer program for calculating the scattering from coated spheres and descriptions of the subroutines are given in the appendices. ↑

II. COHESION MECHANISMS

There are three mechanisms that can contribute to the cohesion of particles:¹⁻³

a) If two particles are linked by a liquid bridge that wets both particles, the surface tension of the liquid results in an attractive force. b) An electrically charged particle experiences attractive forces to oppositely charged particles, or to image charges induced in other uncharged particles and other uncharged surfaces. c) Two particles in close proximity experience molecular attraction and molecular binding. The strength and range of the molecular attraction depend on the particle material and the chemical-bonding mechanism appropriate to the material: i.e., van der Waals, metallic, covalent, or ionic.

A. Liquid Bridge

The simple theory of the liquid-bridge mechanism for particle cohesion presented in many textbooks⁴⁻⁶ seems to be incorrect, especially for very small size spheres. A more exact theory is presented in the following and the shortcoming of the simple theory is indicated. Both theories yield relatively large cohesive forces implying that the liquid-bridge mechanism would be the dominant mechanism for particle cohesion, if it actually occurs. However this mechanism seems not to apply to many experimental situations because the state of the adsorbed liquid is not a thermodynamic equilibrium state in many cases.

Consider the contact of two spheres, each having radius a , as is sketched in Fig. 2.1. An adsorbed liquid wets both particles out to an angle θ from the line connecting the sphere centers. The conditions for the liquid to wet the sphere material are discussed in Ref. 7. Generally, water will wet metal and metal-oxide surfaces but will not wet many polymer and other low binding energy (hence, low surface energy) materials.

The attractive force between spheres can be written⁸

$$F = \Delta P \pi \rho^2 + 2 \pi a \gamma \sin \theta \sin (\theta + \phi) , \quad (2.1)$$

where $\pi \rho^2$ is the cross-sectional area of the liquid, γ is the liquid surface tension, and ϕ is the contact angle that the liquid makes with the sphere surface. The first

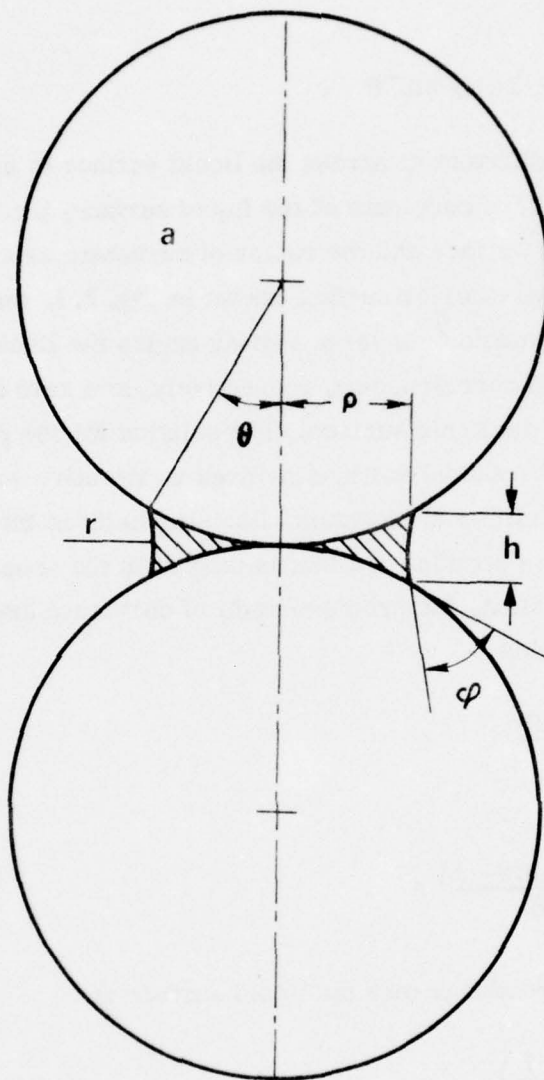


Fig. 2.1. Two spheres of radius a wet by liquid out to an angle θ from the line connecting the sphere centers. The liquid has a contact angle φ with the sphere surfaces and has a radius of curvature r .

term in Eq. (2.1) results from the fact that the pressure within the liquid is lower than the exterior by an amount ΔP . The second term comes from the direct pull of the liquid along the lines of contact on the spheres. With a contact angle of zero, Eq. (2.1) becomes

$$F = \Delta P \pi \rho^2 + 2 \pi a \gamma \sin^2 \theta \quad . \quad (2.2)$$

The pressure differential across the liquid surface is inversely proportional to the principal radii of curvature of the liquid surface, i.e., the radius of curvature at the exterior surface and the radius of curvature around the axis of symmetry. For the concave exterior surface shown in Fig. 2.1, the actual shape of the liquid surface is a nodoid.⁹ At large wetting angles the liquid surface becomes a catenoid or unduloid corresponding, respectively, to a zero or a positive pressure differential across the liquid surface. The solution for the principal radii of curvature of the actual nodoidal surface involves an iterative solution of equations involving incomplete elliptical integrals. For simplicity in the following, the surface is approximated by a circular arc that is tangent to the spheres at the wetting angle. With this approximation, the principal radii of curvature are obtained from simple geometry which yields

$$r = \frac{(1 - \cos \theta)}{\cos \theta} a \quad (2.3)$$

and

$$\rho = \left(\frac{\cos \theta + \sin \theta - 1}{\cos \theta} \right) a \quad . \quad (2.4)$$

The pressure differential across the liquid surface is

$$\Delta P = \gamma \left(\frac{1}{r} - \frac{1}{\rho} \right) \quad . \quad (2.5)$$

Derivations of the liquid-bridge force presented in several textbooks⁴⁻⁶ assume a circular-arc liquid surface, neglect the second term in Eqs. (2.1) and

(2.2) and neglect the second term in Eq. (2.5). These approximations are mathematically valid at small wetting angles and yield

$$F_0 = 2\pi a\gamma, \quad \text{as } \theta \rightarrow 0. \quad (2.6)$$

Although the attractive force in Eq. (2.6) remains finite as the wetting angle approaches zero, the pressure differential approaches negative infinity. This implies that the liquid is under considerable tension at small wetting angles. This does not seem physically possible, although it is not discussed in the textbooks presenting this derivation.

At finite wetting angles, both the attractive force and the pressure differential are angle dependent. To determine the dependence of the pressure differential on the wetting angle, a dimensionless pressure is derived by substituting the radii of curvature from Eqs. (2.3) and (2.4) into Eq. (2.5) and factoring a term γ/a :

$$(a/\gamma)\Delta P = \frac{\cos\theta}{1 - \cos\theta} - \frac{\cos\theta}{\cos\theta + \sin\theta - 1}. \quad (2.7)$$

This dependence of the pressure differential on angle is plotted in Fig. 2.2. At small angles the pressure differential goes to infinity as θ^{-2} . At $\theta = 53.1^\circ$ the pressure differential vanishes because the two principal radii of curvature are equal and opposite.

Similarly, the two force terms in Eq. (2.2) can be written in dimensionless form to bring out the angular dependence of these terms. The first component of the attractive force F_p , from the pressure differential, becomes

$$F_p/2\pi a\gamma = \frac{(\cos\theta + \sin\theta - 1)^2}{2\cos\theta} \left[\frac{1}{1 - \cos\theta} - \frac{1}{\cos\theta + \sin\theta - 1} \right]. \quad (2.8)$$

The other term F_τ , from the direct pull of the liquid, is

$$F_\tau/2\pi a\gamma = \sin^2\theta. \quad (2.9)$$

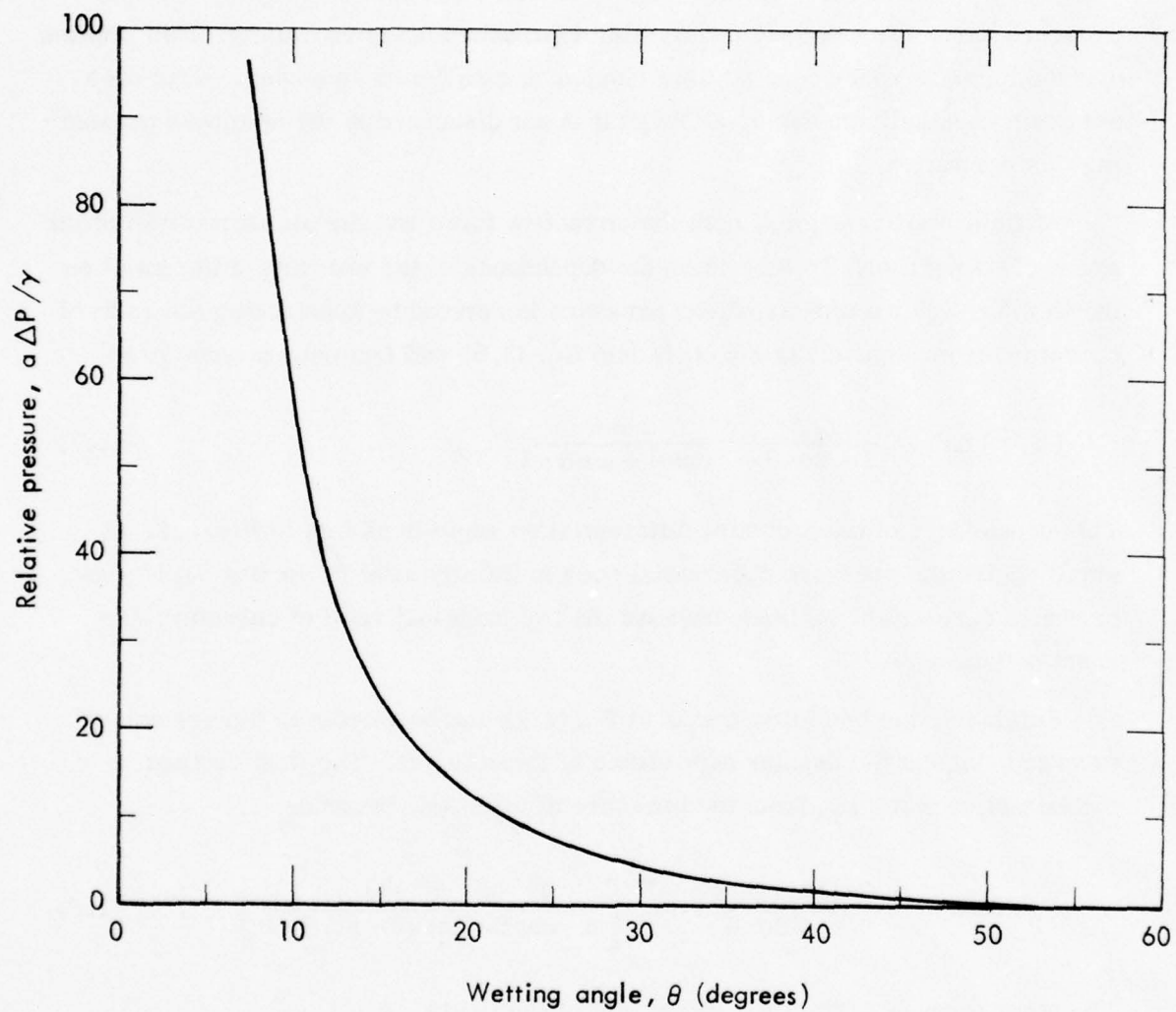


Fig. 2.2. Dependence of the liquid pressure differential on wetting angle.

These forces are plotted as functions of the wetting angle in Fig. 2.3. At small angles, the pressure term dominates and approaches the limiting value given by Eq. (2.6). As the wetting angle increases, contributions from F_τ become non-negligible. The two terms are equal at 33.5° and the pressure term vanishes at 53.1° .

To solve for the attractive force as a function of sphere size, the following approach is taken: First, a "critical wetting angle" θ_0 is determined at which the pressure differential equals atmospheric pressure ($1.01 \times 10^6 \text{ dyne/cm}^2$) using the surface tension of water $\gamma = 70 \text{ dyne/cm}^2$. Next θ_0 is substituted into Eqs. (2.3) and (2.4) which along with Eqs. (2.5) and (2.2) yield the attractive force. The critical wetting angle θ_0 is plotted as a function of the sphere radii in Fig. 2.4. The two components of the attractive force and the total attractive force $F = F_p + F_\tau$ are plotted in Fig. 2.5. Tabular results are presented in Table 2.1.

The above derivation makes the reasonable and convenient approximations of a zero contact angle and a circular arc surface. In addition, the sagging of the liquid due to gravity and the buoyant force of the liquid are neglected, as is valid at small sphere sizes.

It is seen from Table 2.1 and Fig. 2.4 that the critical wetting angles for small spheres are quite large, approaching the limiting value of 53.1° . In this size range, the attractive force presented in Fig. 2.5 is dominated by the direct surface tension term F_τ . The two components of the attractive force are equal near the sphere radius of $2 \mu\text{m}$ ($\theta_0 = 33.5^\circ$) and the pressure differential term F_p dominates at sphere radii larger than this value. It is interesting to note that the total force $F = F_p + F_\tau$ is approximately equal to the naive textbook value given in Eq. (2.6). This agreement is regarded as accidental.

Should the particles be wet to angles greater than θ_0 , the cohesive forces decrease as is apparent from Fig. 2.2. Larger forces than those presented in Table 2.1 and Fig. 2.5 would be obtained at smaller angles if large negative pressures (tensile forces) are allowed in the liquid. There is no discussion of such tensile forces in the literature on sphere cohesion except for a brief statement in Ref. 9a where it is stated that this may be a limiting effect. A similar

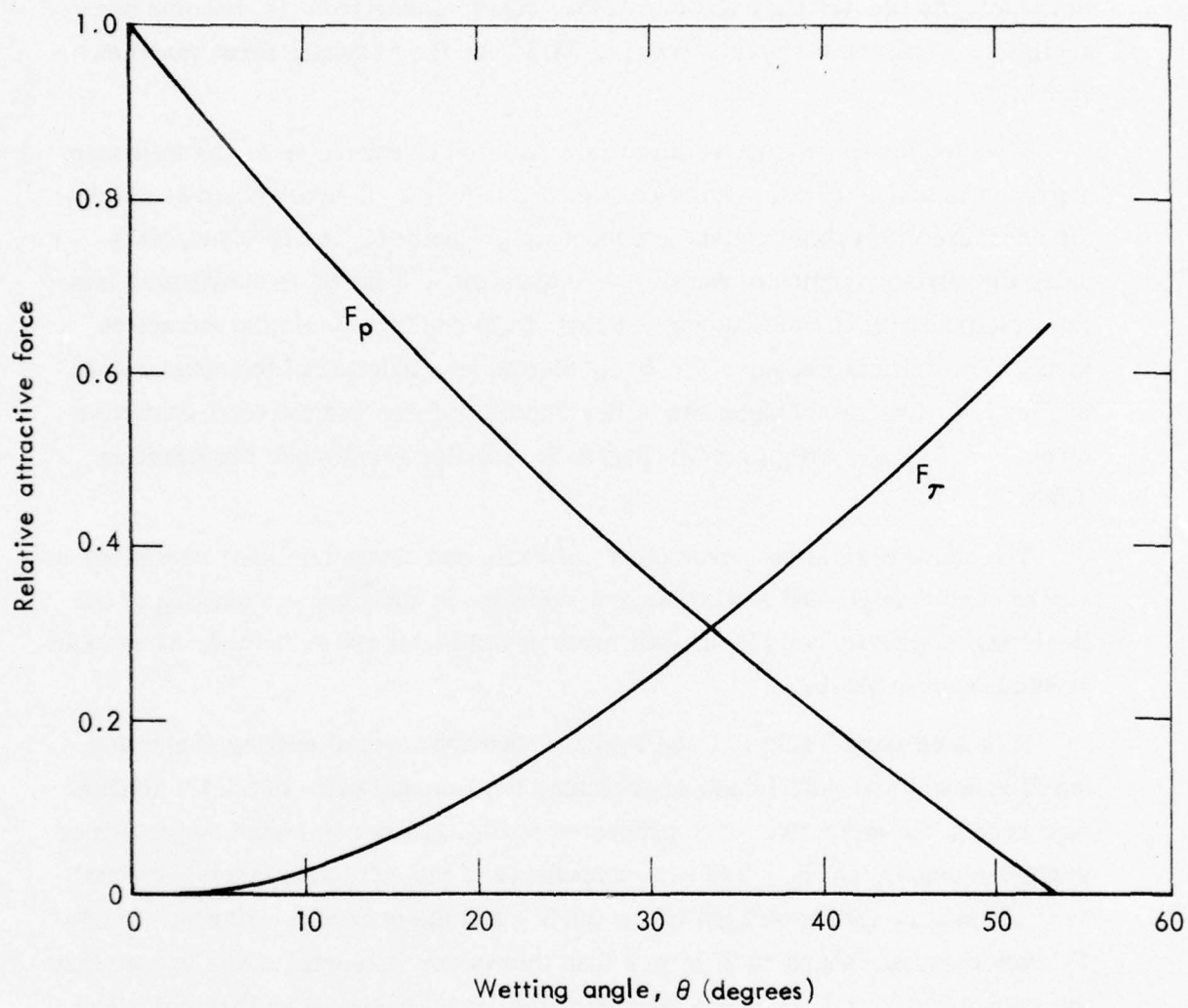


Fig. 2.3. Dependence of the attractive force component on wetting angle.

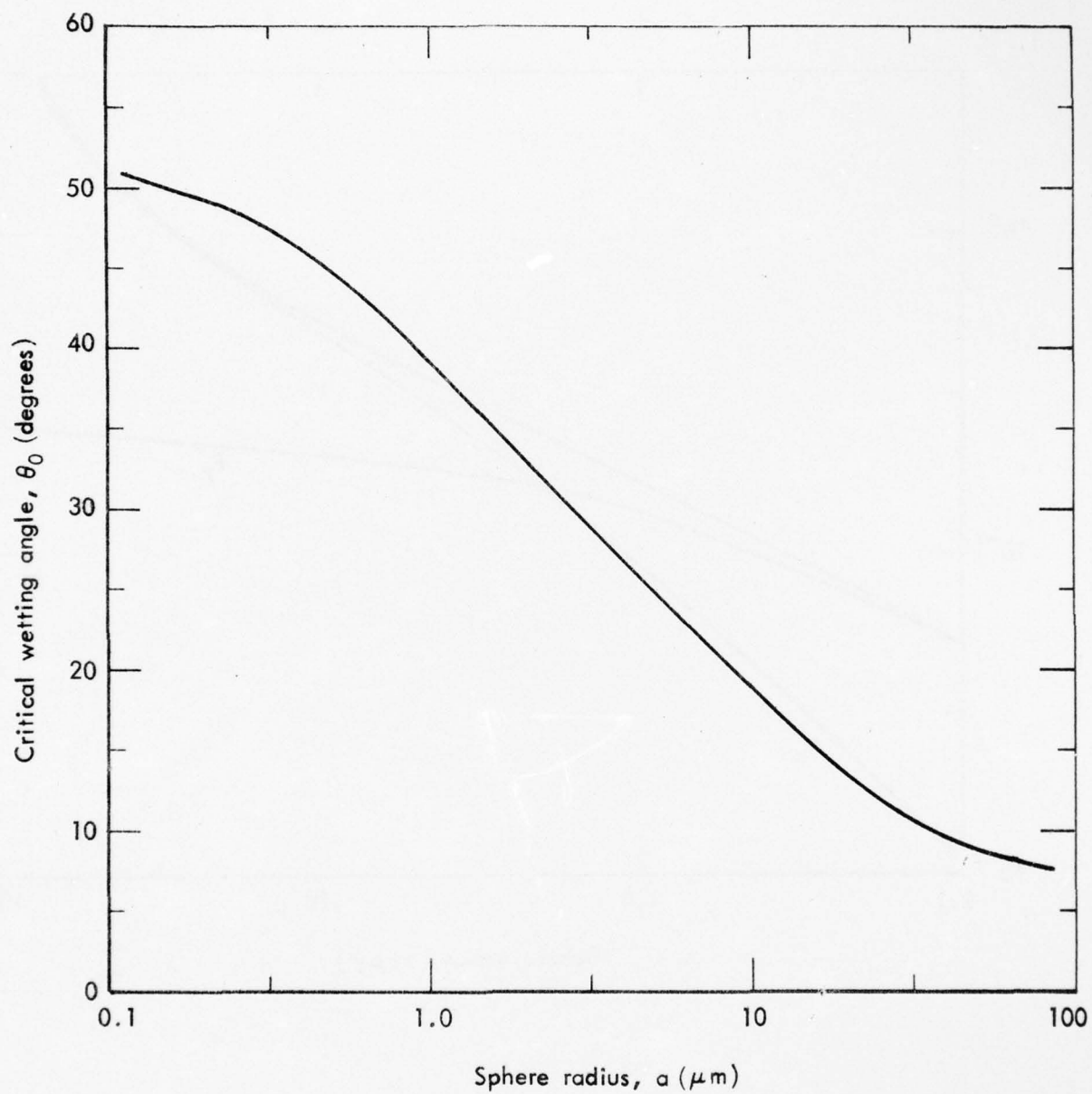


Fig. 2.4. Dependence of the critical wetting angle on sphere radius.

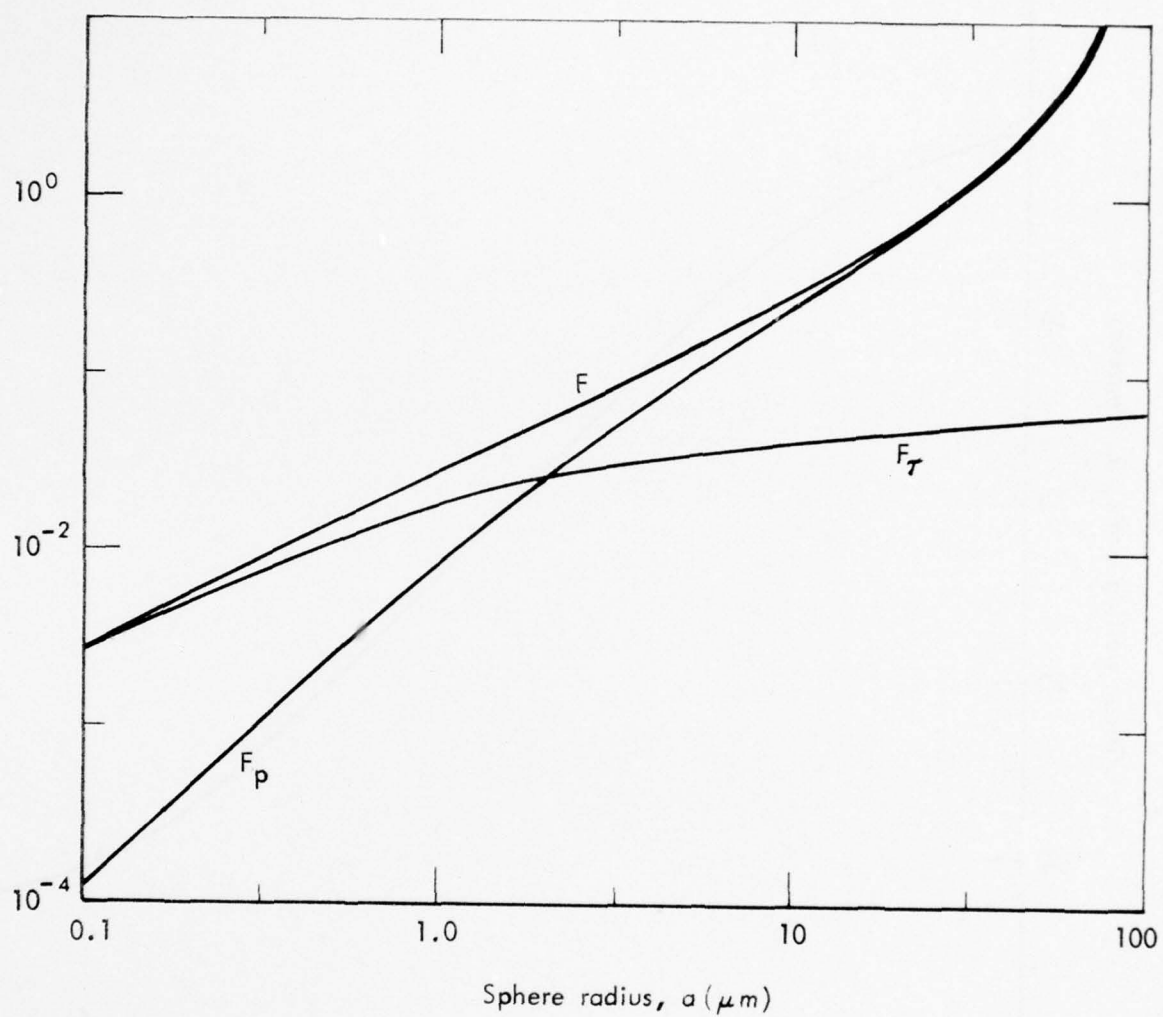


Fig. 2.5. Dependence of the liquid-bridge attractive forces on sphere radius.

Table 2.1. The attractive force F and components of the attractive force F_p , from the pressure differential, and F_τ , from the direct pull of the liquid, for several sphere radii a . The critical wetting angle is θ_0 .

a (μm)	θ_0 (degrees)	F_p (dyne)	F_τ (dyne)	F (dyne)
0.05	52.1	3.40×10^{-5}	1.37×10^{-3}	1.40×10^{-3}
0.25	48.4	7.67×10^{-4}	6.15×10^{-3}	6.92×10^{-3}
0.50	44.9	2.70×10^{-3}	1.10×10^{-2}	1.37×10^{-2}
2.5	31.2	3.80×10^{-2}	2.95×10^{-2}	6.75×10^{-2}
5.0	24.6	1.02×10^{-1}	3.81×10^{-2}	1.40×10^{-1}
25.0	12.5	7.74×10^{-1}	5.15×10^{-2}	8.26×10^{-1}
50.0	9.07	1.71	5.46×10^{-2}	1.76

effect occurs with very small capillary tubes where negative pressures have been observed.¹⁰⁻¹² However in the capillary tubes, the tensile state of the liquid is a metastable state and is lost when a bubble is nucleated. Nevertheless such metastable states occur regularly in nature as is evidenced by sap in the xylem tubes of trees that are over 10 m (34 ft.) in height.¹³ Hence if wetting angles less than the critical angle θ_0 occur, the liquid will be under tension and in a metastable state.

It may be very difficult to form a liquid bridge between particles even at angles greater than θ_0 unless one starts with the particles completely immersed in the liquid. If the particles are initially dry, liquid may not condense at the points of contact. The difficulty in condensation here is analogous to the well-known difficulty in the homogeneous nucleation of small water drops or small bubbles. It may be possible to form liquid bridges between the particles if the particles are initially immersed and liquid is withdrawn from the sample. In this case sudden evaporation of the liquid may occur when the critical angle is reached.

B. Electrostatic

The electrostatic attraction of charged spheres is complicated by the facts that the mechanisms for charging particles are not well understood and the locations of the charges on, or within, the particles generally are not known.^{14, 15} Only with conducting spheres that are free of contamination can predictions be made with any degree of confidence. As a known example, consider the contact of spheres of two different metals having differing electron work functions. Electrons are transferred from one sphere to the other until the Fermi levels are aligned (i.e., as in a thermocouple).¹⁴ Excess electrons on a conducting sphere spatially isolated from other material surfaces, are uniformly distributed over the surface. However, the presence of other particles, charged or not, will perturb this uniform distribution.

With dielectric particles or contaminated metallic particles, charging often involves the transfer of ions absorbed on the surfaces as well as the transfer of electrons. The ion-transfer mechanism is very dependent on complexities of the surface such as past surface treatments and the relative humidity of the surrounding atmosphere. To predict the charge transfer between bulk samples of various

materials, researchers have attempted to set up triboelectric series of materials analogous to electrochemical potential series. However, such series are not reproducible, with series set up by different researchers being very dissimilar and lacking agreement on the positions of materials in the series.¹⁴

Ignoring the mechanism for charging, the equilibrium amount of charge on an isolated sphere can be derived from thermodynamic considerations.¹ A spatially isolated sphere, of radius a with an excess or deficiency of n electrons uniformly distributed over its surface, has an electrostatic potential energy

$$\mathcal{E} = (ne)^2/2a, \quad (2.10)$$

where e is the charge of an electron. Assuming a Boltzmann distribution, the probability that a sphere has n excess or deficient electrons is

$$f = \exp \left[-(ne)^2/2akT \right] / \sum_{n=-\infty}^{\infty} \exp \left[-(ne)^2/2akT \right], \quad (2.11)$$

where k is the Boltzmann constant and T is the temperature. The mean magnitude of n is

$$\langle n \rangle = (2akT/\pi e^2)^{1/2}. \quad (2.12)$$

Values of $\langle n \rangle$ are listed in the second column of Table 2.2 for several sphere radii.

Rather than attempting to specify the details of the distribution of the charge on or within the particle, the following model problem is considered: With a spatially isolated and uniformly charged sphere, the electric field outside of the sphere appears as though the charge is concentrated at the center of the sphere. Hence as a first approximation for a charged sphere in contact with an uncharged sphere, the excess charge is considered to be positioned at the center of the charged sphere. If the spheres both have radii equal to a , the charge ne in the first sphere induces an image charge of magnitude $-ne/2$ at a distance $a/2$ from the center of the second sphere. This situation is sketched in Fig. 2.6. (The magnitude and position of the image charge is appropriate for a conducting sphere, with dielectric spheres having a smaller magnitude image charge at a different position.) The attractive force between the charges is

Table 2.2. Equilibrium number of excess or deficient electron charges $\langle n \rangle$, sphere potential Φ , electric field E , and attractive force F for several sphere radii, a . F_{\max} is the force obtained for an electric field of 3×10^4 V/cm at the sphere surface.

a (μm)	$\langle n \rangle$	Φ (mV)	E (V/cm)	F_{eq} (10^{-12} dyne)	F_{\max} (dyne)
0.05	0.68	19.6	3910	947	5.57×10^{-8}
0.25	1.66	9.55	382	226	1.39×10^{-6}
0.50	2.37	6.82	136	115	5.57×10^{-6}
2.5	5.34	3.07	12.3	23.4	1.39×10^{-4}
5.0	7.54	2.17	4.34	11.6	5.57×10^{-4}
25.0	16.9	0.91	0.39	2.34	1.39×10^{-2}
50.0	23.9	0.69	0.14	1.17	5.57×10^{-2}

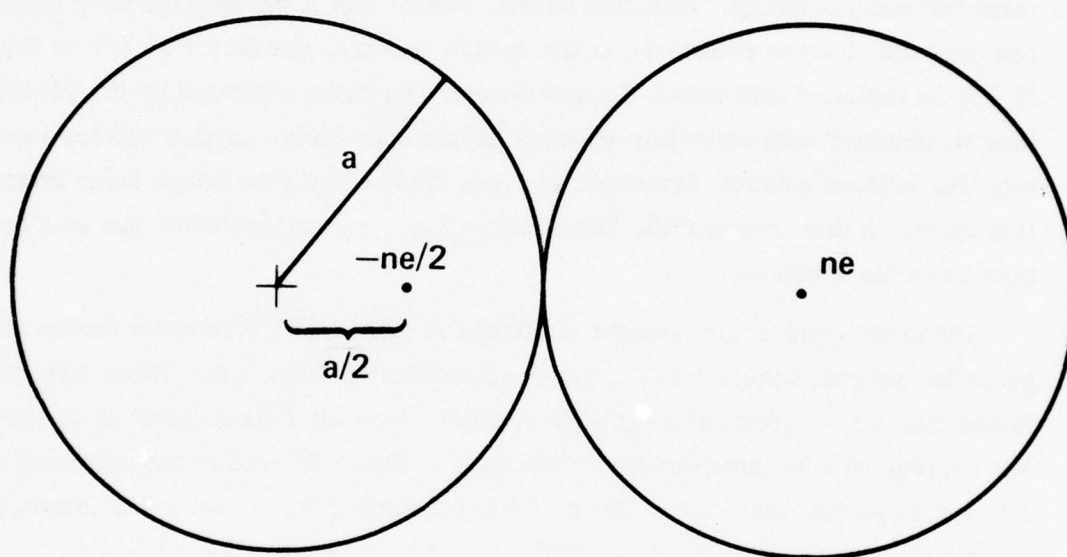


Fig. 2.6. A charge of magnitude ne at a distance of $2a$ from a conducting sphere of radius a , induces an image charge of magnitude $-ne/2$ in the conducting sphere.

$$F = \frac{2}{9} \frac{(ne)^2}{a^2} \quad . \quad (2.13)$$

This model is perhaps most valid for conducting spheres coated with a thin dielectric layer. For conducting spheres where an insulating layer prevents equilibration of the excess charge, the result in Eq. (2.13) is the first term in a series generated by alternately placing image charges in the two spheres to satisfy boundary conditions.¹⁶

The force given by Eq. (2.8) should be valid as an order-of-magnitude estimate for many seemingly different cases. Notice that if the spheres have equal and opposite charges positioned at the sphere centers, the factor of $2/9$ in Eq. (2.13) is replaced with unity. Larger forces than those indicated by Eq. (2.13) may be obtained with dielectric spheres having oppositely charged surface ions near the point of contact. However, the ions themselves experience large attractive forces in this case and the large forces may be ameliorated by the ions being torn from the surfaces.

Using the equilibrium amount of charge in Eq. (2.13), attractive forces are given for several sphere radii in the third column of Table 2.2. These attractive forces are many orders of magnitude smaller than either those given in the previous section for the liquid-bridge mechanism or those derived in the following section for molecular attraction. Hence for electrostatic forces to be important, the magnitude of the charge must be much greater than the equilibrium value.

Under favorable circumstances such as in a corona discharge, spheres can be charged far in excess of their equilibrium values where as many as one thousand excess electrons are observed on micron-sized particles.^{1, 14} To search for a mechanism to limit the ultimate possible excess charge, the electrical potential of the particle and the magnitude of the electrical field at the particle surface were examined. Values of these quantities are listed in the fourth and fifth columns of Table 2.2 for spheres having equilibrium numbers of electrons. The equilibrium value of the electrical potential is in the millivolt range for all particle sizes and, hence, is not expected to prevent increases in the charge under favorable circumstances. On the other hand, the electric field at the sphere surface is quite large for small spheres. Attempts to increase the charge on small spheres beyond the equilibrium value will be limited by air breakdown near the sphere surface.

To estimate the maximum possible electrostatic forces, it is assumed that the sphere charge is limited by a value of 3×10^4 V/cm for the electric field at the sphere surface. Solving for the charge required to produce this field and substituting the result into Eq. (2.13) yields the values in the sixth column of Table 2.2 labeled F_{\max} . These values are still approximately one order of magnitude smaller than the liquid-bridge forces obtained in the previous section. However, at the largest particle sizes, the maximum electrostatic forces become comparable to molecular forces.

Such highly charged particles are expected to be the exception rather than the general rule. In a large sample containing many particles, binding from the electrostatic mechanism should occur only for relatively few particles.

C. Molecular Attraction

The molecular attraction between spheres is viewed two ways:^{2,6} First, a model potential such as the Lenard-Jones potential is integrated over the volume of the spheres.¹⁷ Differentiation yields the cohesive force. Secondly, an effective area of contact is derived from geometrical considerations. This effective area, when multiplied by the material tensile strength, yields the force of attraction. The Lenard-Jones potential used in the first method is strictly applicable only to nonpolar molecular solids having van der Waals bonding. However, it can be used as a mathematically convenient model potential for order-of-magnitude estimates of the cohesive force between other types of materials. Additionally, the Lenard-Jones potential is used to estimate the coating thickness required to saturate the attraction so that the cohesion is determined by the coating rather than the core.

Consider two spheres, one of radius a and the other of radius b , having a distance L between sphere centers. The Lenard-Jones potential between volume elements dV_1 in the first sphere and dV_2 in the second sphere is

$$d^6 U = - \frac{\beta}{\rho^6} dV_1 dV_2 \quad , \quad (2.14)$$

where ρ is the distance between the volume elements and β is a material-dependent constant. Integration over the volume of the first sphere yields

$$d^3U = -4\pi a^3 \beta dV_2/3 (r^2 - a^2)^3, \quad -4\pi a^3 \beta dV_2/3 (r^2 - a^2)^3 \quad (2.15)$$

where r is the distance of the volume element dV_2 from the center of the first sphere. Integration over the volume of the second sphere yields the potential between the two spheres:

$$U = -\pi^2 \beta \frac{a^3}{3} \left\{ \frac{(L-b)}{a^2 [(L-b)^2 - a^2]} - \frac{(L+b)}{a^2 [(L+b)^2 - a^2]} + \frac{1}{2a^3} \ln \left(\frac{L-b-a}{L-b+a} \right) - \frac{1}{2a^3} \ln \left(\frac{L+b-a}{L+b+a} \right) - \frac{1}{L[(L-b)^2 - a^2]} + \frac{1}{L[(L+b)^2 - a^2]} \right\} \quad (2.16)$$

Differentiating with respect to L and collecting terms yields the attractive force between spheres:

$$F = \frac{32}{3} \pi^2 \beta \frac{a^3 b^3 L}{[(L^2 + b^2 - a^2)^2 - 4b^2 L^2]^2} \quad (2.17)$$

The force given in Eq. (2.17) diverges at $L = a + b$ because we have neglected to include a repulsive term in the potential. Rather than including a repulsive term, the divergence is avoided by defining sphere contact as occurring when $L = a + b + \delta$, where δ is a lattice spacing.

The result given in Eq. (2.17) is next used to calculate the force between two coated spheres each having core radius a and total radius $b = a + t$, where t is the coating thickness. For coated spheres the attractive force is the sum of the forces between cores, between cores and coatings, and between coatings. The force between cores is

$$F_{a,a} = \frac{32}{3} \pi^2 \beta_{11} \frac{a^6}{L^3 [L^2 - 4a^2]^2} \quad (2.18)$$

where β_{11} is the potential parameter for the core material. The force between each core and the coating on the other sphere has potential parameter β_{12} . This force is equal to the force between the core and a homogeneous, solid sphere of the coating material with radius b minus the force between the core and a sphere of coating material having radius a :

$$F_{a,b} = \frac{64}{3} \pi^2 \beta_{12} \frac{a^3 b^3 L}{[(L^2 + b^2 - a^2)^2 - 4b^2 L^2]^2} - \frac{64}{3} \pi^2 \beta_{12} \frac{a^6}{L^3 [L^2 - 4a^2]^2} \quad (2.19)$$

The force between coatings equals the force between homogeneous, solid spheres of the coating material of radius b minus the force between cores of coating material and minus the force between cores and coatings:

$$F_{b,b} = \frac{32}{3} \pi^2 \beta_{22} \frac{b^6}{L^3 [L^2 - 4b^2]^2} - \frac{64}{3} \pi^2 \beta_{22} \frac{a^3 b^3 L}{[(L^2 + b^2 - a^2)^2 - 4b^2 L^2]^2} + \frac{32}{3} \pi^2 \beta_{22} \frac{a^6}{L^3 [L^2 - 4a^2]^2} \quad (2.20)$$

Summing Eqs. (2.18), (2.19), and (2.20) yields the force between coated spheres:

$$F = \frac{32}{3} \pi^2 (\beta_{11} - 2\beta_{12} + \beta_{22}) \frac{a^6}{L^3 [L^2 - 4a^2]^2} + \frac{32}{3} \pi^2 \beta_{22} \frac{b^6}{L^3 [L^2 - 4b^2]^2} + \frac{64}{3} \pi^2 (\beta_{12} - \beta_{22}) \frac{a^3 b^3 L}{[(L^2 + b^2 - a^2)^2 - 4b^2 L^2]^2} \quad (2.21)$$

To examine the reduction in the attractive force from the coating, consider a coating having potential parameter $\beta_{22} = 0.1\beta_{11}$. The relative potential parameter is $\beta_{12} = (\beta_{11}\beta_{22})^{1/2} = 0.316\beta_{11}$. To obtain the effect of the coating thickness t , we take $b = a + t$ and $L = 2a + 2t + \delta$ with $\delta = 4 \times 10^{-8}$ cm. The attractive force between two coated spheres using these values in Eq. (2.21) is plotted as a function of coating thickness in Fig. 2.7. The attractive force has a minimum value for coating thicknesses near 40 Å. For thicknesses greater than this value, the attractive force increases due to the increased sizes of the spheres. The continuum model used in this calculation is not valid for coating thicknesses less than about 10 Å. Nevertheless, the rapid decrease of the attractive force for small coating thicknesses obtained from the continuum model indicates that only a few molecular layers of coating are necessary to saturate the forces so that the force is determined nearly entirely by the coating rather than the core.

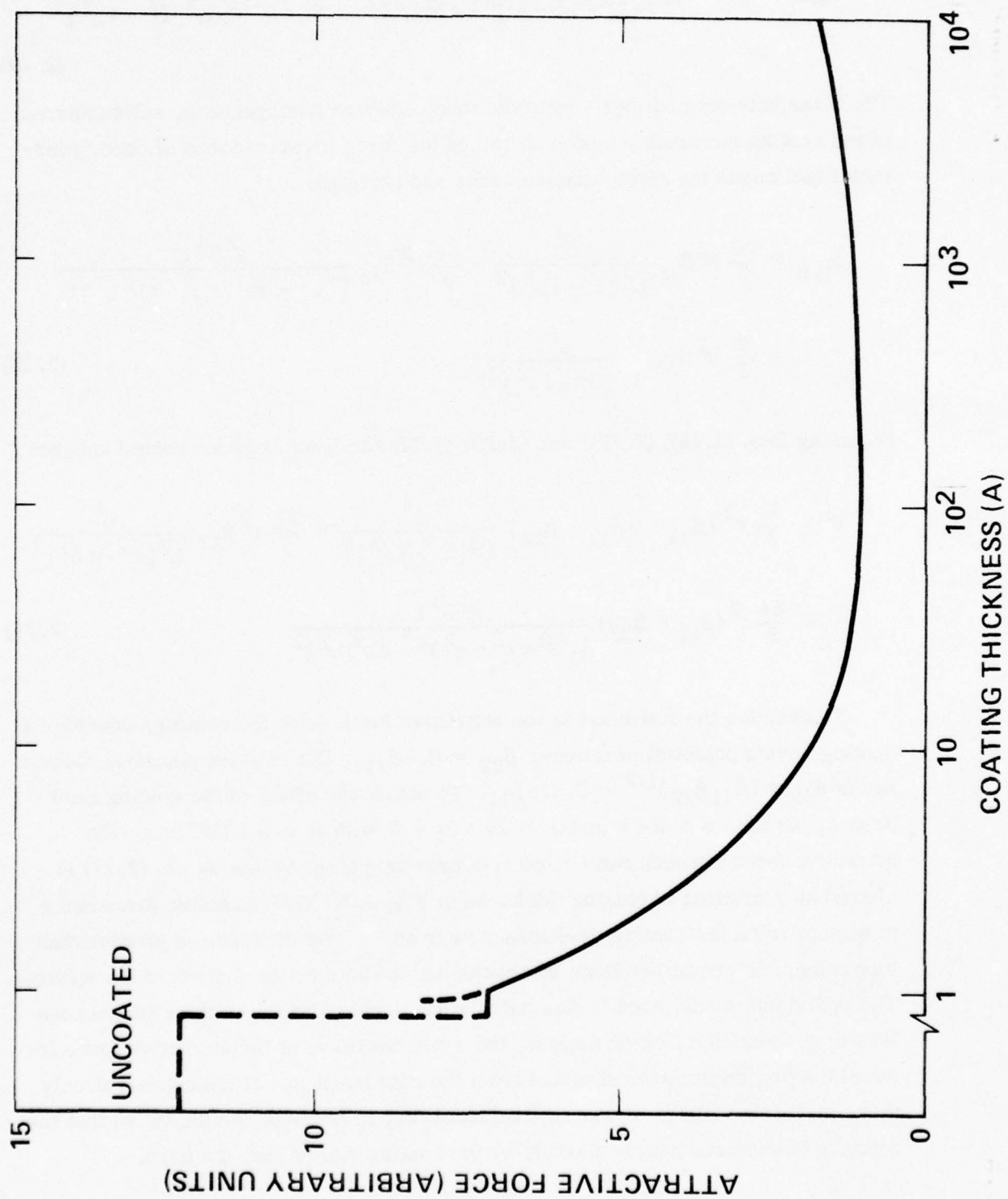


Fig. 2.7. Dependence of the molecular attractive force on coating thickness.

To obtain numerical values for metallic spheres coated with nonpolar dielectrics, we take $\beta_{22} = C_L / \Omega^2$, where Ω is the atomic volume of the atoms in the coating and C_L is the constant in the London force equation for the force between two spherically symmetric atoms.^{2, 17} This constant is evaluated from

$$C_L = 3\alpha^2 h\nu / 4 \quad , \quad (2.22)$$

where α is the atomic polarizability and $h\nu$ is the electronic excitation energy of the atoms. As typical values we take $\Omega = (4 \times 10^{-8} \text{ cm})^3$, $\alpha = 10^{-24} \text{ cm}^3$, and $h\nu = 1.60 \times 10^{-11} \text{ erg}$ (10 eV). These values yield

$$\beta_{22} \cong 2.9 \times 10^{-15} \text{ erg} \quad . \quad (2.23)$$

Assuming that the coating is sufficiently thick to saturate the attractive force, this value, along with $L = 2b + \delta$, where $\delta = 4 \times 10^{-8} \text{ cm}$ for spheres in contact, yields the attractive force

$$F = (1.49 \text{ dyne/cm}) a \quad . \quad (2.24)$$

Values of the force for several sphere radii are presented in Table 2.3.

A second way of viewing the molecular attraction between two spheres in contact is from a materials strength point of view.^{2, 4} In this method the spheres are again viewed as being homogeneous and continuous, rather than atomic. The hypothesis is made that the distinction of one sphere surface from the other is lost if the surfaces are within a distance of approximately one lattice spacing, i.e., about $4 \times 10^{-8} \text{ cm}$. Referring to Fig. 2.8, it is seen that the distance h between sphere surfaces is approximately $h \cong \rho^2 / a$, where ρ is the distance from the line connecting the sphere centers and a is the sphere radius. The effective area of contact between spheres is

$$A = \pi \rho^2 = \pi a h \quad . \quad (2.25)$$

Multiplying this area by the tensile strength σ^c of the material yields the cohesive force

$$F = \sigma^c \pi a h \quad . \quad (2.26)$$

Table 2.3. Molecular attractive forces for spheres of various radii, a , coated with a nonpolar, dielectric coating.

$a (\mu\text{m})$	0.05	0.25	0.50	2.5	5.0	25.0	50.0
$F (\text{dyne})$	7.4×10^{-6}	3.7×10^{-5}	7.4×10^{-5}	3.7×10^{-4}	7.4×10^{-4}	3.7×10^{-3}	7.4×10^{-3}

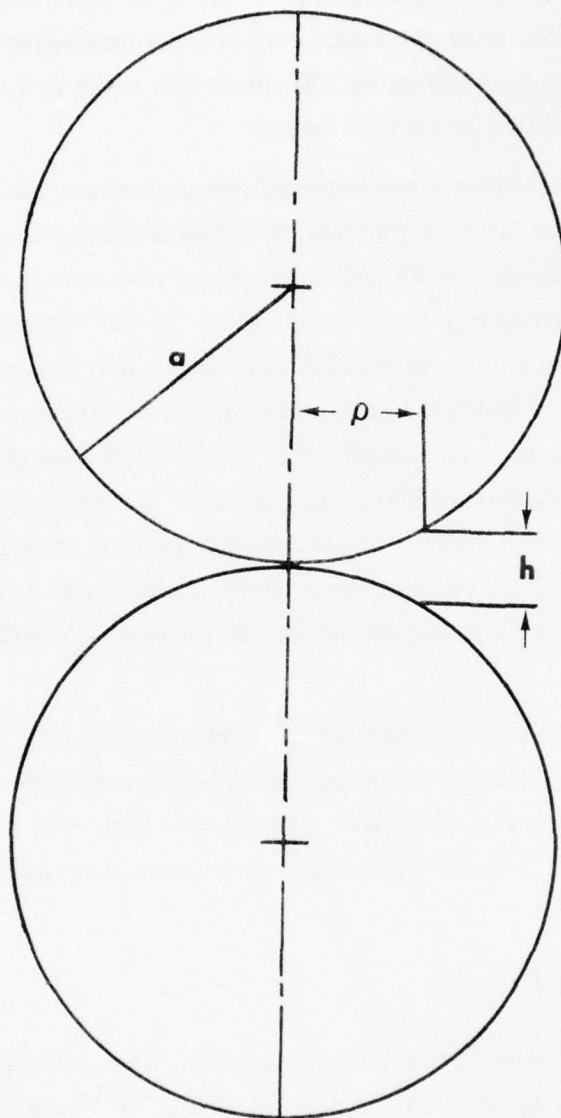


Fig. 2.8. Separation h of the sphere surfaces at a distance ρ from the line between sphere centers.

For nonpolar molecular solids the two methods yield equivalent results. The attractive force, derived from the Lenard-Jones potential presented in Eq. (2.24), implies a tensile strength $\sigma^c = 1.2 \times 10^7$ dyne/cm² (170 psi). This value is approximately what one would expect for a molecular solid. The tensile strength of metals is approximately 100 times this value and implies an approximately 100 times greater attractive force.

Intuitively the cohesive force between oxidized-metal spheres is expected to be less than the force for pure metals. With metal oxides or with other ionic and covalent solids, estimates of the attractive force are complicated by uncertainties in the tensile strength of these materials. Tensile strengths of bulk ionic and covalent solids are sensitive to small cracks which are comparable in size to the smallest sphere sizes under consideration. If cracks are not important with small spheres and theoretical tensile strengths are used, the cohesive force is as large, or greater than, the cohesive force for pure metals. Instead, it is expected that dielectric coatings are sensitive to the crystallographic orientation of the coatings on the two spheres. This misalignment of the lattices may result in a decreased cohesive force analogous to decreased tensile strengths in bulk, dielectric solids from small cracks.

Additionally, malleability may favor the cohesion of pure metals due to increases in the effective area of contact caused by deformation around the point of contact under the action of molecular attraction.¹ When two elastic spheres are pressed together with a force F , there is a flat area surrounding the point of contact having radius¹⁸

$$\rho = 0.88 [Fa/E]^{1/3}, \quad (2.27)$$

where E is the elasticity of the sphere material. Using the attractive force given by Eq. (2.26) and using $E = 10^{11}$ dyne/cm² and $\sigma^c = 10^7$ dyne/cm² as typical values for a metal, the area of contact is

$$A = (2.84 \times 10^{-6}) a^{4/3}, \quad (2.28)$$

where the units of A are cm² for a expressed in cm. With $a = 2.5 \times 10^{-4}$ cm, Eq. (2.28) yields 4.5×10^{-11} cm² which is comparable to the effective area of 3.1×10^{-11} cm² given by Eq. (2.15). These values indicate that the effective area of

contact for a pure metal, or for a thin oxide-coated metal, may be enhanced compared to dielectrics and thick oxide coatings. The continuum model is not thought to be sufficiently accurate to estimate the amount of enhancement.

D. Summary and Conclusions of Cohesion Study

Cohesive forces from the various mechanisms discussed in the preceding sections are presented graphically in Fig. 2.9. The attraction from the liquid-bridge mechanism, if it occurs, has the largest magnitude. However, liquid bridges may not be formed between particles under the experimental conditions of interest, as is discussed in Section IIA. Molecular attractive forces are greatest for metallic spheres and smallest for spheres coated with a nonpolar dielectric having van der Waals molecular binding. Coatings having covalent or ionic binding are expected to have intermediate force values with the range of possible molecular attraction forces extending between (and perhaps somewhat beyond) the two curves labeled molecular, metal and molecular, Lenard-Jones.

To avoid the large cohesive forces between metallic spheres, the spheres should be coated with a nonpolar dielectric coating having van der Waals binding. The calculation in the previous section indicates that the coating need only be a few molecular layers thick to saturate the forces so that the attraction is determined by the coating rather than the core. The liquid-binding mechanism can be avoided if the coating is hygrophobic.

The concern that electrostatic forces may become troublesome with dielectric coatings does not appear to be a problem. If the particles have the thermodynamic equilibrium amount of charge, the electrostatic forces are negligible, as is indicated by the bottom curve of Fig. 2.9. The amount of charge required to make the electrostatic force comparable to the molecular force is unreasonably large, with large electric fields occurring near the particle surface. It is thought that such large charges will only occur in exceptional circumstances and, in general, will be present only on a few spheres of a large sample.

One of the easiest coatings to apply to the particles is an oxide coating. Even though the tensile strength of oxides can be as large as metals, the sphere binding force may be smaller for oxidized spheres because of the sensitivity of oxides to crystallographic orientation. If the spheres are oxidized while in contact,

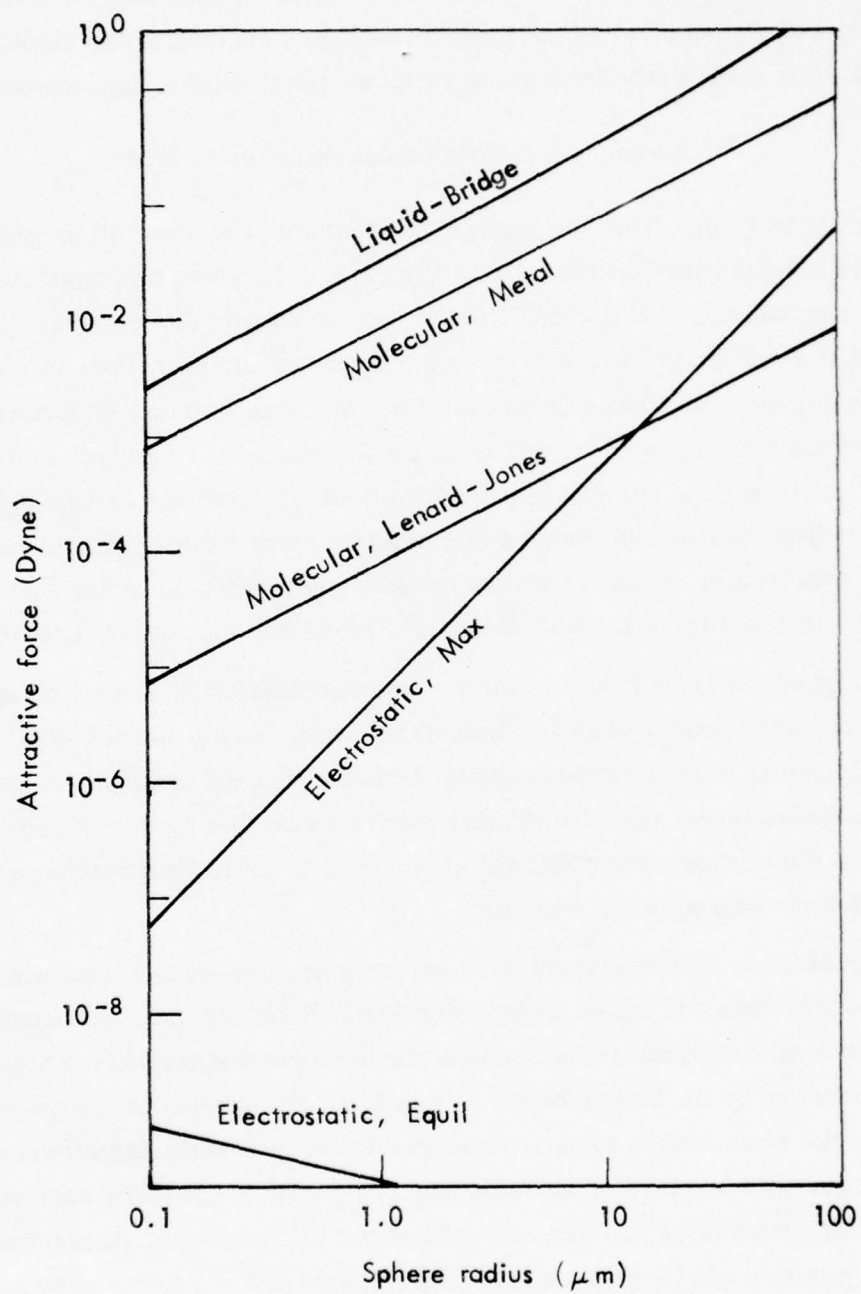


Fig. 2.9. Comparison of cohesion mechanisms.

an oxide bridge of large cross section may be grown between the spheres with a subsequently large binding force. It will then be necessary to mechanically break the spheres apart. Once separated, smaller attractive forces are expected to be obtained.

Another simple method of reducing cohesion is to use spacer particles smaller in size than the primary particles to avoid contact of the primary particles. The spacer particles can be made of a material such as carbon that has weak binding to the metal. Additionally because of the smaller size of the spacer particles, the attractive force between a spacer and primary particles is smaller than between two particles of the same size so that the cohesion of the mixture is reduced. Spacer particles are expected to have little effect on the light scattering from the dispersed mixture for two reasons: First, spacer particles are only a small fraction of the total mass. Second, the size of the spacer particles falls in a range where the scattering is inefficient, i.e., the scattering cross section is smaller than the geometrical cross section. Should a spacer particle remain bound on the surface of a primary metallic particle, it should have little effect on the scattering of the primary particle. The maximum effect on the scattering will occur if the spacer is positioned at a local maximum in the electric field on the surface of the primary particle. It could then result in damping of one of the multipole moments contributing to the scattering, but the effect should be small since several multipole moments contribute.

Coatings that have desirable properties from a molecular point of view are many polymers and such fatty acids as stearic acid. Of the polymers, teflon is desirable because it is hydrophobic and because it, along with other fluorinated hydrocarbons, has a small polarizability which yields small attractive forces. Methods for depositing teflon from the gas phase by ultraviolet photolysis have been published.¹⁹⁻²¹ A possible problem with polymer coatings that could lead to increasing binding is incomplete chain termination with loose bonds on two particles combining and forming a bridge between particles.

Low cohesive forces should be obtained with metallic spheres coated with an aligned monomolecular layer of fatty acid.^{3,7,22} Stearic, lauric, and other fatty acids are used as additives in lubricating oils to provide boundary lubrication under high-pressure conditions, vacuum conditions, or other situations where the

lubricating oil may be lost. The fatty acids consist of a backbone of carbon atoms with a reactive carboxyl radical on one end. When applied from a dilute solution to active metals such as copper or zinc, the carboxyl radical reacts with the substrate metal forming an aligned monomolecular layer as is sketched in Fig. 2.10. Such a layer will not be formed on noble metals such as gold and silver. It has been noted that care is needed to get a reaction on aluminum, with factors such as the degree of surface strain and amount of oxide present on the surface influencing the reaction. If two surfaces coated with monolayers of fatty acid are brought into contact, contact is made between the inert, nonpolar tails facing outward from the coated metals. The Lenard-Jones potential is applicable for the interaction between the tails and very small forces of attraction should be obtained. Such coatings can possibly be applied to small metallic spheres by reaction from a volatile solvent such as benzene, although with semi-inert metals such as aluminum more care may be needed to insure a reaction with the substrate.

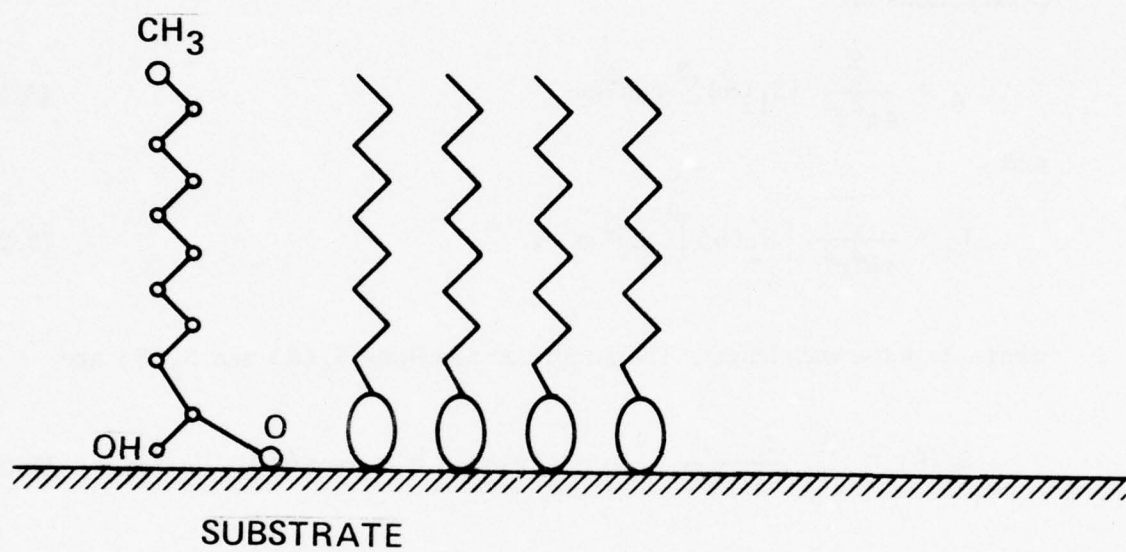


Fig. 2.10. Aligned monolayer of fatty acid.

III. LIGHT SCATTERING FROM COATED SPHERES

A. Theory

Scattering from a spherically symmetric object is described with the aid of Fig. 3.1.²³⁻²⁵ Incident radiation of unit intensity and polarized in the \hat{x} direction propagates in the \hat{z} direction to the particle located at the origin. The scattered intensities at the position (r, θ, φ) for the two polarizations in the $\hat{\theta}$ and $\hat{\phi}$ directions are

$$I_{\theta} = \frac{\lambda^2}{4\pi^2 r^2} |S_1(\theta)|^2 \cos^2 \varphi \quad (3.1)$$

and

$$I_{\phi} = \frac{\lambda^2}{4\pi^2 r^2} |S_2(\theta)|^2 \sin^2 \varphi, \quad (3.2)$$

where λ is the wavelength. The amplitude functions $S_1(\theta)$ and $S_2(\theta)$ are

$$S_1(\theta) = \sum_{n=1}^{\infty} \frac{2n+1}{n(n+1)} \left[a_n \pi_n(\cos\theta) + b_n \tau_n(\cos\theta) \right] \quad (3.3)$$

$$S_2(\theta) = \sum_{n=1}^{\infty} \frac{2n+1}{n(n+1)} \left[a_n \tau_n(\cos\theta) + b_n \pi_n(\cos\theta) \right], \quad (3.4)$$

where π_n and τ_n are Legendre functions and where a_n and b_n are Mie scattering coefficients which are determined by boundary conditions on the particle surfaces.

The Legendre functions can be written in terms of associated Legendre polynomials of order n and degree unity:

$$\pi_n(\cos\theta) = P_n^{(1)}(\cos\theta) / \sin\theta \quad (3.5)$$

and

$$\tau_n(\cos\theta) = dP_n^{(1)}(\cos\theta) / d\theta. \quad (3.6)$$

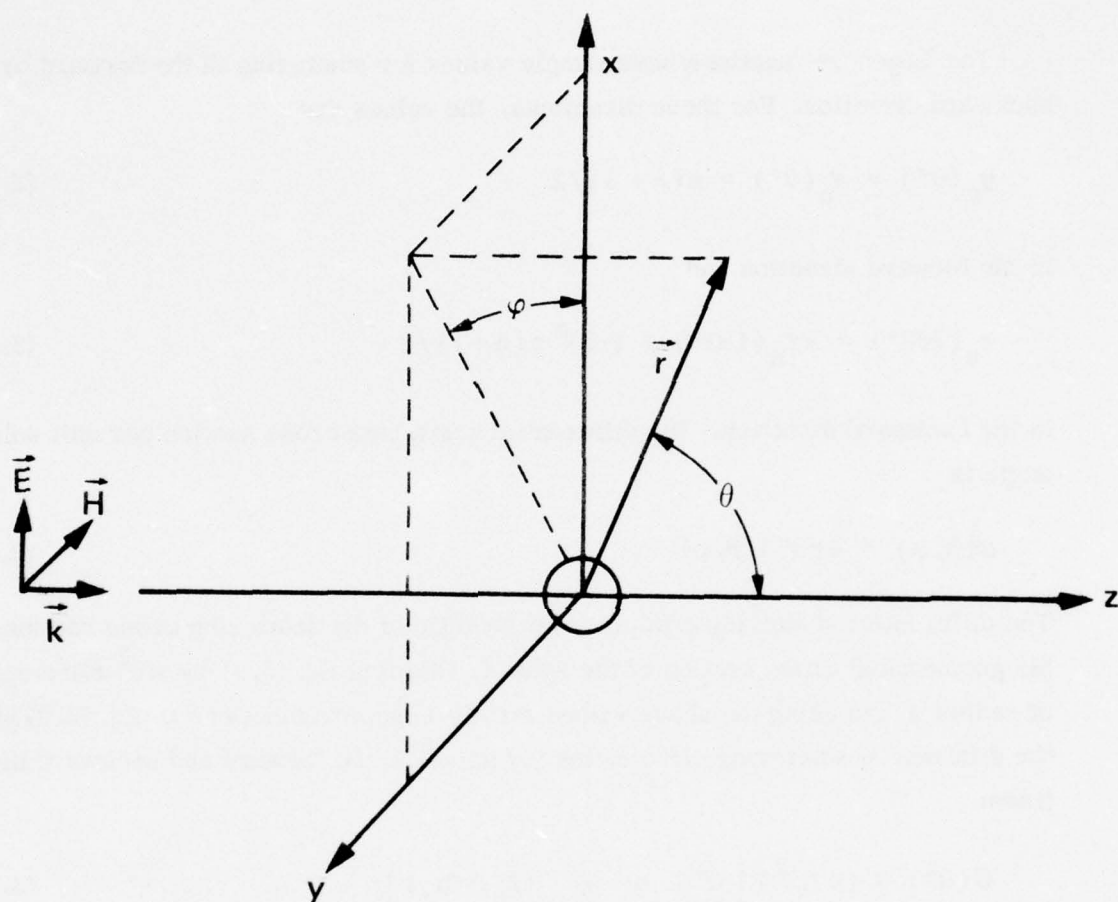


Fig. 3.1. Radiation propagating in the \hat{z} direction is scattered from a spherically symmetric object at the origin to the observation point (r, θ, ϕ) .

The associated Legendre polynomials can be expressed in terms of Legendre polynomials, P_n :

$$P_n^{(m)}(\eta) = (1 - \eta^2)^{m/2} d^m P_n(\eta) / d\eta^m . \quad (3.7)$$

The Legendre functions have simple values for scattering in the forward or backward direction. For these directions, the values are

$$\pi_n(0^\circ) = \tau_n(0^\circ) = n(n+1)/2 \quad (3.8a)$$

in the forward direction and

$$\pi_n(180^\circ) = -\tau_n(180^\circ) = (-1)^n n(n+1)/2 \quad (3.8b)$$

in the backward direction. The differential scattering cross section per unit solid angle is

$$\sigma(\theta, \varphi) = 4\pi r^2 I(\theta, \varphi) . \quad (3.9)$$

The differential scattering efficiency is the ratio of the scattering cross section to the geometrical cross section of the sphere. Dividing Eq. (3.9) by πa^2 for a sphere of radius a and using the above values for the Legendre functions in Eq. (3.8) yields the differential scattering efficiencies (or gains) in the forward and backward directions:

$$G(0^\circ) = (4/\alpha^2) \left| \sum_{n=1}^{\infty} n + \frac{1}{2} (a_n + b_n) \right|^2 \quad (3.10)$$

and

$$G(180^\circ) = (4/\alpha^2) \left| \sum_{n=1}^{\infty} n + \frac{1}{2} (-1)^n (b_n - a_n) \right|^2 \quad (3.11)$$

where α is the sphere size parameter

$$\alpha = 2\pi a/\lambda . \quad (3.12)$$

Similarly, simple expressions are obtained for the integrated efficiencies for scattering, Q_{sca} , and extinction, Q_{ext} :

$$Q_{\text{sca}} = (2/\alpha^2) \sum_{n=1}^{\infty} (2n+1) \left[|a_n|^2 + |b_n|^2 \right] \quad (3.13)$$

and

$$Q_{\text{ext}} = (2/\alpha^2) \sum_{n=1}^{\infty} (2n+1) \operatorname{Re} (a_n + b_n) , \quad (3.14)$$

where Re denotes the real part. The extinction efficiency gives the total energy lost from the incident beam to scattering and absorption. The absorption efficiency is obtained by taking the difference between the extinction efficiency and scattering efficiency.

It remains to calculate the Mie scattering coefficients, a_n and b_n . These coefficients are associated with the various multipole moments induced in the sphere by the incident radiation with a_1 representing the electric dipole moment, a_2 representing the electric quadrupole moment, b_1 representing the magnetic dipole moment, etc.

For a homogeneous sphere having a complex refractive index $m = n - ik$, the Mie scattering coefficients are

$$a_n = \frac{\psi'_n(m\alpha)\psi_n(\alpha) - m\psi_n(m\alpha)\psi'_n(\alpha)}{\psi'_n(m\alpha)\zeta_n(\alpha) - m\psi_n(m\alpha)\zeta'_n(\alpha)} \quad (3.15)$$

and

$$b_n = \frac{m\psi'_n(m\alpha)\psi_n(\alpha) - \psi_n(m\alpha)\psi'_n(\alpha)}{m\psi'_n(m\alpha)\zeta_n(\alpha) - \psi_n(m\alpha)\zeta'_n(\alpha)} , \quad (3.16)$$

where primes denote derivatives with respect to the arguments of the functions. The function ζ_n is a linear combination of functions:

$$\zeta_n = \psi_n + iX_n , \quad (3.17)$$

where ψ_n and X_n are Riccati-Bessel functions of the first and second kind.

In the limit of an infinite refractive index (perfectly conducting sphere), the above expressions for the Mie scattering coefficients reduce to

$$a_n = \psi'_n(\alpha) / \zeta'_n(\alpha) \quad (3.18)$$

and

$$b_n = \psi_n(\alpha) / \zeta_n(\alpha) \quad (3.19)$$

Notice that these equations, also the various scattering efficiencies, involve only the particle size parameter $\alpha = 2\pi a / \lambda$. Hence parameters for perfectly conducting spheres provide limiting values for testing results for spheres having finite optical constants.

The Mie scattering coefficients for a coated sphere are more complex than those of a homogeneous sphere because of the necessity of satisfying boundary conditions at the coating-core interface as well as at the outer surface. A coated sphere having core radius a and total radius b is depicted in Fig. 3.2. Optical constants in the core and coating are denoted by subscripts 1 and 2, respectively. Expressions for the Mie scattering coefficients given in Kerker²³ are incorrect. The corrected coefficients are given by the determinantal expressions:

$$a_n = \frac{\begin{vmatrix} m_1 \psi'_n(m_2 \alpha) & m_1 \chi'_n(m_2 \alpha) & m_2 \psi'_n(m_1 \alpha) & 0 \\ \psi_n(m_2 \alpha) & \chi_n(m_2 \alpha) & \psi_n(m_1 \alpha) & 0 \\ \psi'_n(m_2 \nu) & \chi'_n(m_2 \nu) & 0 & m_2 \psi'_n(\nu) \\ \psi_n(m_2 \nu) & \chi_n(m_2 \nu) & 0 & \psi_n(\nu) \end{vmatrix}}{\begin{vmatrix} m_1 \psi'_n(m_2 \alpha) & m_1 \chi'_n(m_2 \alpha) & m_2 \psi'_n(m_1 \alpha) & 0 \\ \psi_n(m_2 \alpha) & \chi_n(m_2 \alpha) & \psi_n(m_1 \alpha) & 0 \\ \psi'_n(m_2 \nu) & \chi'_n(m_2 \nu) & 0 & m_2 \zeta'_n(\nu) \\ \psi_n(m_2 \nu) & \chi_n(m_2 \nu) & 0 & \zeta_n(\nu) \end{vmatrix}} \quad (3.20)$$

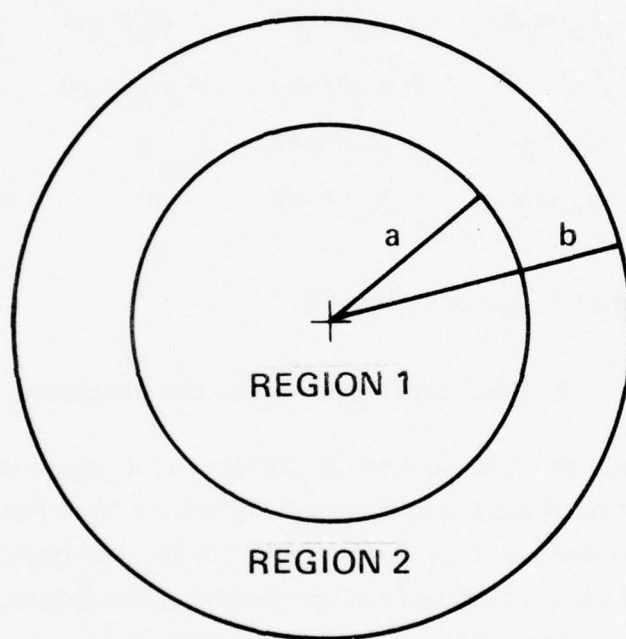


Fig. 3.2. Coated sphere having core radius, a , and total radius, b .

and

$$b_n = \frac{\begin{vmatrix} m_1 \psi'_n(m_2 \alpha) & m_1 \chi'_n(m_2 \alpha) & \psi'_n(m_1 \alpha) & 0 \\ m_1^2 \psi_n(m_2 \alpha) & m_1^2 \chi_n(m_2 \alpha) & m_2 \psi_n(m_1 \alpha) & 0 \\ \psi'_n(m_2 \nu) & \chi'_n(m_2 \nu) & 0 & \psi'_n(\nu) \\ \psi_n(m_2 \nu) & \chi_n(m_2 \nu) & 0 & m_2 \psi_n(\nu) \end{vmatrix}}{\begin{vmatrix} m_1 \psi'_n(m_2 \alpha) & m_1 \chi'_n(m_2 \alpha) & \psi'_n(m_1 \alpha) & 0 \\ m_1^2 \psi_n(m_2 \alpha) & m_1^2 \chi_n(m_2 \alpha) & m_2 \psi_n(m_1 \alpha) & 0 \\ \psi'_n(m_2 \nu) & \chi'_n(m_2 \nu) & 0 & \zeta'_n(\nu) \\ \psi_n(m_2 \nu) & \chi_n(m_2 \nu) & 0 & m_2 \zeta_n(\nu) \end{vmatrix}} \quad (3.21)$$

where $\alpha = 2\pi a/\lambda$ and $\nu = 2\pi b/\lambda$.

B. Practical Computational Considerations

The calculation of the scattering efficiency of a sphere involves straightforward computation of the Mie scattering coefficients from Eqs. (3.20) and (3.21) for a coated sphere [or Eqs. (3.15) and (3.16) for a homogeneous sphere] and substitution of these coefficients in the desired scattering efficiency sum in Eqs. (3.10), (3.11), (3.13), or (3.14). Factors requiring consideration are: the number of terms required in the Mie series, an efficient and accurate means of calculating the Riccati-Bessel functions, and modifications to the formulas to handle overflows that occur with the large values of the refractive index for metals.

The number of terms required in the Mie series is dependent primarily on the ratio of the sphere radius to the incident radiation wavelength and to a lesser extent on the sphere refractive index. To determine the number, the magnitudes of the first eleven scattering coefficients for a perfectly conducting sphere of radius b were calculated. The logarithms of these terms are plotted as a function of $kb = 2\pi b/\lambda$ in Figs. 3.3 and 3.4. Prior to their initial approach to unit magnitude,

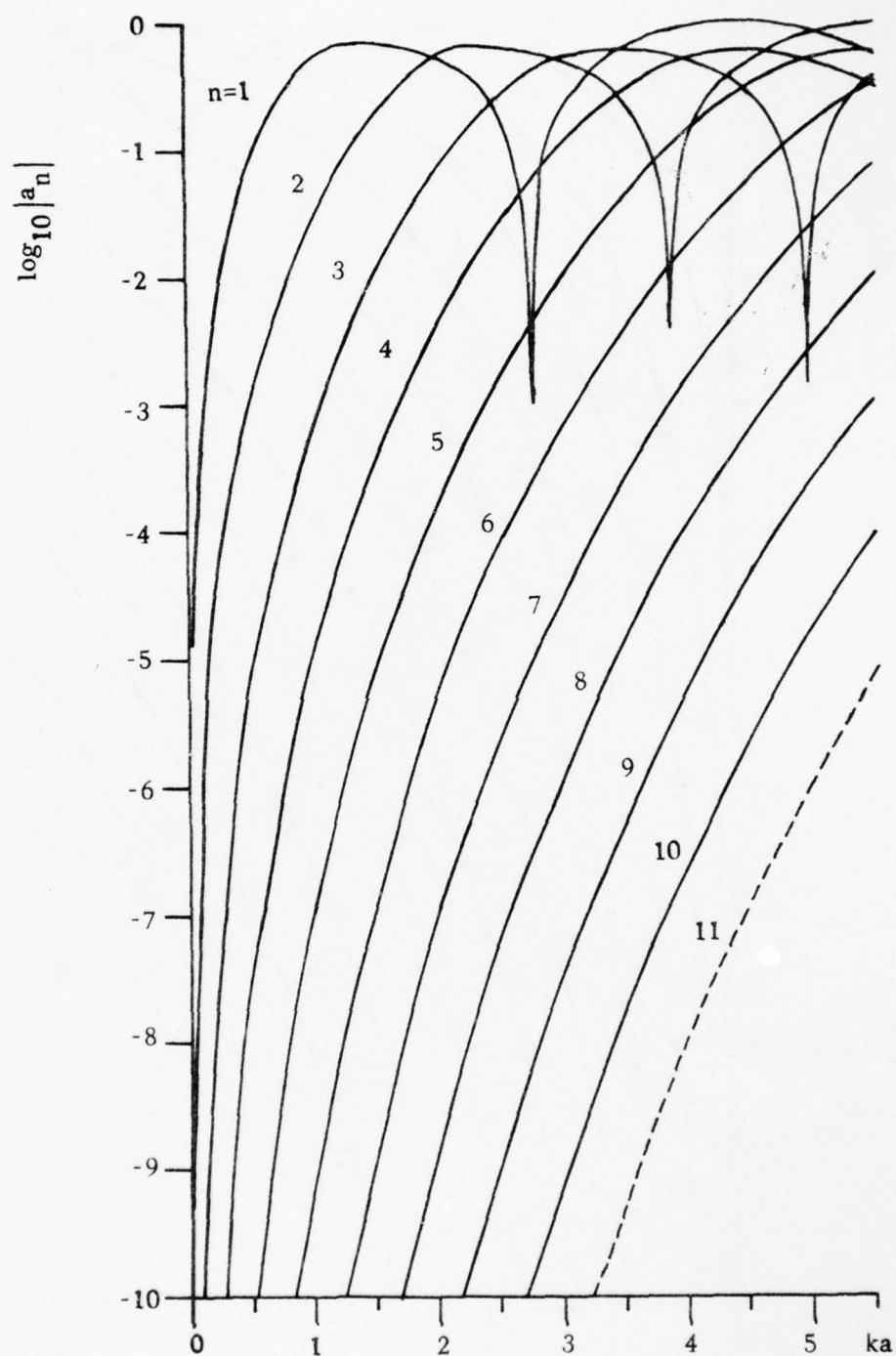


Fig. 3.3. Magnitude of the electric-multipole scattering coefficients a_n of a perfectly conducting sphere as a function of the sphere size parameter ka .

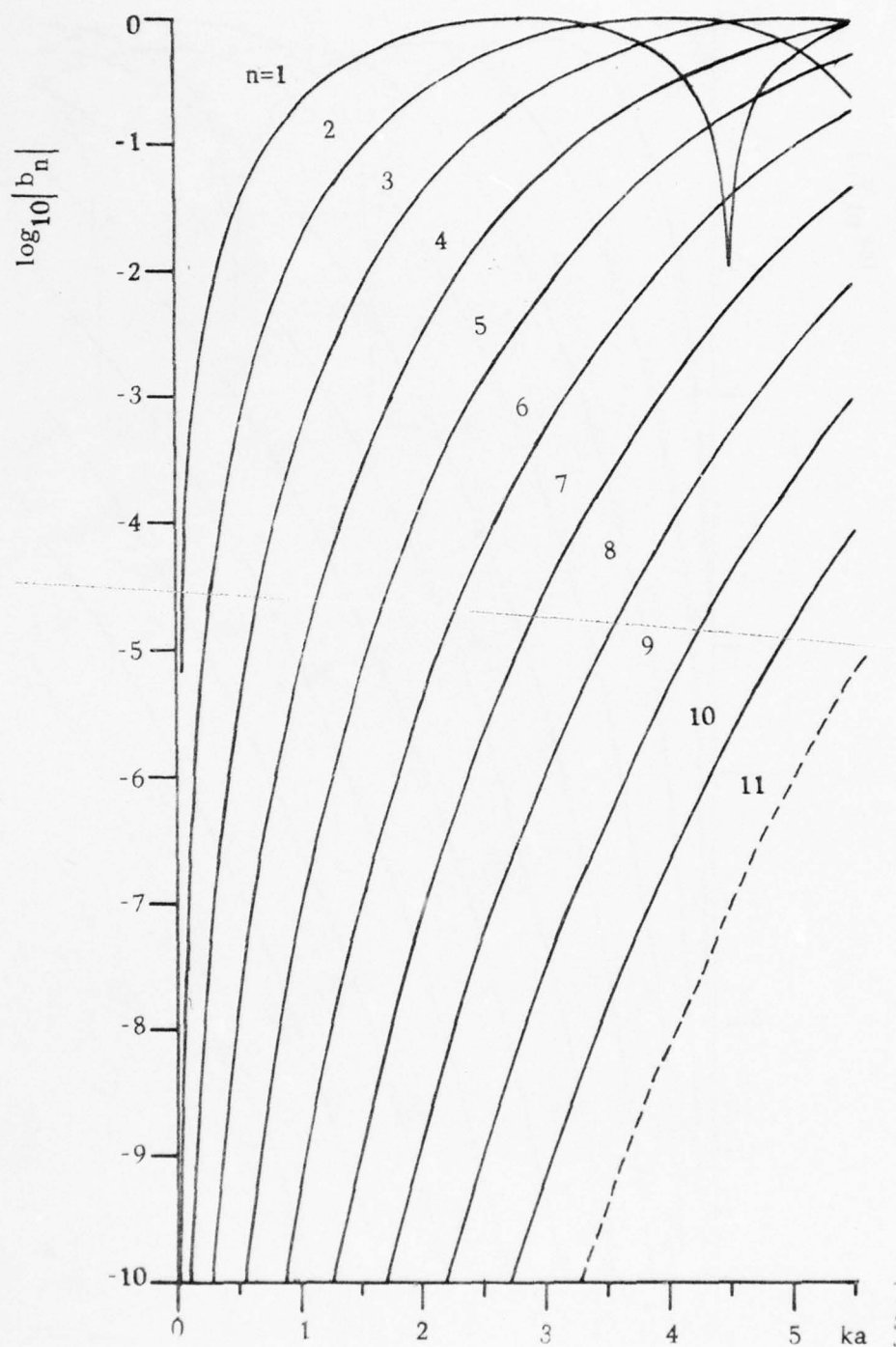


Fig. 3.4. Magnitude of the magnetic-multipole scattering coefficients b_n of a perfectly conducting sphere as a function of the sphere size parameter ka .

the scattering coefficients are seen to increase with increasing kb and to decrease with increasing order. In the following calculations, the Mie series has been truncated at ten terms. For sizes and wavelengths in the range of Figs. 3.3 and 3.4, the truncation error in the Mie series is of the order of a_{11} or b_{11} as is indicated by the dashed curves.

The above estimate of the truncation error should also be approximately valid for dielectric-coated metallic spheres in this size and wavelength region. An examination of the scattering coefficients of a few dielectric-coated metallic spheres reveals that, even with thick coatings of $b/a = 1.4$, the major differences from a perfectly conducting sphere occur in the region near magnitude unity. In the region where the scattering coefficients are small, which determines the truncation error, the coefficients are quite similar.

Most of the numerical subtleties in the program are contained in the algorithms for calculating the Riccati-Bessel functions and their derivatives. Rather than using explicit algorithms for calculating all orders of the Riccati-Bessel functions and their derivatives, two of the orders are calculated explicitly with recursion relations being used to generate the remaining orders and all derivatives. Routines are needed only for the psi and chi functions since the zeta function is a linear combination of these functions, as is given in Eq. (3.17).

Recursion relations for X_n are stable in the forward direction, so X_1 and X_2 are evaluated using

$$X_1(z) = \sin z + \cos z / z \quad (3.22)$$

and

$$X_2(z) = -\cos z + 3X_1(z)/z, \quad (3.23)$$

except for arguments having large imaginary parts as is discussed later. Use of the recursion relation

$$X_{n+1} = (2n+1)X_n/z - X_{n-1} \quad (3.24)$$

yields orders two through ten.

Recursion relations for ψ_n are unstable in the forward direction, so the backward recursion relation

$$\psi_{n-1} = (2n+1) \psi_n / z - \psi_{n+1} \quad (3.25)$$

is used with starting functions ψ_9 and ψ_{10} to generate orders one through eight.

Derivatives are obtained using

$$\psi'_n = \psi_{n+1} - \frac{(n+1)}{z} \psi_n \quad (3.26)$$

for orders one through nine and

$$\psi'_n = \psi_{n-1} - (n/z) \psi_n \quad (3.27)$$

for order ten. These same derivative equations are also valid for χ'_n when χ is substituted for ψ .

Algorithms involving sines and cosines multiplied by polynomials in z^{-1} can be written for the starting functions ψ_9 and ψ_{10} . However in contrast to Eqs. (3.22) and (3.23) for χ_1 and χ_2 , the analogous algorithms for ψ_9 and ψ_{10} are inaccurate at small arguments, in addition to having difficulties at large imaginary arguments as discussed later. For arguments greater than about twice the subscript, but not having too large an imaginary part, the most accurate algorithms are:

$$\begin{aligned} \psi_9 = & \left[45 - 13860/z^2 + 945945/z^4 \right. \\ & \left. - 16216200/z^6 + 34459425/z^8 \right] \sin z/z \\ & - \left[1 - 990/z^2 + 135135/z^4 \right. \\ & \left. - 4729725/z^6 + 34459425/z^8 \right] \cos z, \quad |z| \geq 20.0 \end{aligned} \quad (3.28)$$

and

$$\begin{aligned} \psi_{10} = & - \left[1 - 1485/z^2 + 315315/z^4 - 18918900/z^6 \right. \\ & \left. + 310134825/z^8 - 654729075/z^{10} \right] \sin z \\ & - \left[55 - 25740/z^2 + 2837835/z^4 \right. \\ & \left. - 91891800/z^6 + 654729075/z^8 \right] \cos z/z, \quad |z| \geq 20.0. \end{aligned} \quad (3.29)$$

At small z , the terms in the z^{-1} polynomials become very large and accuracy is lost in taking the difference of nearly equal large numbers. In this region it is more accurate to expand the sines and cosines in power series which yield the over-all power series:

$$\psi_n(z) = \frac{z^{n+1}}{1 \cdot 3 \cdot 5 \cdots (2n+1)} \left[1 - \frac{\frac{1}{2} z^2}{1! (2n+3)} + \frac{\left(\frac{1}{2} z^2\right)^2}{2! (2n+3)(2n+5)} - \cdots \right], |z| < 20.0. \quad (3.30)$$

The power series in Eq. (3.30) is not used for all magnitudes z including those greater than 20 because it is inefficient and inaccurate due to the large number of terms required in the series with large arguments. The cross-over point in accuracy between the two methods was determined by computing ψ_9 and ψ_{10} both ways for values of z from $|z| = 10$ to $|z| = 30$ and locating the point where they agreed to greatest number of decimals. On the IBM370 computer, run in double precision, the results of the two methods agree to six places in the region around the cross-over point. This six-significant-figure limitation near the cross-over point is the major limiting factor in the accuracy of the scattering calculation in the region.

As mentioned above, there are additional difficulties in both Riccati-Bessel functions for arguments having large imaginary parts, as occurs for those containing the refractive index of a metal. In this case the sine and cosine factors in the Riccati-Bessel function algorithms may have magnitudes greater than the capacity of the computer. To avoid this difficulty, a large positive exponential term from the imaginary part of the sine and cosine arguments is factored out.

Consider first the modifications required for a metallic core sphere having a complex refractive index m_1 . Using the convention where the imaginary part of the refractive index is negative, the function argument involving the core refractive index is written

$$m_1 \alpha = u - iv, \quad (3.31)$$

where both u and v are positive. The cosine of this term is

$$\cos(m_1 \alpha) = \left[e^{i(u-iv)} + e^{-i(u-iv)} \right] / 2. \quad (3.32)$$

Factoring out the term having the divergent exponential part yields

$$\cos(m_1 \alpha) = \left[e^{(v+iu)/2} \right] \left[1 + e^{-2v} e^{-2iu} \right] . \quad (3.33)$$

Similarly the sine of this argument is written

$$\sin(m_1 \alpha) = \left[e^{(v+iu)/2} \right] \left[(-i) \left(1 - e^{-2v} e^{-2iu} \right) \right] . \quad (3.34)$$

Notice that the same divergent factor appears in the first square-bracketed term of both Eqs. (3.33) and (3.34). Since the Riccati-Bessel functions are linear in sine and cosine, this same term can be factored from these functions, and their derivatives, leaving the second square-bracketed terms in place of the sine and cosine. Referring to Eqs. (3.20) and (3.21) for the Mie scattering coefficients, the argument $m_1 \alpha$ appears only in the third columns of each determinant. By the rules of matrix algebra, the divergent term can also be factored from the determinants. When this is done, terms factored from the numerator and denominator cancel. Thus, the divergent term is entirely compensated by replacing the sines and cosines in the Riccati-Bessel functions of the core sphere by the second square-bracketed terms in Eqs. (3.33) and (3.34). No other changes are necessary.

Additionally, it is desirable to expand the capabilities of the computer program to handle metal-clad spheres as well as dielectric-coated spheres. In this case it is necessary to remove divergences occurring in Riccati-Bessel functions having arguments $m_2 \alpha$ and $m_2 \nu$. For convenience, only a real factor $e^{v/2}$ is removed from the algorithms, for example

$$\cos(m_2 \alpha) = \left[e^{v_a/2} \right] \left[e^{iu_a} + e^{-iu_a} e^{-v_a} \right] . \quad (3.35)$$

Functions involving the coating refractive index are found in the first two columns of the determinants in Eqs. (3.20) and (3.21). In contrast to the core functions, there is no common factor in each column because both arguments $m_2 \alpha$ and $m_2 \nu$ appear in each column. However, when the determinants are expanded, there are two over-all common factors $1/2 \exp(v_a)$ and $1/2 \exp(v_b)$ from two arguments. These common factors are made possible by the zeros in the third and fourth

columns. As with the core functions, the divergent factors from the numerators and denominators of the scattering coefficients cancel, and it is only necessary to replace the sines and cosines in the Riccati-Bessel functions by terms similar to the second square-bracketed term in Eq. (3.35).

With the coating functions it is also necessary to remove the same factor from the power series algorithm used for small arguments of the psi function in order to keep functions computed from this algorithm normalized with respect to the other coating functions. Otherwise erroneous results occur in the region where $|m_2\alpha| < 20.0$ or $|m_2\nu| < 20.0$. Such a difficulty does not occur with the psi function of the core.

Besides the difficulties with overflows in the algorithms, in some cases underflows occurred in products of functions in the expanded determinant. These products were examined and were found to be negligible with respect to other terms in the expanded determinants. Hence, the underflow difficulty was overcome, with no loss in accuracy, by testing for an underflow and by setting underflowing products equal to zero.

A listing of the computer program is given in the appendices along with a further description of the implementation of the above equations.

C. Tests of Program Accuracy

Four series of tests were made of the numerical accuracy of the program:

- 1) The Riccati-Bessel function subroutines were compared with published tables.
- 2) A few points on the computer-calculated scattering curves were compared in detail to a calculation on a hand calculator.
- 3) It was verified that the coated-sphere formulas reproduced the homogeneous sphere results in the proper limits.
- 4) Scattering results of the coated-sphere calculation were compared with previously published curves.

1. To test the accuracy of the Riccati-Bessel function subroutines, both algorithms used for small and large arguments were used to generate ψ_9 and ψ_{10} for a large number of pure real and pure imaginary arguments. Recursion relations were used to generate ψ_1 through ψ_8 . Since tables of Riccati-Bessel

functions were not available, these functions were converted to spherical Bessel functions j_n and y_n using

$$\psi_n(z) = z j_n(z) \quad \text{and} \quad \chi_n(z) = z y_n(z) \quad . \quad (3.36)$$

Values of spherical Bessel functions are available in Tables 10.1, 10.2, and 10.5 of Abramowitz and Stegun.²⁶ Less extensive tests were made of the χ_n functions since only a single algorithm is needed for these functions.

For large z the expressions for ψ_9 and ψ_{10} are quite complex and the available tables are rather sparse (only $z = 20, 20i, 50, 50i, 100, 100i$). Additional tests were made of these functions by generating ψ_1 and ψ_2 using back-recursion relations from calculated values of ψ_9 and ψ_{10} . These values of ψ_1 and ψ_2 were compared to other values calculated directly from their analytic expressions. Values of ψ_1 and ψ_2 calculated by both methods agreed to six decimal places near $|z| = 20$ with improvement to ten places for $|z| < 10$ or $|z| > 30$. This is the same accuracy that is expected for the starting functions ψ_9 and ψ_{10} . Hence besides testing the starting function, these results indicate that no accuracy is lost in the use of the recursion relations.

2. At a few selected points on the scattering curves, the complete calculation was carefully paralleled step by step by a tedious hand calculation. The agreement of these calculations gives us great confidence in the over-all computational procedure. In cases where products of Bessel functions produced underflows in the computer, this calculation revealed that there were always additional non-negligible terms that summed with the underflowing terms so that there is no loss of accuracy in setting the underflowing parts to zero.

3. As an additional test of the over-all program, it was verified that the coated-sphere program reproduced the homogeneous sphere results in the appropriate limits. Besides providing a test of the formulas for the scattering coefficients, this procedure also tests the Riccati-Bessel function subroutines since the coated sphere coefficients involve more complex products than the homogeneous sphere coefficients. The limit, b finite and $a = 0$, is not a proper homogeneous sphere limit of the coated-sphere formulas. When the electromagnetic boundary value problem was solved at $r = a$, solutions in the coating involve

both psi and chi functions, but in the core sphere only psi functions are allowed since chi functions are singular at the origin. Hence the limit $a = 0$ cannot be taken since singular chi functions would be introduced into the region containing the origin.

The homogeneous sphere limit was taken in the following five cases:

- metal core, vacuum coating, $b = a$
- metal core, arbitrary coatings, $b = a$
- metal core, vacuum coating, $b \neq a$
- metal core, same metal coating, $b \neq a$
- dielectric core, same dielectric coating, $b \neq a$.

In all limits the results agreed within the six-significant-figure accuracy of the program.

4. There are no previous calculations of scattering from a dielectric-coated metallic sphere available for comparison to our results. Previous investigators have approximated homogeneous metallic spheres by a perfectly conducting sphere. Scharfman has studied dielectric-coated perfectly conducting spheres in the region near $ka = 1.0$.²⁷ In the course of our computer calculation, scattering from perfectly conducting spheres of radii a and b was calculated for comparison to the coated-sphere results. Our calculations for a perfectly conducting sphere agree with our own hand calculations, Fig. 4.27 of Kerker,²³ and Scharfman.²⁷ Our coated-sphere results presented in the following section agree with Scharfman²⁷ with the differences being within the differences of a perfectly conducting sphere and an actual metallic sphere.

For comparison to a sphere with finite optical constants, a dielectric sphere coated with the same dielectric was compared to the homogeneous dielectric sphere curve in Fig. 4.34 of Kerker²³ using the following parameters:

$$m_1 = m_2 = 1.29 - i1.37, \quad b/a = 1.4.$$

There was good agreement between our calculated results and the curve in Kerker.²³

D. Results

Previous investigators have approximated scattering from metallic spheres by results for a perfect conductor. Scattering from coated perfect conductors has been considered by Scharfman²⁷ and by Rheinstein.²⁸ By making this approximation, the difficulties with large imaginary arguments of the Riccati-Bessel functions, as occur with actual metals, are avoided. As is shown in the following, scattering from a homogeneous, metallic sphere is well approximated by scattering from a perfect conductor. However for examination for the effects of dielectric coatings, it is necessary to consider actual metals since changes in the scattering for many coatings are less than the differences between an actual metal and a perfect conductor.

The results of four studies are presented in this section. First, scattering from a homogeneous, metallic sphere is compared to that from a perfect conductor. Second, a qualitative comparison is made of scattering from dielectric-coated metals and dielectric-coated perfect conductors. The similarity of the scattering of both types of coated spheres to scattering of a homogeneous, perfect conductor is determined. Third, differences in the scattering of metallic spheres due to various nondispersive, dielectric coatings is investigated quantitatively. Fourth, the effects of dispersion in the dielectric coatings are investigated by considering model coatings having a single Lorentzian-shaped absorption line. Scattering from an actual metal oxide coating and from small, homogeneous dielectric spheres is also calculated.

1. Homogeneous, metallic spheres.

The infinite refractive index of a perfect conductor is independent of the wavelength. Hence, scattering curves which are plotted as a function of the particle size parameter $\alpha = ka = 2\pi a/\lambda$ can be interpreted as being functions of changes in either the sphere radius or in the wavelength. This duality does not occur with actual metals because of dispersion in the optical constants. Metallic spheres considered in this section have fixed radii and a complex refractive index

$$m_2(\lambda_1 \text{ microns}) = -12.5 + 3.8\lambda - i(9.9 + 5.68\lambda) \quad . \quad (3.37)$$

The linear dependence of the refractive index on wavelength in Eq. (3.37) is a good fit to handbook values over the wavelength range of interest. In this region the reflectivity of the metal is at least 0.978, so that the perfect conductor is expected to be a good approximation.

Scattering from such a metal is compared to a perfect conductor of the same radius b in Fig. 3.5, where scattering from the metal is denoted by the solid curve and the perfect-conductor results are given by + symbols. The qualitative agreement is good with the oscillations in the two curves being in phase throughout the kb range from zero to four given in the figure. The magnitudes of the scattering agree in the region from kb equal to zero to the first peak. After the first peak the amplitude of the oscillations in the metal curve are greater than those in the perfect-conductor curve. At the two minima, the two scattering curves differ by approximately ten percent. The mean difference in the region between the first two peaks is four percent.

There appears to be no simple method for estimating the quantitative differences between the scattering from an actual metal and the scattering from a perfect conductor without doing the difficult Mie-theory calculation. Notice that the approximately ten percent difference in the two curves at the minima is much greater than the approximately two percent difference in the bulk reflectivities. At other points, the two curves cross and there is no difference in the scattering at these crossing points.

2. Qualitative results for coated metallic spheres.

Scharfman²⁷ has investigated the scattering efficiency in the ka region around the first peak of perfectly conducting spheres coated with nondispersive dielectrics. For high-index coatings with refractive indices greater than approximately 2.5, his scattering curves have a first peak at nearly the same position and of nearly the same magnitude as a perfectly conducting sphere of the same total radius, b . This result is somewhat surprising in view of the low reflectivity of the bulk dielectric material. Another limit is the limit of a vacuum coating (refractive index equal unity) where the scattering must approach the results for an uncoated sphere. This limit is approximately valid for thin coatings having refractive indices less than 1.6.

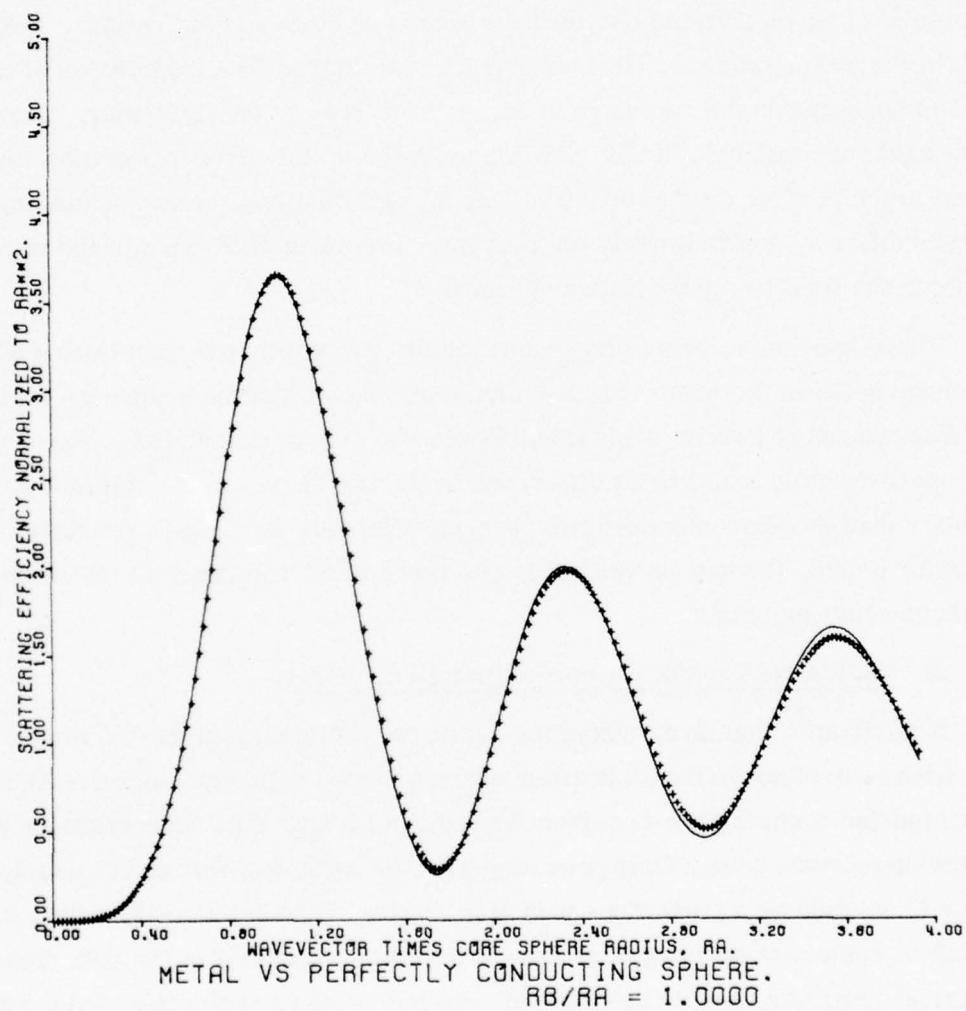


Fig. 3.5. Comparison of the scattering from a perfectly conducting sphere (symbols) and a metallic sphere (solid curve).

Metallic spheres coated with nondispersive absorbing and transparent dielectrics were examined to find whether similar qualitative rules are applicable in this case, and whether the rules are valid at other maxima and minima besides the first peak. This study was done graphically by preparing two plots of the scattering efficiency of the coated sphere which has core radius a and total radius b : In the first plot the scattering of the coated metallic sphere is normalized to the total geometrical cross section, πb^2 , and plotted as a solid curve as a function of kb . For comparison, the scattering efficiency of a perfectly conducting sphere of radius b is presented as a series of + symbols on the same axes. In the second plot, scattering from the coated metallic sphere is normalized to the core cross section, πa^2 , and plotted versus ka . Comparison in this case is made to a perfectly conducting sphere of radius a .

For the investigation of nondispersive, transparent coatings, a two-dimensional grid of coating thicknesses and refractive indices was used. At each of the three radius ratios, $b/a = 1.04, 1.004, 1.0004$, the scattering was calculated for the set of refractive indices $m_2 = 1.2, 1.35, 1.5, 1.75, 2.5, 3.25$, and 4.0 . Two plots of the scattering efficiency, normalized to πa^2 and πb^2 , are presented in Figs. 3.6 to 3.19 for the full set of refractive indices and the single radius ratio $b/a = 1.04$.

Consider first the scattering curves with $b/a = 1.04$ plotted in terms of the larger radius, i.e., kb abscissa. For the coating refractive index $m_2 = 4.0$ shown in Fig. 3.6, the curves for the coated, metallic sphere and the perfectly conducting sphere are in-phase, having maxima and minima at nearly the same positions. The curves differ in amplitude with the magnitude of the coated, metallic sphere curve being greater than the perfectly conducting curve at the maxima and smaller at the minima. The differences in amplitude increase with increasing kb .

As the coating refractive index decreases, the amplitude of the coated, metallic sphere scattering curve decreases and the period increases. With a coating refractive index of 1.5 shown in Fig. 3.14, the magnitude of the first peak of the coated sphere has decreased to the point where it is comparable to that of the perfect conductor. At kb values beyond the first peak, the coated sphere curve still has a larger amplitude than the perfect conductor curve.

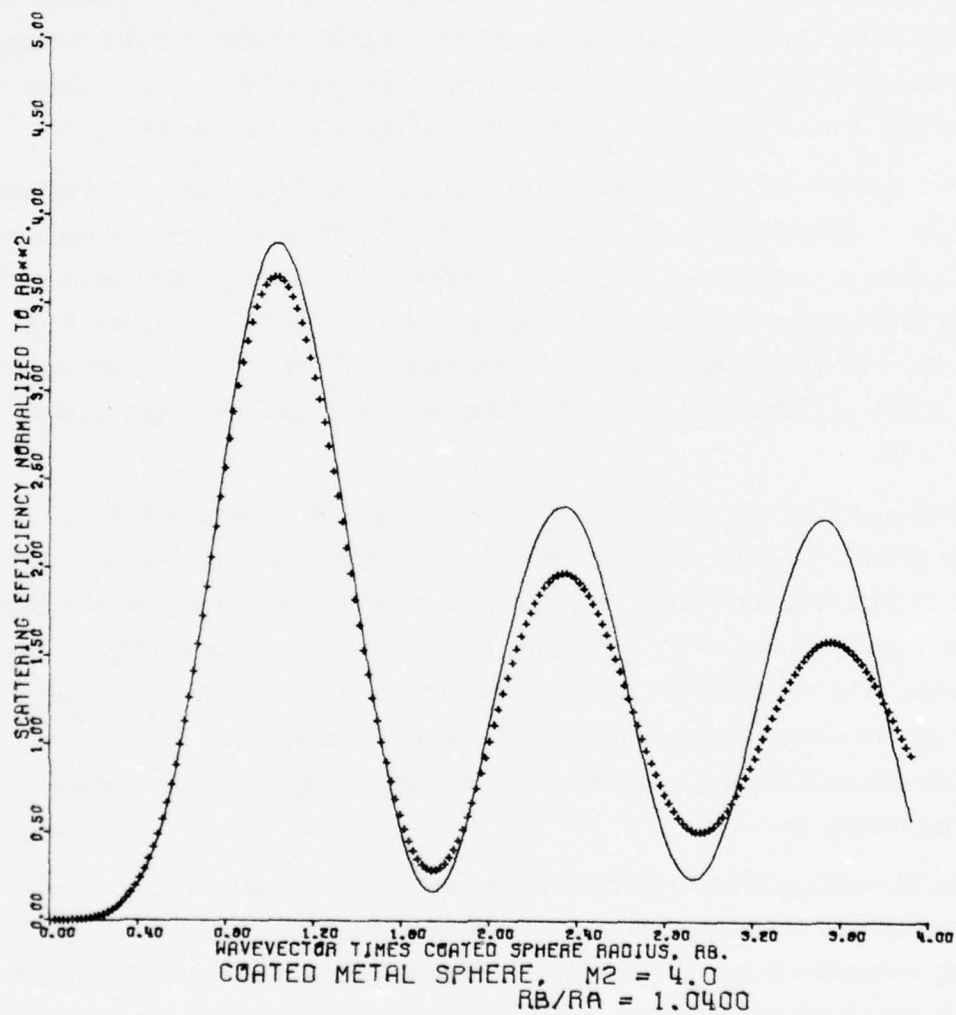


Fig. 3.6. Scattering from a coated metallic sphere normalized to the total cross-sectional area (solid curve) and scattering from a perfectly conducting sphere of radius b (symbols).

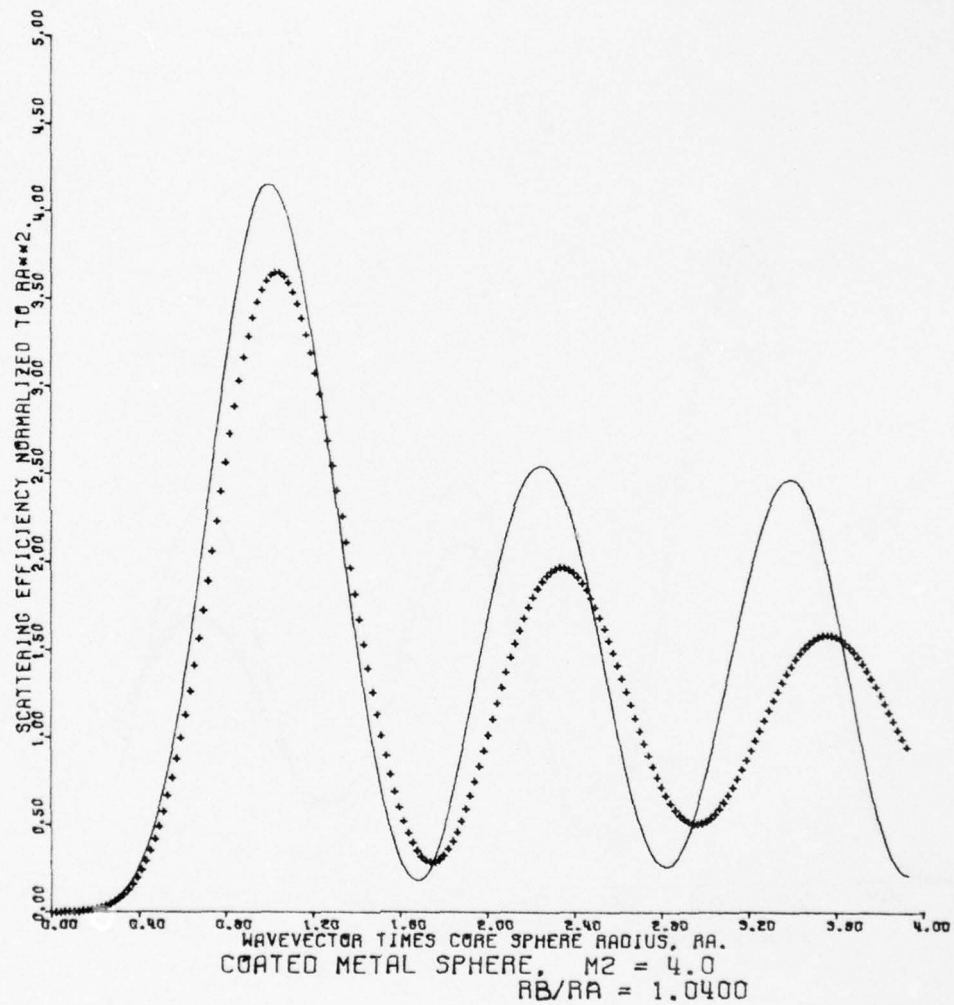


Fig. 3.7. Scattering from a coated metallic sphere normalized to the core cross-sectional area (solid curve) and scattering from a perfectly conducting sphere of radius a (symbols).

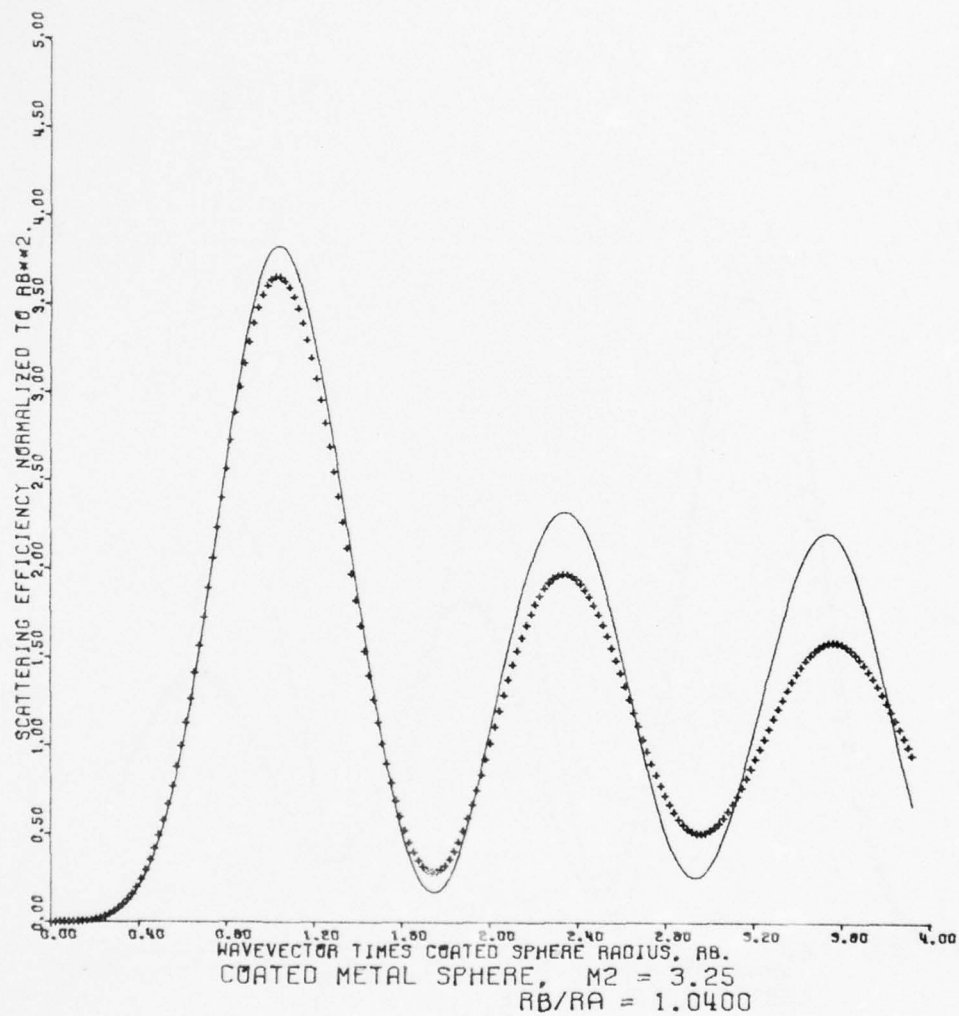


Fig. 3.8. Scattering from a coated metallic sphere normalized to the total cross-sectional area (solid curve) and scattering from a perfectly conducting sphere of radius b (symbols).

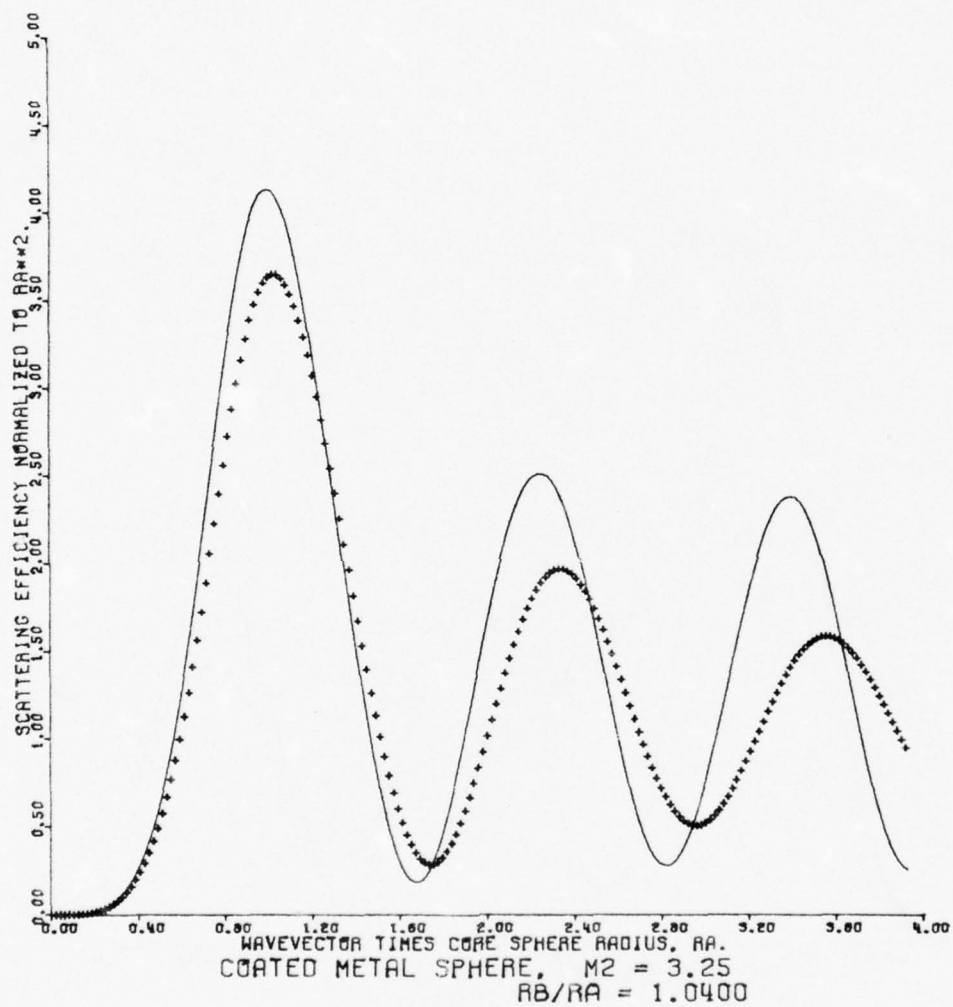


Fig. 3.9. Scattering from a coated metallic sphere normalized to the core cross-sectional area (solid curve) and scattering from a perfectly conducting sphere of radius a (symbols).

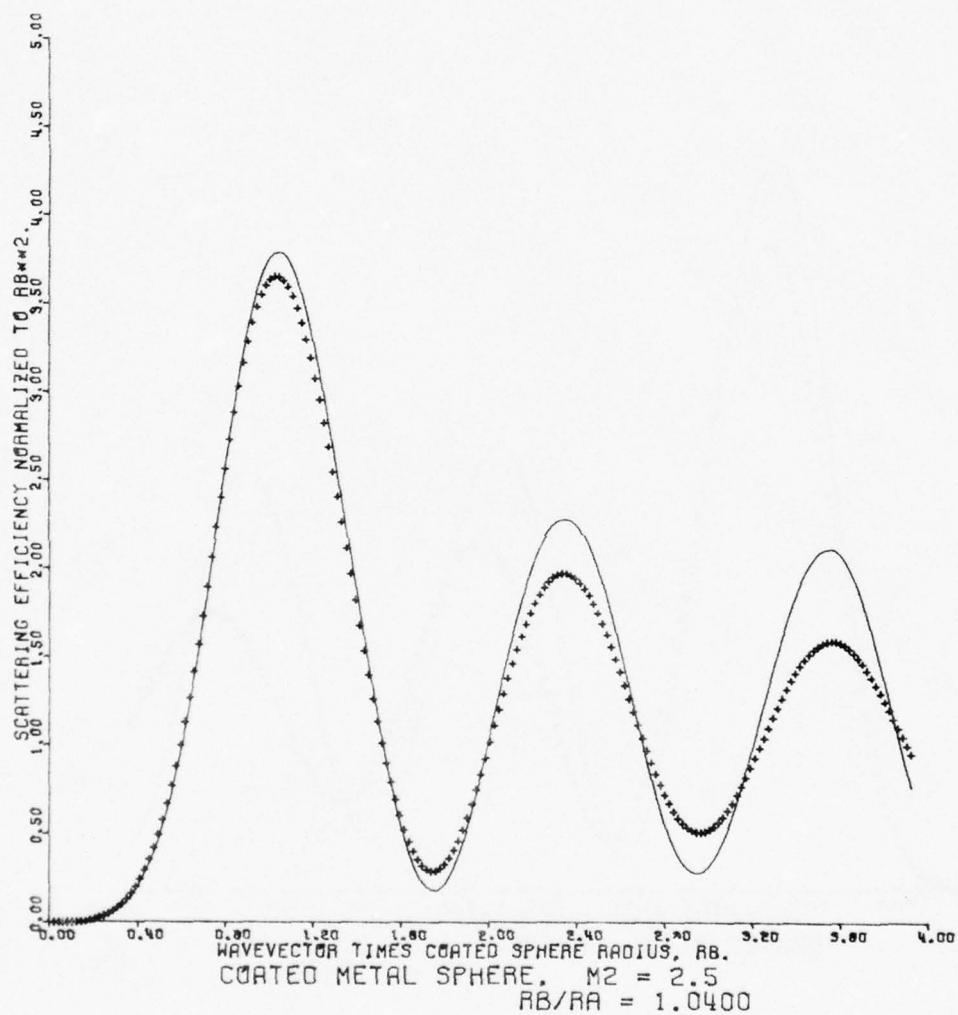


Fig. 3.10. Scattering from a coated metallic sphere normalized to the total cross-sectional area (solid curve) and scattering from a perfectly conducting sphere of radius b (symbols).

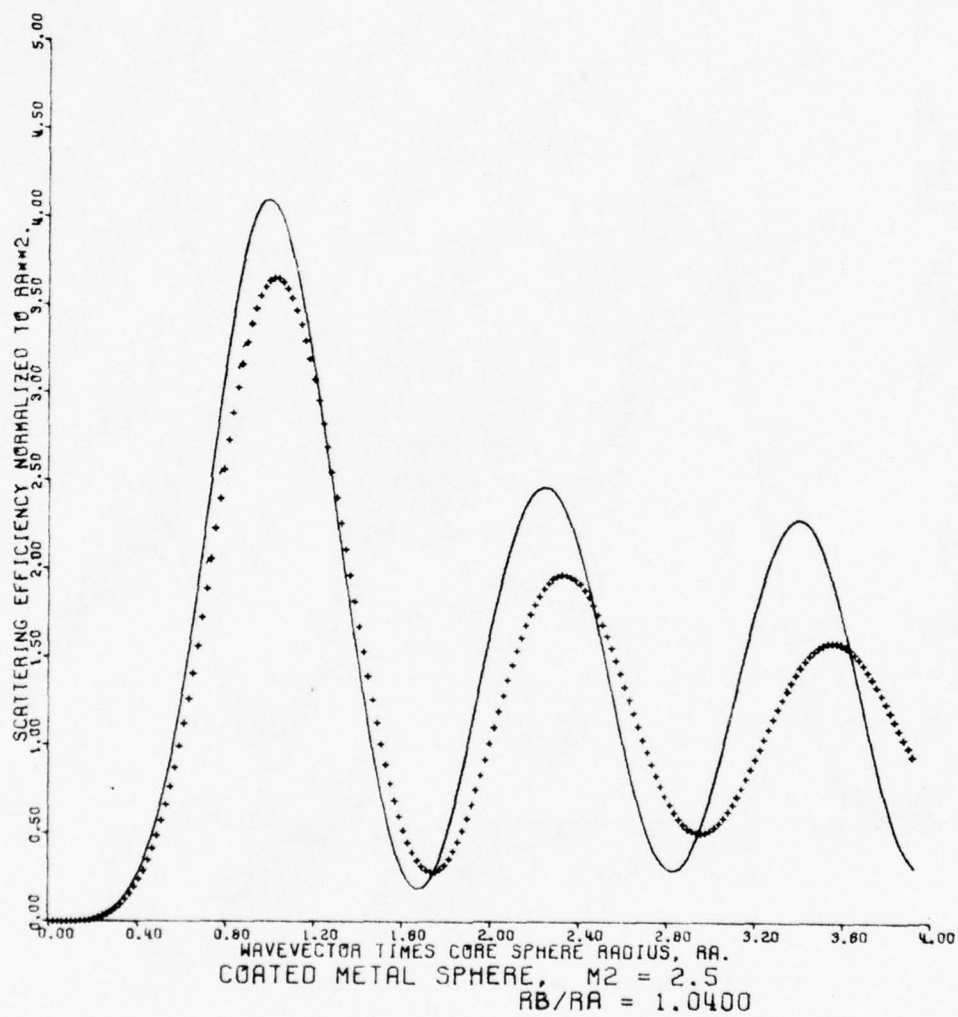


Fig. 3.11. Scattering from a coated metallic sphere normalized to the core cross-sectional area (solid curve) and scattering from a perfectly conducting sphere of radius a (symbols).

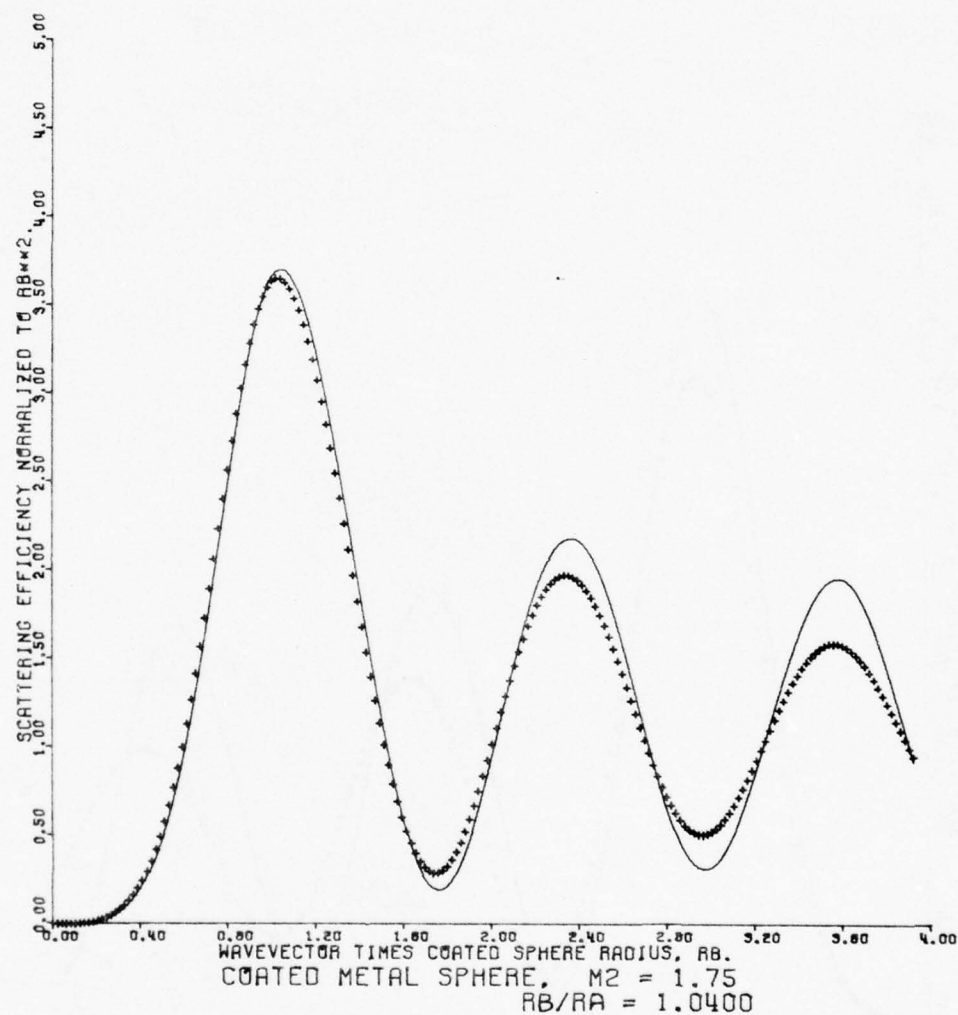


Fig. 3.12. Scattering from a coated metallic sphere normalized to the total cross-sectional area (solid curve) and scattering from a perfectly conducting sphere of radius b (symbols).

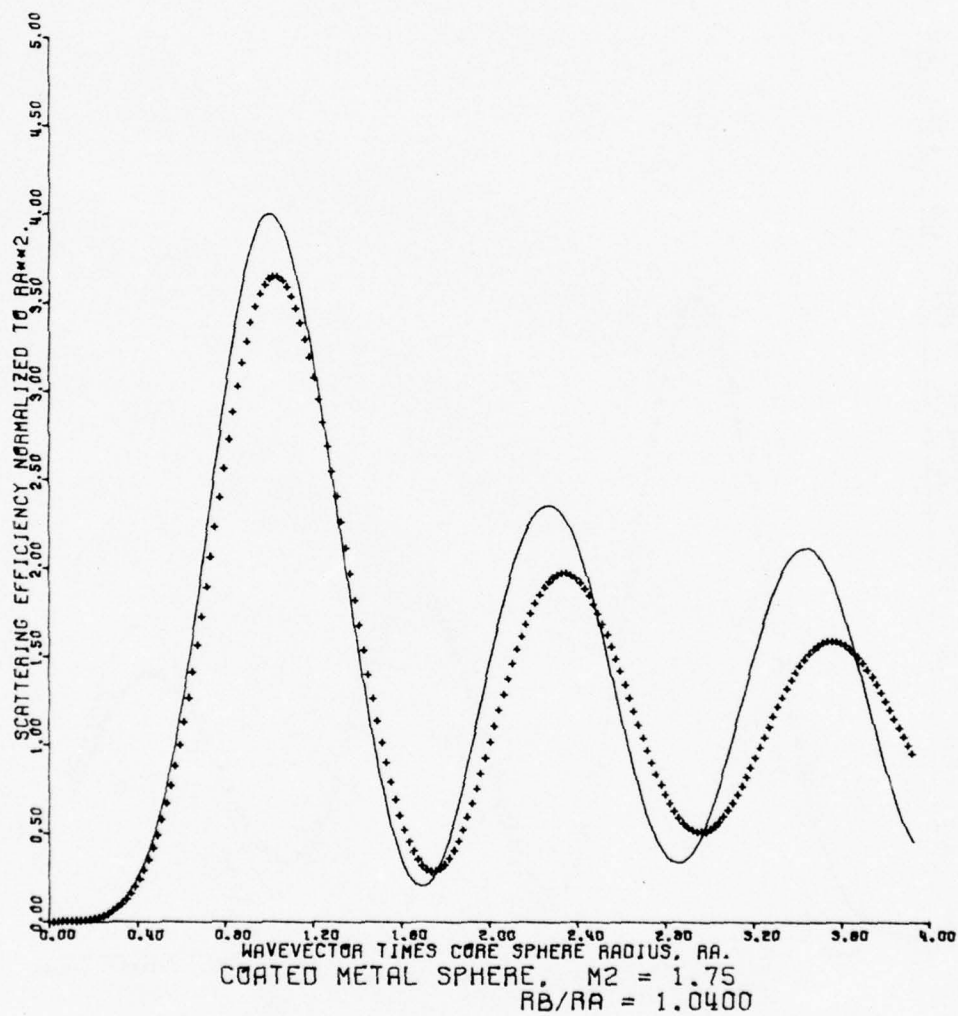


Fig. 3.13. Scattering from a coated metallic sphere normalized to the core cross-sectional area (solid curve) and scattering from a perfectly conducting sphere of radius a (symbols).

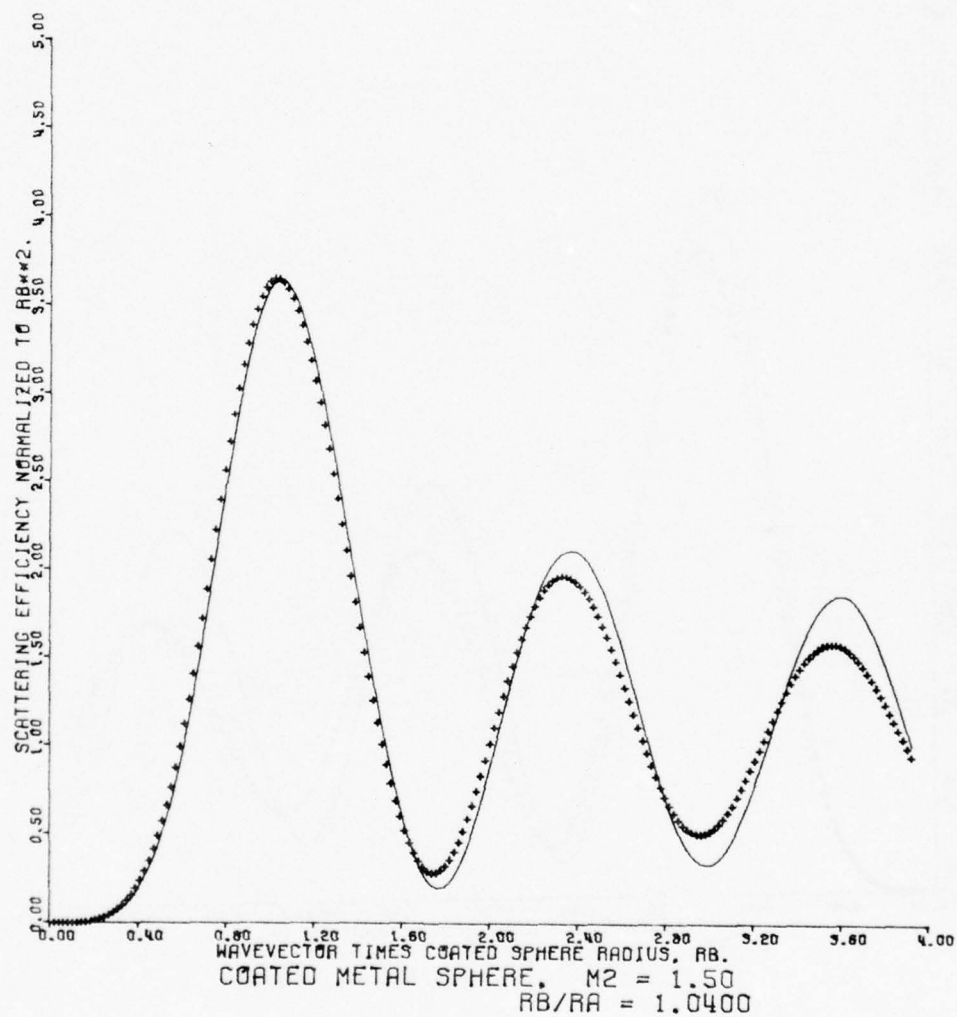


Fig. 3.14. Scattering from a coated metallic sphere normalized to the total cross-sectional area (solid curve) and scattering from a perfectly conducting sphere of radius b (symbols).

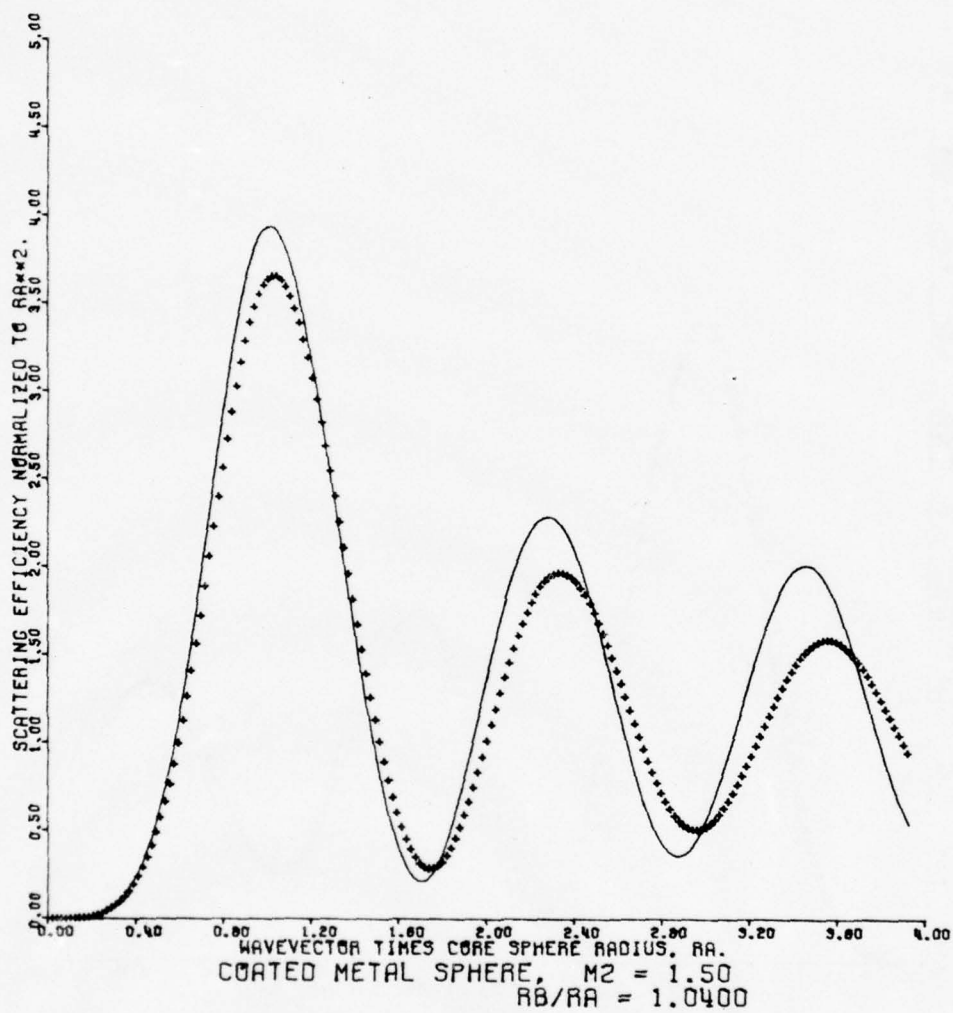


Fig. 3.15. Scattering from a coated metallic sphere normalized to the core cross-sectional area (solid curve) and scattering from a perfectly conducting sphere of radius a (symbols).

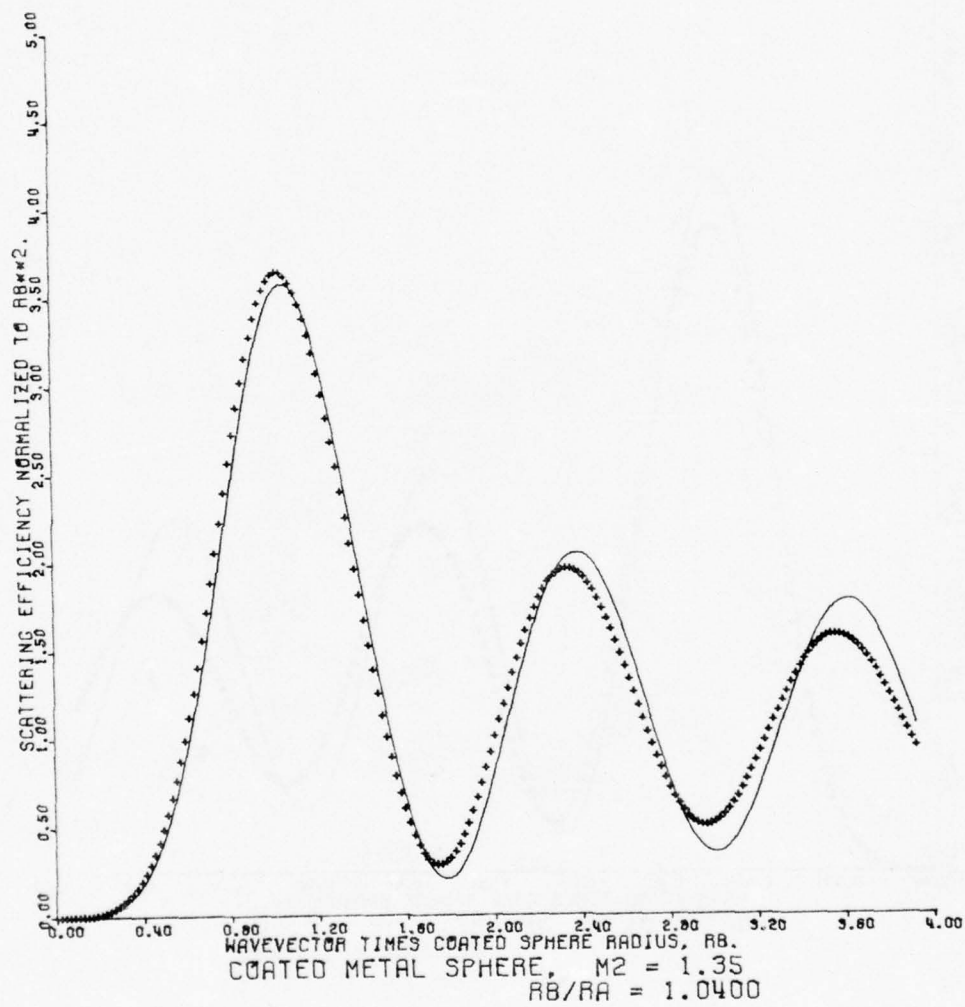


Fig. 3.16. Scattering from a coated metallic sphere normalized to the total cross-sectional area (solid curve) and scattering from a perfectly conducting sphere of radius b (symbols).

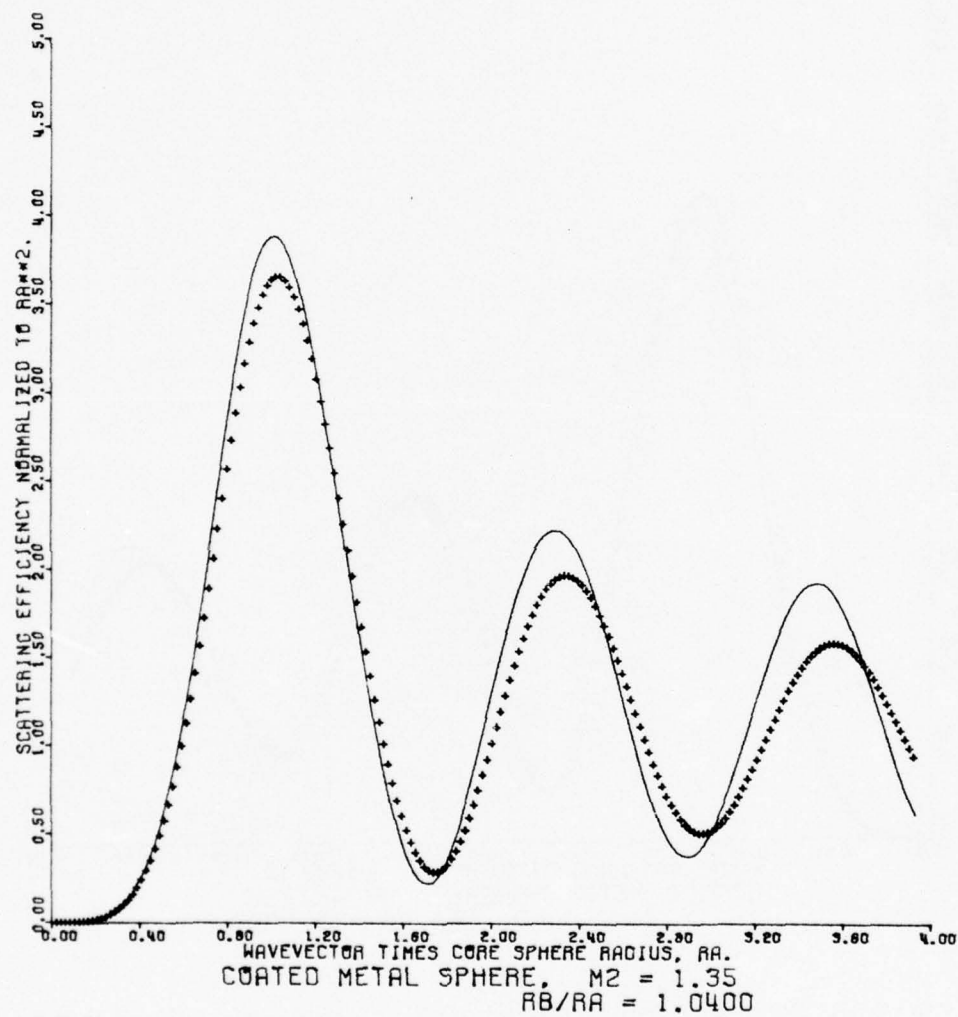


Fig. 3.17. Scattering from a coated metallic sphere normalized to the core cross-sectional area (solid curve) and scattering from a perfectly conducting sphere of radius a (symbols).

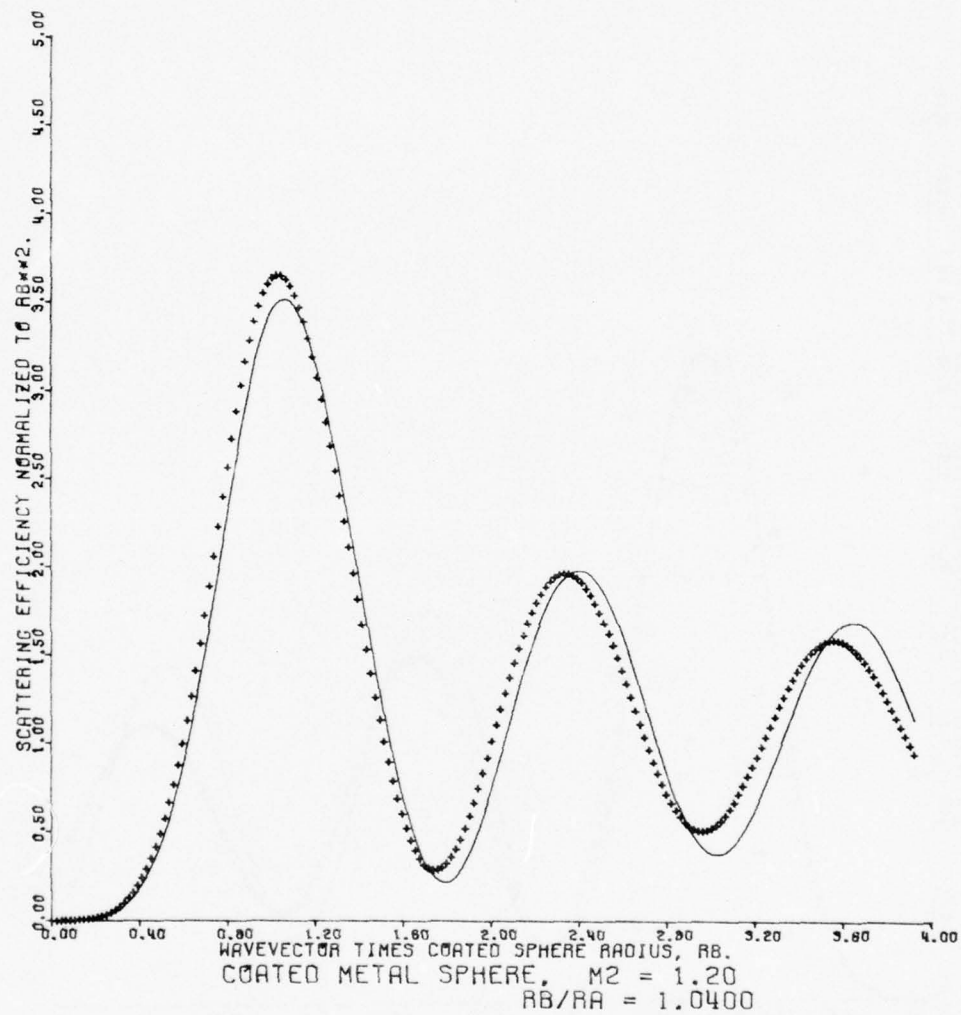


Fig. 3.18. Scattering from a coated metallic sphere normalized to the total cross-sectional area (solid curve) and scattering from a perfectly conducting sphere of radius b (symbols).

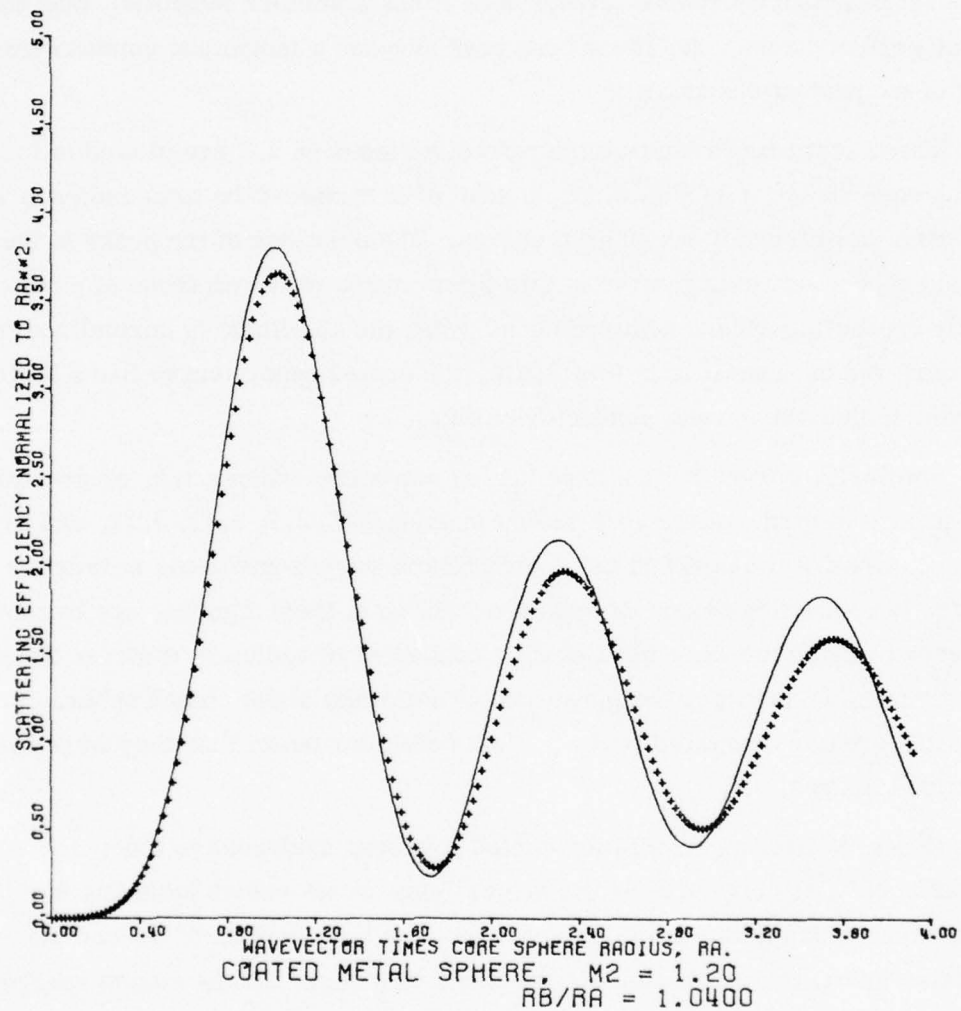


Fig. 3.19. Scattering from a coated metallic sphere normalized to the core cross-sectional area (solid curve) and scattering from a perfectly conducting sphere of radius a (symbols).

A slight shift to larger kb values is noticeable in the coated sphere curve peaks with respect to the peaks of the perfect conductor.

At the still smaller coating refractive index of 1.2 shown in Fig. 3.18, the shift in the kb values of the peaks is much more noticeable. The magnitude of the first peak has decreased further until it has a smaller magnitude than that of the perfect conductor. The second peak now has a magnitude comparable to that of the perfect conductor.

These scattering results for a refractive index of 1.2 are plotted in terms of the core radius a in Fig. 3.19, instead of in terms of the total radius b as was done in previously considered curves. The positions of the peaks in the coated sphere scattering curve in this figure agree well with those of a perfectly conducting sphere with radius a . When the amplitude is normalized to the core radius a as it is in this figure, the coated sphere curve has a larger amplitude than the perfect conductor curve.

Similarly, curves for coatings having refractive indices 1.5, or greater, are plotted in terms of the core radius in Figs. 3.7, 3.9, 3.11, 3.13, and 3.15. The positions of the peaks in the coated sphere curves and in the curves for a perfectly conducting sphere of radius a , shown in these figures, are in poorer agreement than they were for a perfect conductor of radius b shown in the previous figures. In addition, the magnitude of the peaks in the coated sphere curves are still greater compared to the perfect conductor peaks than they were in the previous figures.

Hence, scattering results for coated spheres, analogous to those of Scharfman,²⁷ are obtained for the larger range of kb values including the first three peaks in the scattering curves: For large values of the coating refractive index, the oscillations in the scattering curve for the coated sphere are approximately in-phase with those in the scattering curve of a perfectly conducting sphere having a radius equal to the total radius of the coated sphere. For coating refractive indices less than approximately 1.6, the scattering is better described by a perfectly conducting sphere having a radius equal to the core radius. In both cases, the amplitudes of the oscillations in the scattering curves of the coated spheres are greater than those of the perfectly conducting spheres.

This qualitative rule remains valid with thinner coatings where similar, but much less pronounced effects are seen in the scattering plots. To illustrate the magnitude of the effect with thin coatings, scattering plots are presented for the radius ratios 1.004 and 1.0004 and for only two coating refractive indices of 1.75 and 4.0 at each coating thickness. These curves are given in Figs. 3.20 to 3.27. Since it is difficult to see differences in the curves at these thicknesses, the similarity to the previous case of $b/a = 1.04$ was verified from the computer printouts.

Including even a large amount of nondispersive absorption in the coating has very little effect on the qualitative behavior of the scattering curves. Absorption lines with dispersion are discussed in Section 4. To investigate the effect of constant absorption in the coating, the coating refractive index

$$m_2 = m'_2 - i0.1 \quad (3.38)$$

was used with $b/a = 1.0012$ and with the set of values $|m_2| = 1.2, 1.35, 1.5, 1.75, 2.5, 3.25,$ and 4.0 . The scattering curves are qualitatively the same as is expected for nonabsorbing coatings having the same magnitude refractive index. Notice that the imaginary part of the refractive index given in Eq. (3.38) implies a large absorption coefficient. With the constant imaginary part of 0.1, the absorption coefficient varies from 220 cm^{-1} at $kb = 1$ to 3000 cm^{-1} at $kb = 4$.

With coating thicknesses and refractive indices larger than those used in the above two-dimensional grid, the scattering begins to depart from the simple analogies with perfectly conducting spheres. The first evidence of anomalous results for high-index, thick coatings can be seen in Fig. 3.6 for $b/a = 1.04$ with $m_2 = 4.0$. In this figure the scattering at the third peak is as large as that at the second peak in contrast to the decreasing scattering amplitude with increasing kb of the perfectly conducting sphere. If the radius ratio is increased still further to $b/a = 1.4$ with $m_2 = 1.5$, the magnitude of the third peak becomes greater than both the first and second peaks. This case is plotted in Figs. 3.28 and 3.29 where the fourth peak is seen to have a still greater magnitude. Nevertheless, even with this very thick coating, there still is some qualitative agreement with a perfectly conducting sphere of radius b in the kb region of the first two peaks in Fig. 3.28.

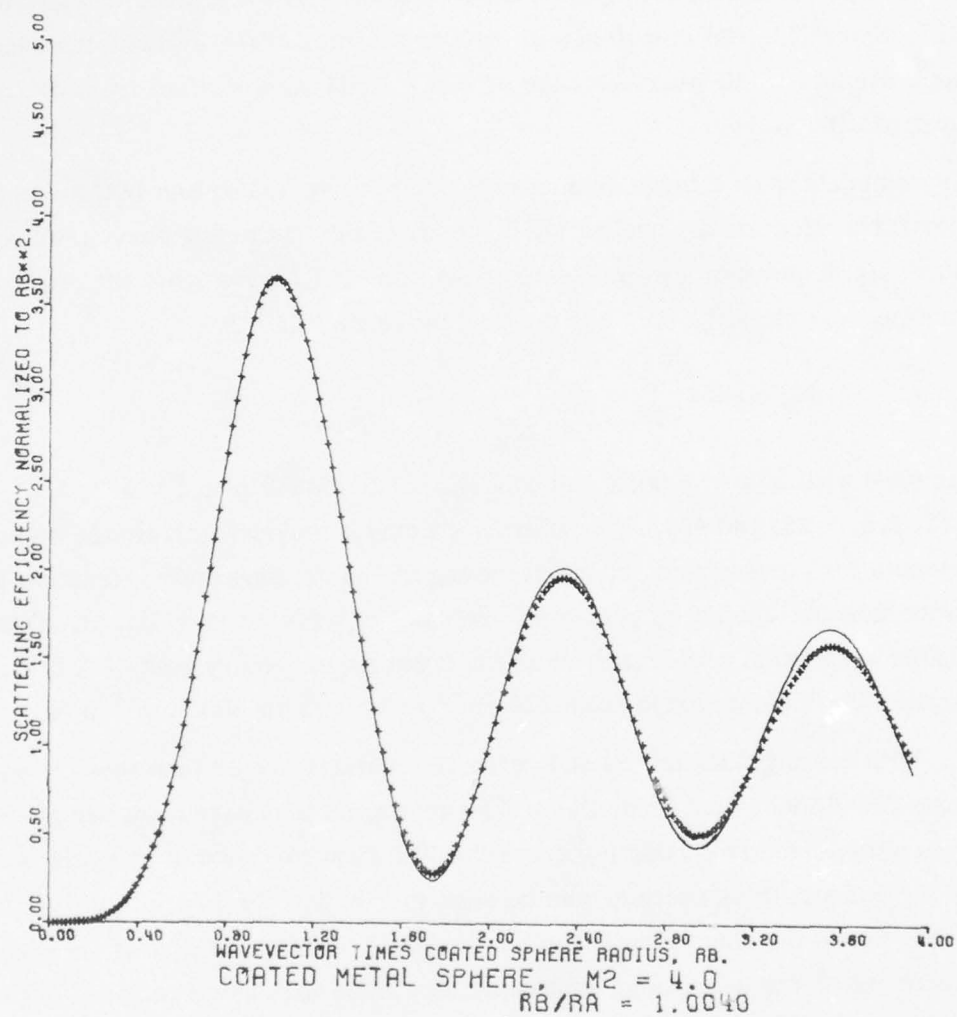


Fig. 3.20. Scattering from a coated metallic sphere normalized to the total cross-sectional area (solid curve) and scattering from a perfectly conducting sphere of radius b (symbols).

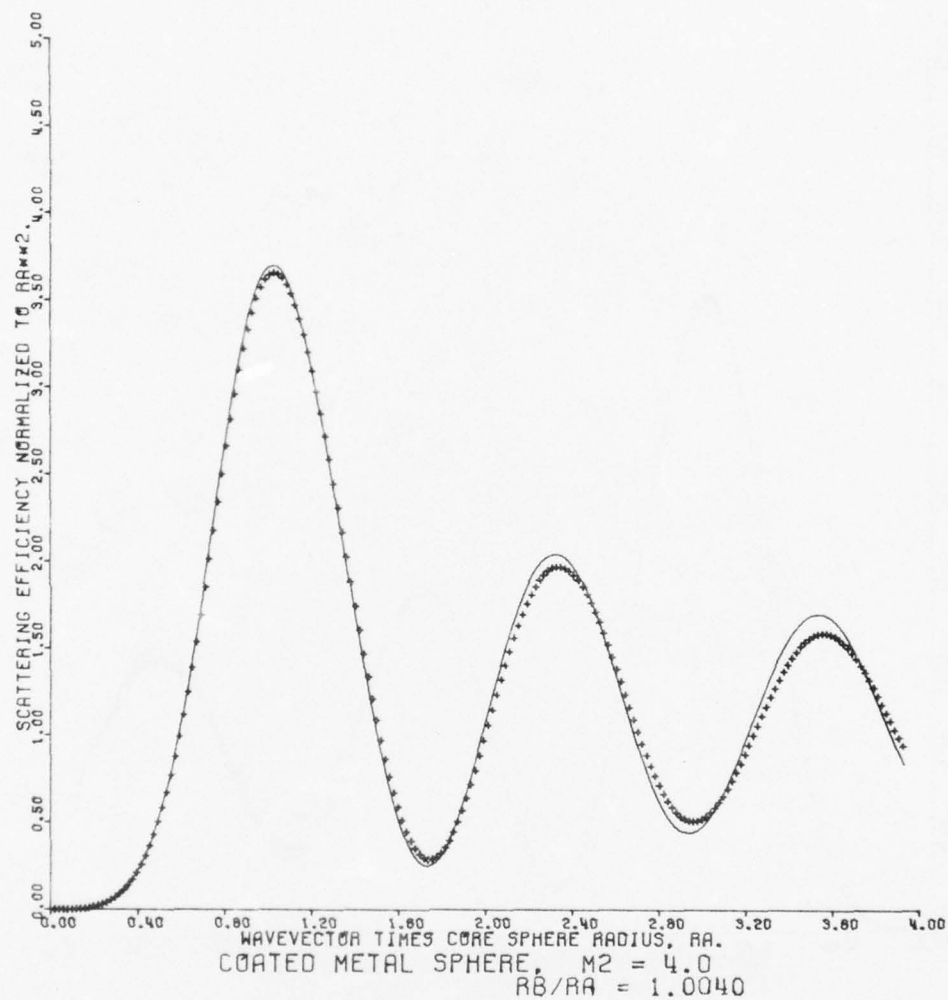


Fig. 3.21. Scattering from a coated metallic sphere normalized to the core cross-sectional area (solid curve) and scattering from a perfectly conducting sphere of radius a (symbols).

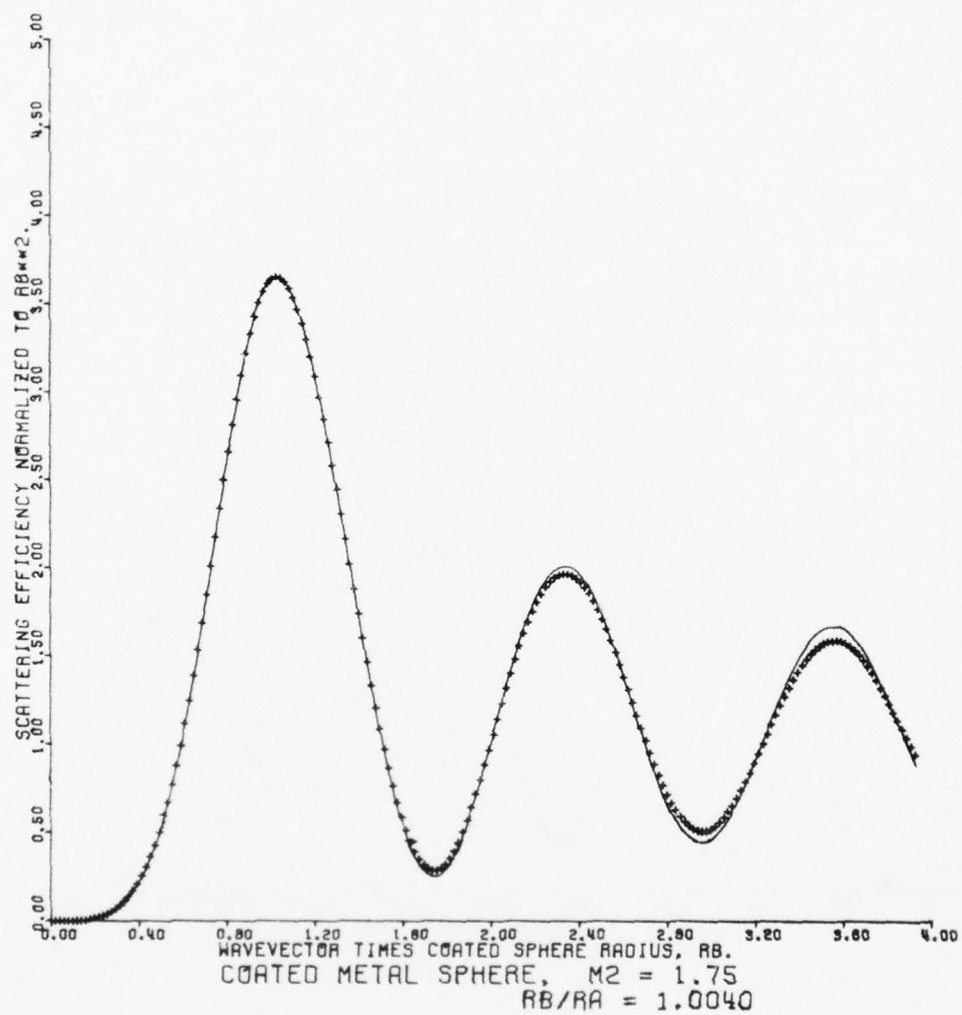


Fig. 3.22. Scattering from a coated metallic sphere normalized to the total cross-sectional area (solid curve) and scattering from a perfectly conducting sphere of radius b (symbols).

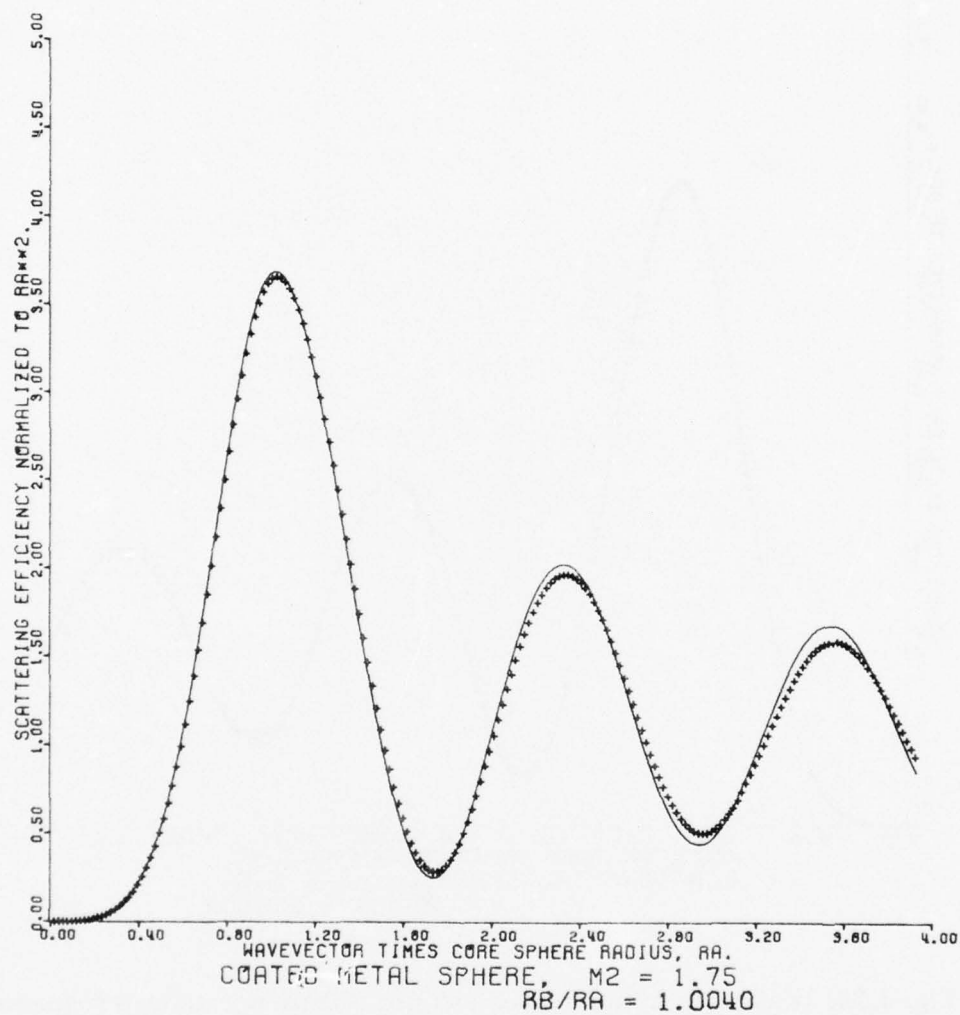


Fig. 3.23. Scattering from a coated metallic sphere normalized to the core cross-sectional area (solid curve) and scattering from a perfectly conducting sphere of radius a (symbols).

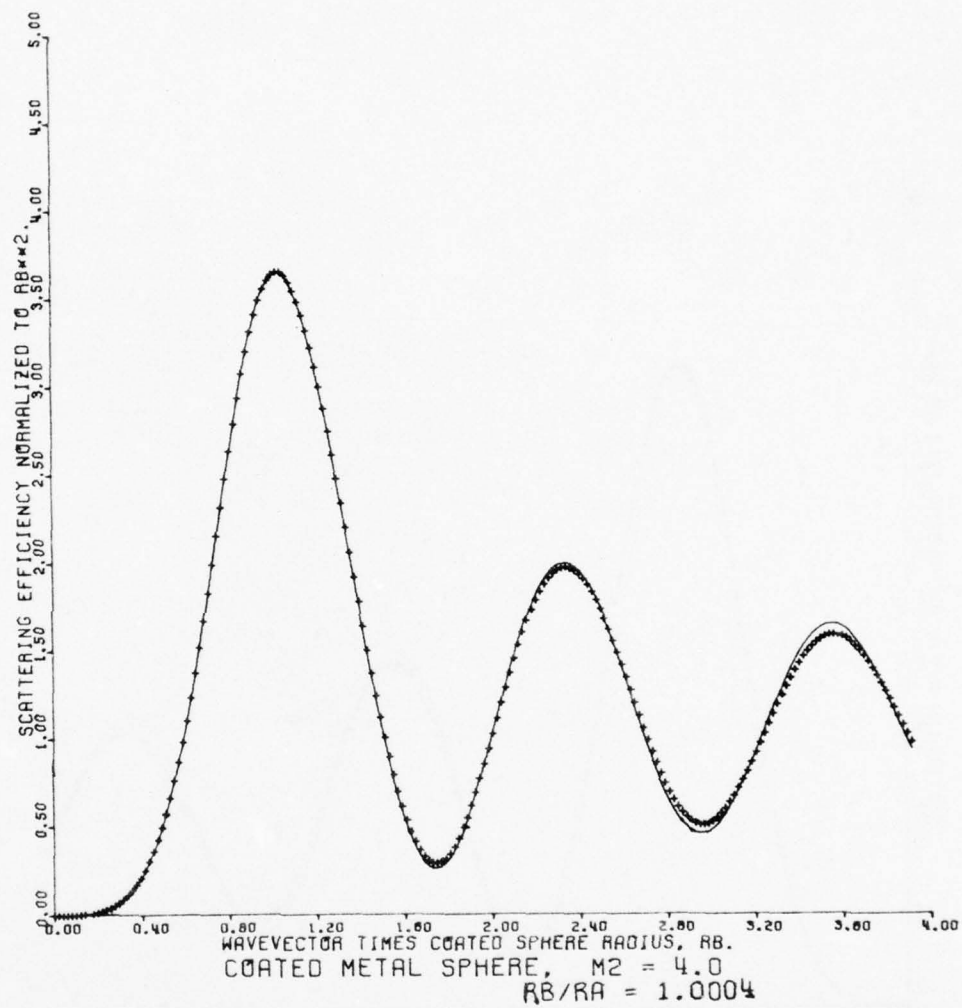


Fig. 3.24. Scattering from a coated metallic sphere normalized to the total cross-sectional area (solid curve) and scattering from a perfectly conducting sphere of radius b (symbols).

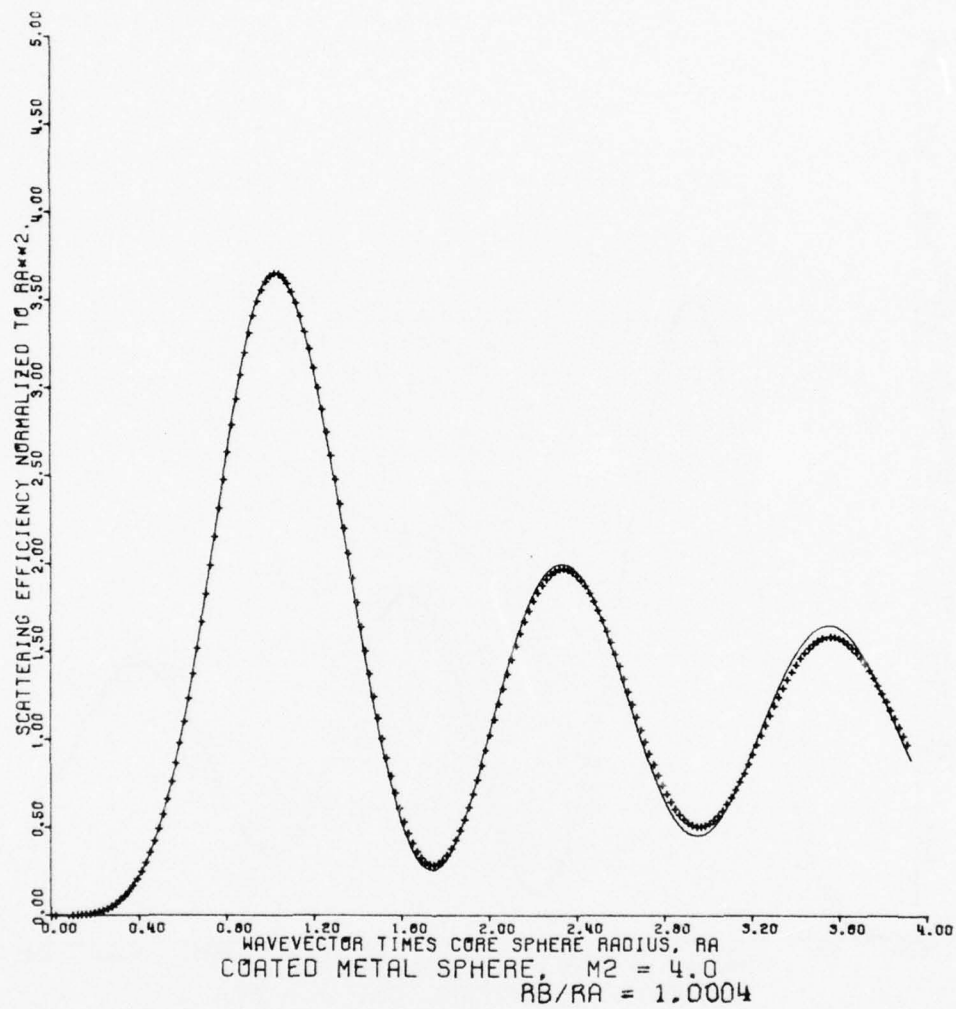


Fig. 3.25. Scattering from a coated metallic sphere normalized to the core cross-sectional area (solid curve) and scattering from a perfectly conducting sphere of radius a (symbols).

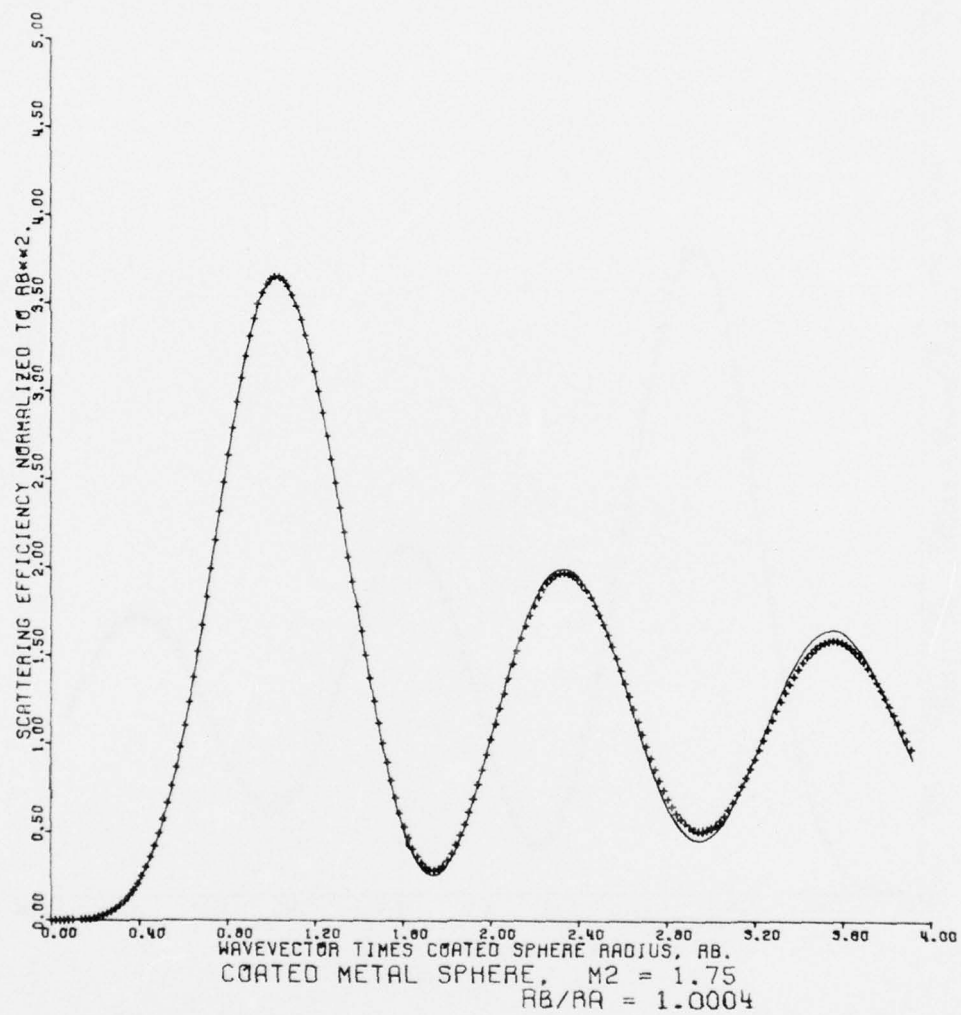


Fig. 3.26. Scattering from a coated metallic sphere normalized to the total cross-sectional area (solid curve) and scattering from a perfectly conducting sphere of radius b (symbols).

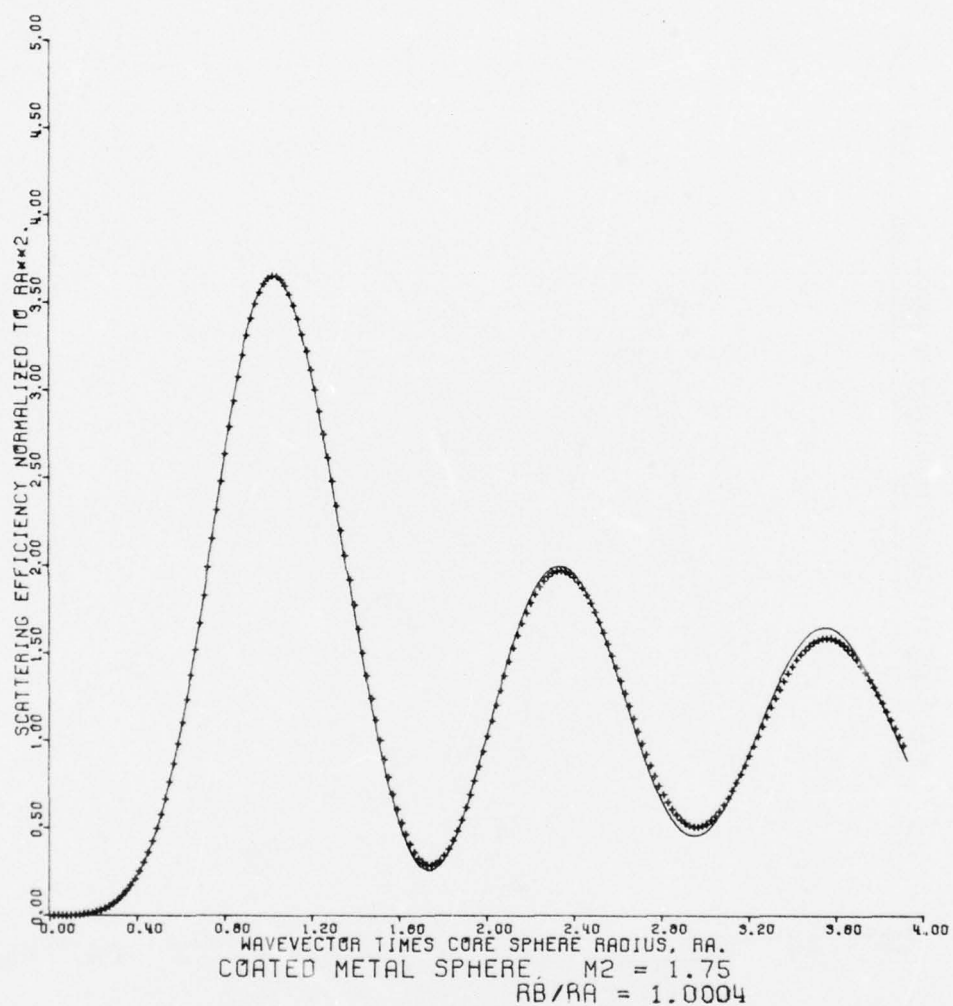


Fig. 3.27. Scattering from a coated metallic sphere normalized to the core cross-sectional area (solid curve) and scattering from a perfectly conducting sphere of radius a (symbols).

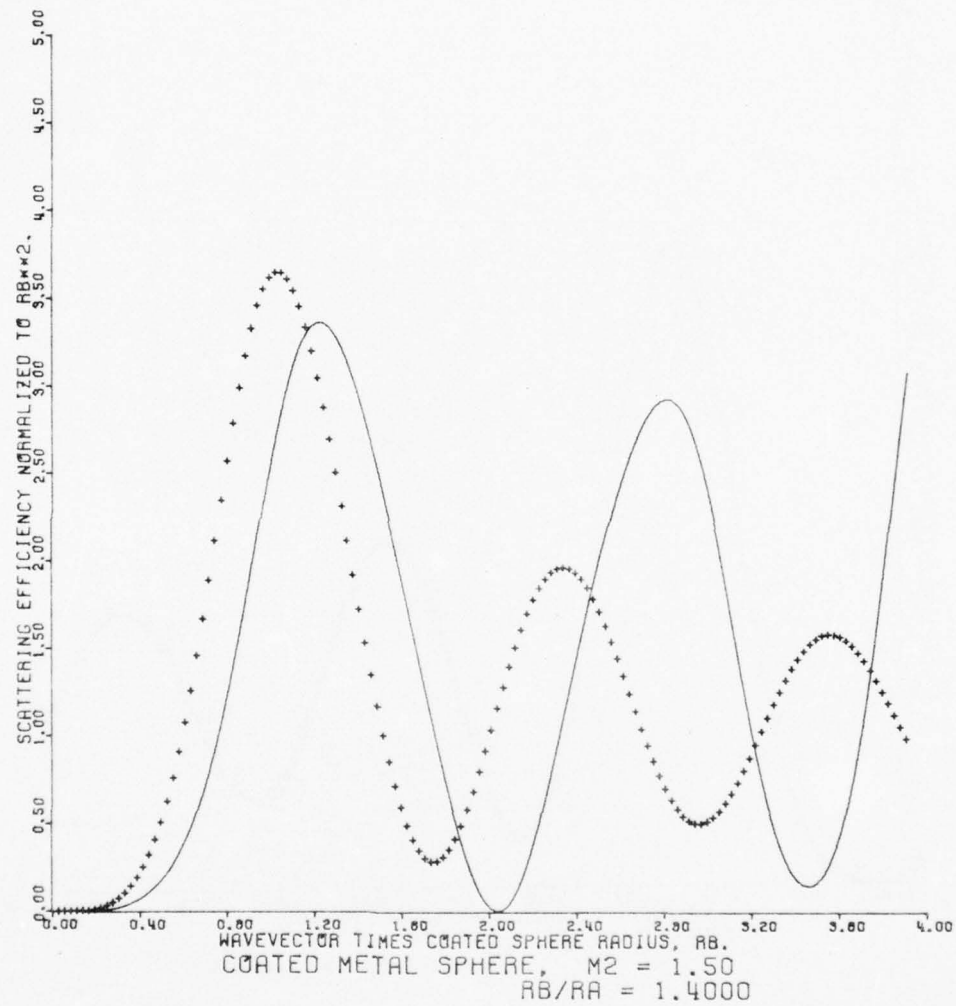


Fig. 3.28. Scattering from a coated metallic sphere normalized to the total cross-sectional area (solid curve) and scattering from a perfectly conducting sphere of radius b (symbols).

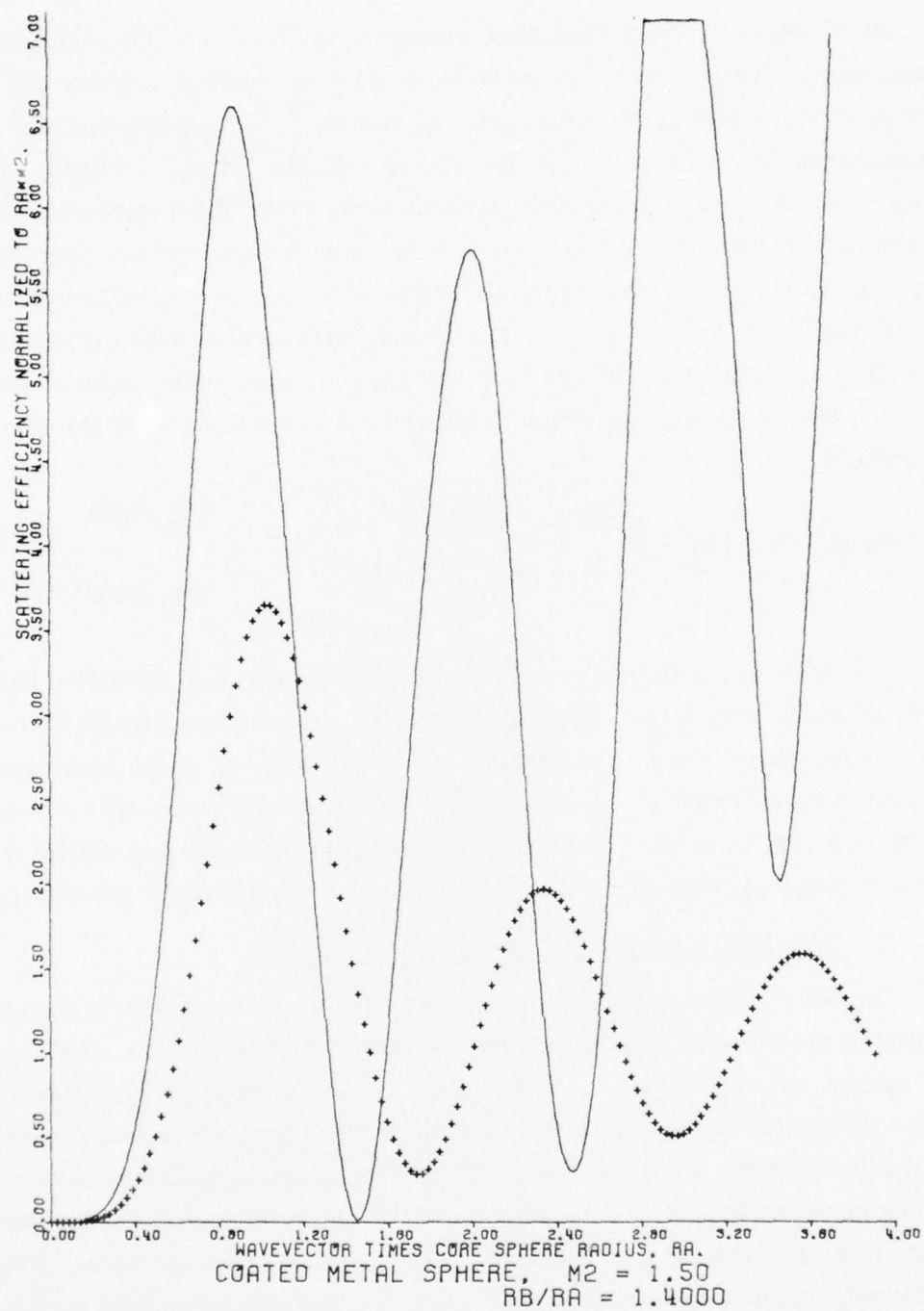


Fig. 3.29. Scattering from a coated metallic sphere normalized to the core cross-sectional area (solid curve) and scattering from a perfectly conducting sphere of radius a (symbols).

At kb values greater than those presented in Fig. 3.28, the scattering curve has a series of sharp spikes which become increasingly narrow and increase in magnitude as kb increases. Rheinstein²⁸ has investigated this phenomenon for perfectly conducting core spheres coated with a nondispersive dielectric. In his analysis the anomalously large value of the scattering at the resonance spikes is attributed to constructive interference in "creeping waves" trapped in the coating. For small kb values with thin coatings of low refractive index, the "creeping waves" are considerably attenuated as they propagate around the circumference of the sphere and, consequently, have little effect on the scattering. The creeping waves begin to influence the scattering when the waveguide conditions

$$kb \left(\frac{b}{a} - 1 \right) \left(m^2 - 1 \right)^{1/2} \cong \begin{cases} (n-1)\pi & \text{TE}_n \text{ mode} \\ \left(n - \frac{1}{2} \right) \pi & \text{TM}_n \text{ mode} \end{cases} \quad (3.39)$$

are met, where n is an integer. If the coating thickness and refractive index are held constant, once kb has increased above the value required by (3.39) to turn on a mode, the creeping wave analysis predicts that the Q of the resonances increases with increasing kb . This results in increasingly sharp spikes in the scattering with increasing kb . Parameters for this behavior are outside the present range of interest and reference is made to Rheinstein²⁸ for details.

3. Quantitative results for nondispersive coatings.

Consider scattering plots similar to those presented in terms of the core radius in the previous section, where now scattering from the uncoated, metallic sphere, rather than a perfectly conducting sphere, is given by + symbols. Since the metallic sphere is well approximated by a perfectly conducting sphere of the same radius, the curves are not repeated. The qualitative behavior remains the same as in the previous section with the scattering curve for the coated sphere having larger maxima and lower minima than the curve for the uncoated, metallic sphere. It is desired to describe the differences between the curves quantitatively. To do this, one complete oscillation in the curve is considered, say between the first two peaks. This region from $ka = 1.021$ to 2.337 is divided into N points and the root-mean-square percent deviation (RMS%) is calculated:

$$\text{RMS \%} = 100 \left[\frac{1}{N} \sum_{n=1}^N \left(\frac{G_n^c - G_n^m}{G_n^m} \right)^2 \right]^{1/2}, \quad (3.40)$$

where G_n^c and G_n^m are the values of the scattering for the coated and uncoated metallic spheres at the n th point, respectively. Use of the RMS% deviation avoids difficulties with the signs of the deviations when the curves cross.

Using the two-dimensional grid of coating refractive indices and thicknesses given in the previous section, curves for the RMS% deviation are given in Fig. 3.30 for each thickness as a function of the coating refractive index. In the limit $m_2 = 1.0$, all of the curves must go to zero deviation since this limit corresponds to a vacuum coating. For m_2 greater than approximately two, the curves become nearly flat. However, the values in the flat region are not the asymptotic values for an infinite refractive index, i.e., the limit where the coated sphere becomes a perfectly conducting sphere of radius b . The dashed lines at the right-hand side of the figure give the asymptotic values for the various thicknesses. The dotted line at 3.7% is the asymptotic limit of a coating having an infinite refractive index and zero thickness, i.e., the limiting deviation between a metallic sphere and a perfectly conducting sphere of the same radius. Notice that with $b/a = 1.04$ and $m_2 = 4.0$, the RMS% deviation is greater than its asymptotic value in contrast to the curves for thinner coatings which are below their asymptotic limits. This difference is a result of the abnormally large cross sections generated by the waveguide mechanism in spheres with thick coatings. A similar enhancement may also occur for $|m_2| \gg 4$ in the curves for thinner coatings.

For thin coatings with radius ratios less than about 1.004, the RMS% deviation is within one percent of being linear in the coating thickness at a fixed coating refractive index. This linear relationship is lost at larger thicknesses. For example, linear extrapolation to the $b/a = 1.04$ curve from the $b/a = 1.004$ and 1.0004 curves predicts values that are three percent too low at $m_2 = 1.2$ and nineteen percent too low at $m_2 = 4.0$.

The curve with $b/a = 1.0012$ in Fig. 3.30 presents the RMS% deviation of nondispersive, absorbing coatings having complex refractive indices given by Eq. (3.38). Even with the large absorption coefficients of these coatings, the

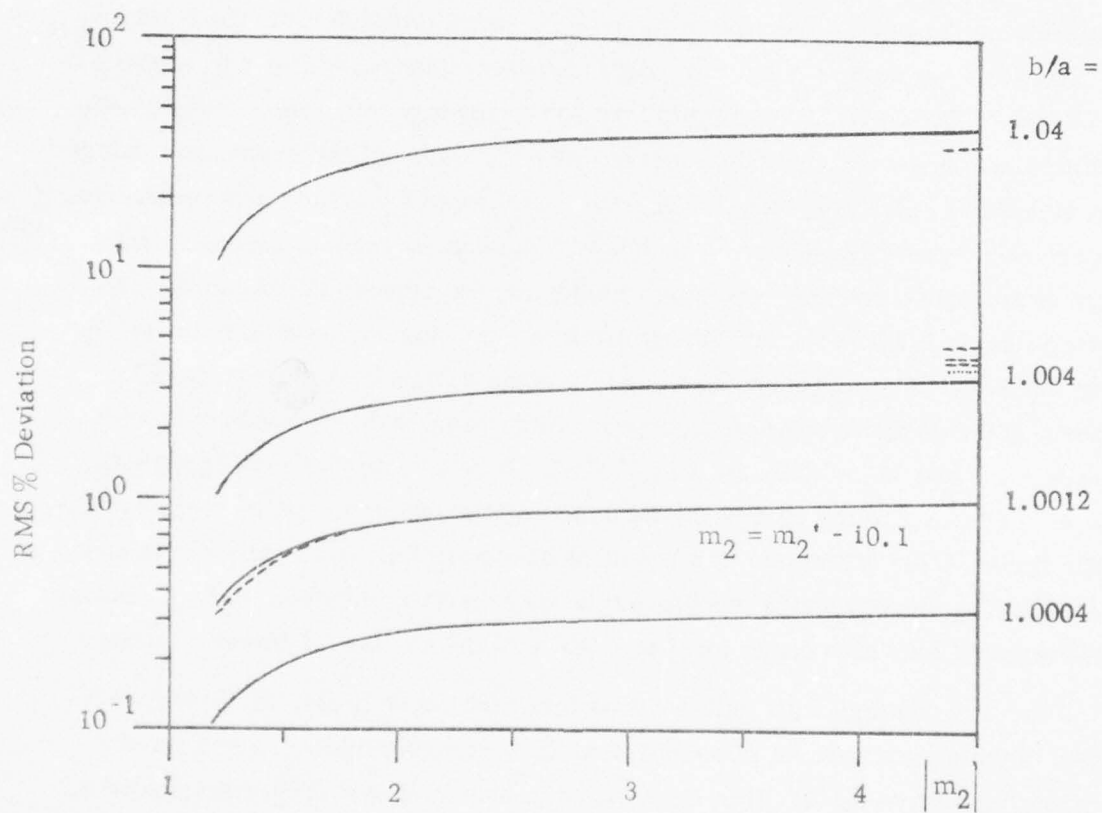


Fig. 3.30. Root-mean-square percent deviation of the scattering of a coated metallic sphere from that of the uncoated sphere as a function of the coating refractive index for various coating thicknesses.

RMS % deviation agrees very well with values for nonabsorbing coatings having the same magnitude refractive index, except for small differences at small magnitude indices. The dashed curve gives values for a real refractive index obtained by extrapolation from the $b/a = 1.004$ and $b/a = 1.0004$ curves.

In Fig. 3.31, the data of Fig. 3.30 have been cast into level contours of the RMS % deviations as a function of the coating thickness, $b-a$, and the magnitude of the refractive index. As the coating refractive index approaches unity, i.e., a vacuum coating, the curves of constant deviation approach infinity indicating that an arbitrarily thick vacuum coating produces zero deviation. The determination of asymptotic values of the error contours in the limit of an infinite refractive index would require another set of computer calculations and hence has not been evaluated. This limit corresponds to differences in the scattering between metallic spheres of radius a and perfectly conducting spheres of radius b .

4. Dispersive coatings.

Optical constants of actual solid materials have absorption bands and dispersion, rather than the constant absorbing and nonabsorbing refractive indices considered in the previous sections. These absorption bands can be conveniently represented by a distribution of Lorentzian absorption lines, the use of which guarantees the correct dispersive behavior as required by the Kramers-Kronig relations. The Reststrahl absorption bands of many ionic solids can be crudely approximated by a single absorption line of large linewidth. A better model in this case is to allow the relaxation frequency of the Lorentzian line to be a function of the radiation frequency. With electronic transitions and with lattice absorption in nonpolar solids, the absorption bands consist of a superposition of many absorption lines of narrow linewidth.

Hence as a model calculation applicable to many materials by superposition, the effect of a single Lorentzian absorption line on the scattering is considered. The dielectric constant for a Lorentzian line as a function of frequency is

$$\epsilon(\omega) = \epsilon_{\infty} + \frac{(\epsilon_0 - \epsilon_{\infty})\omega_0^2}{(\omega_0^2 - \omega^2) + i\omega\Gamma}, \quad (3.41)$$

AD-A035 478

XONICS INC VAN NUYS CALIF
RESEARCH ON CRYSTAL CHEMISTRY STUDIES.(U)
NOV 76 M SPARKS, C J DUTHLER

F/G 7/4

UNCLASSIFIED

RADC-TR-76-343

F19628-75-C-0123
NL

2 OF 2

AD
A035478



END

DATE
FILMED
3-77

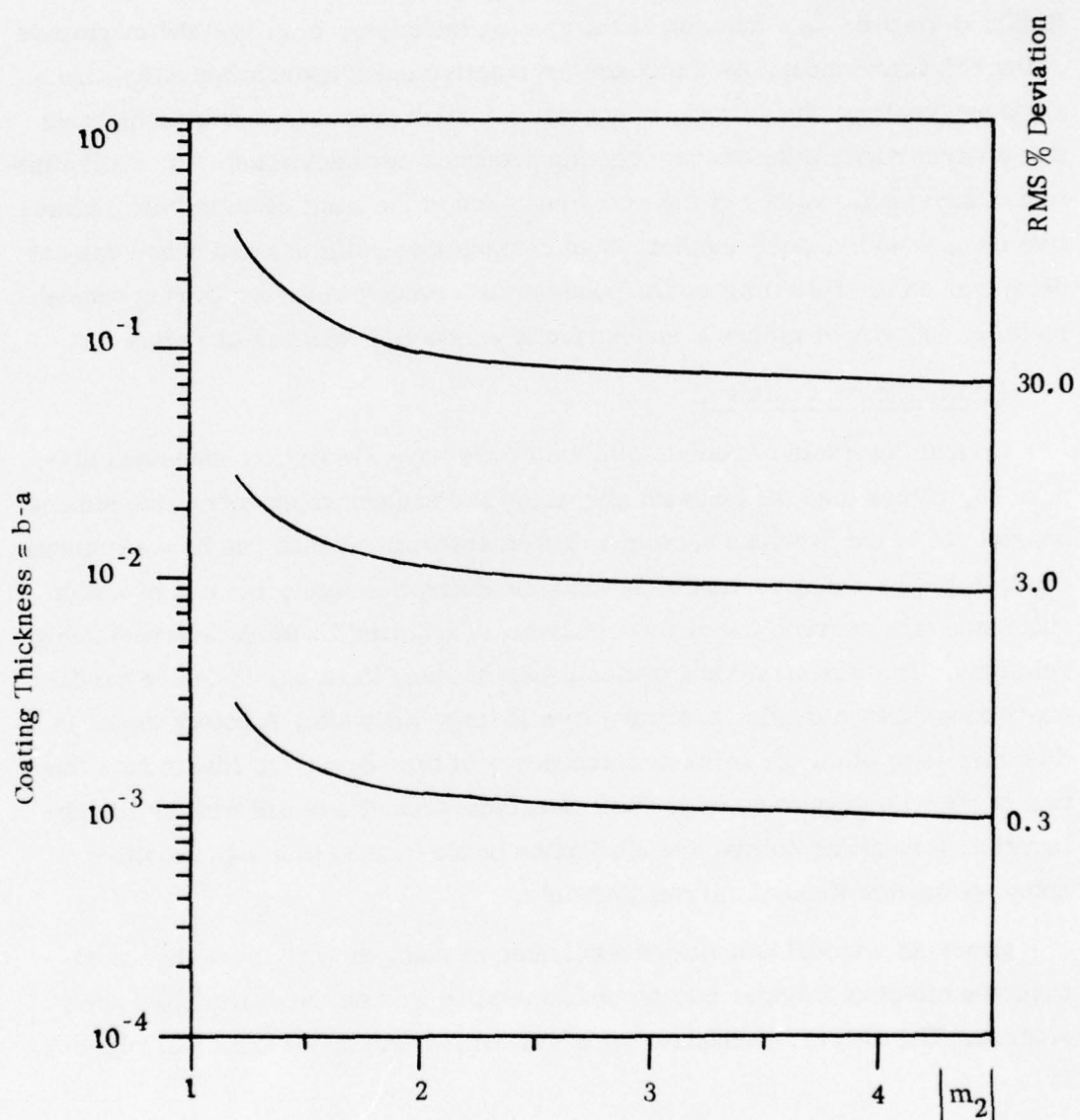


Fig. 3.31. Contours of constant root-mean-square percent deviation of the scattering of a coated metallic sphere from that of the uncoated sphere as a function of the coating thickness and coating refractive index.

where ϵ_0 and ϵ_∞ are the static and high frequency dielectric constants, respectively, ω_0 is the resonant absorption frequency, and Γ is the relaxation frequency. For a constant relaxation frequency, Γ is equal to the full width at half maximum of the absorption line. The scattering from an actual metal-oxide coating and from a dispersive dielectric sphere is considered later in this section.

The effect of the linewidth on the scattering was first investigated using three moderately thick coatings all with radius ratio 1.04 and with a resonant absorption frequency given by the ka value of 1.428. The constants in Eq. (3.41) were adjusted for the three linewidths of 50 cm^{-1} , 20 cm^{-1} , and 10 cm^{-1} used, so that the refractive index in the visible was 1.5 and the absorption strength at the line center was 10^4 cm^{-1} . The real parts (solid curve) and imaginary parts (dashed curve) of these dielectric constants are plotted in Figs. 3.32(a), 3.33(a), and 3.34(a). The abscissas in these figures are given in units of kb for the radius ratio $b/a = 1.04$. In these units, the line centers are located at the kb value of 1.485. In parts (b) of Figs. 3.32-3.34, the scattering in the vicinity of the absorption line is plotted as a solid curve for the coated metallic sphere. For reference, scattering from a perfectly conducting sphere of radius b is shown as a dashed curve on the same axes.

With the 50 cm^{-1} linewidth absorption shown in Fig. 3.32, the scattering curve for the coated sphere has a gentle S-shaped deviation from a smooth curve in the vicinity of the absorption. With the narrower 20 cm^{-1} linewidth shown in Fig. 3.33, the scattering curve has a narrow, flat plateau at the absorption line frequency. With the still narrower linewidth of 10 cm^{-1} shown in Fig. 3.34, there is a small magnitude dip in the absorption curve having approximately the same linewidth as the absorption line.

To investigate the effect of the absorption-line frequency on the scattering, five frequencies are considered at positions evenly spaced in wavelength between the first maximum and the first minimum on the scattering curve. As above, the scattering is calculated for the three linewidths (10 cm^{-1} , 20 cm^{-1} , and 50 cm^{-1}) at each frequency keeping the radius ratio constant at 1.04 and the absorption coefficient at the line center constant at 10^4 cm^{-1} . These scattering results are plotted versus ka in Figs. 3.35-3.49.

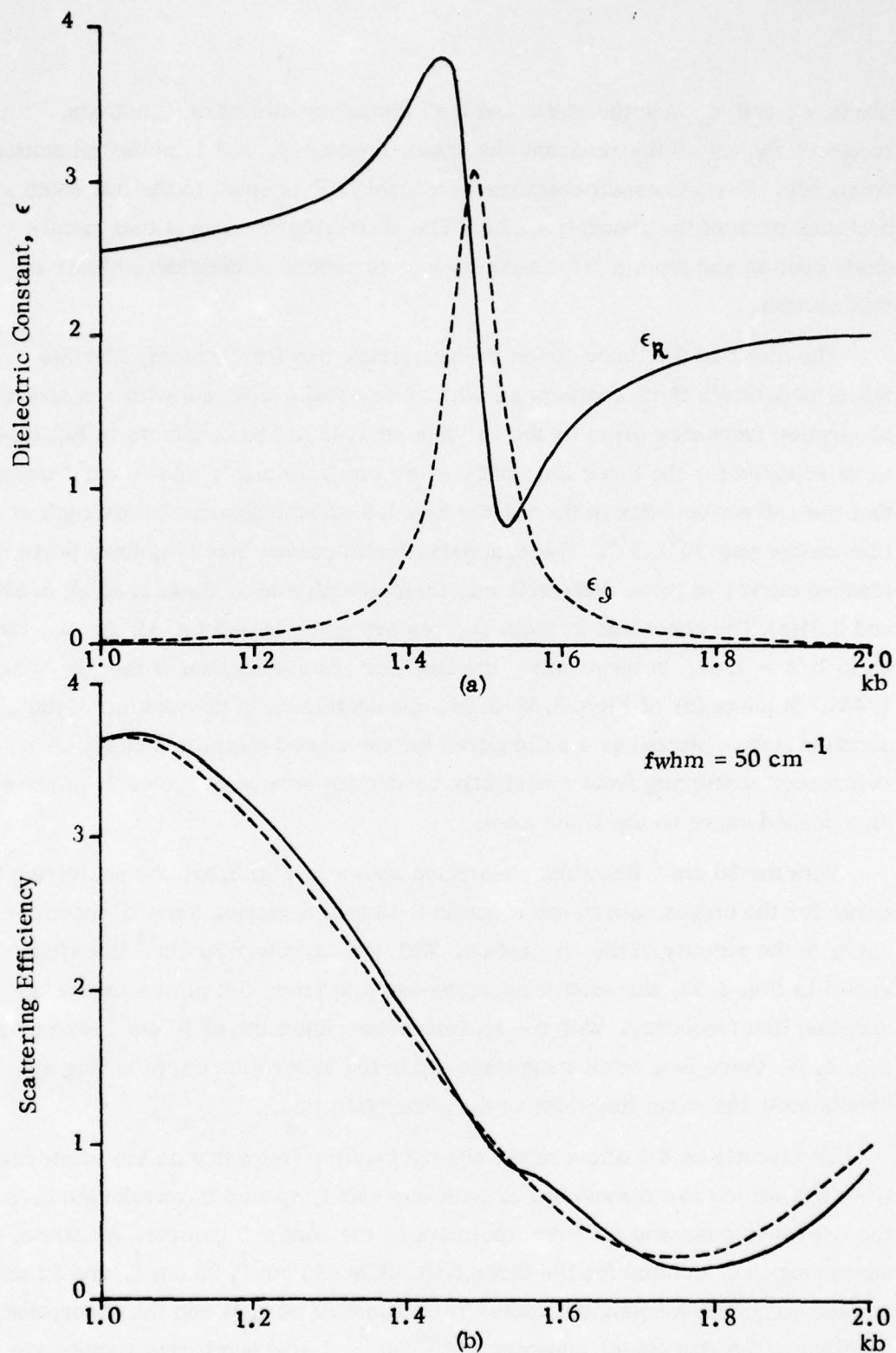


Fig. 3.32. Real part ϵ_R and imaginary part ϵ_g of the dielectric constant of a coating having a Lorentzian absorption line with a full width at half maximum of 50 cm^{-1} (a). Scattering from a coated metallic sphere in the vicinity of the absorption line (b).

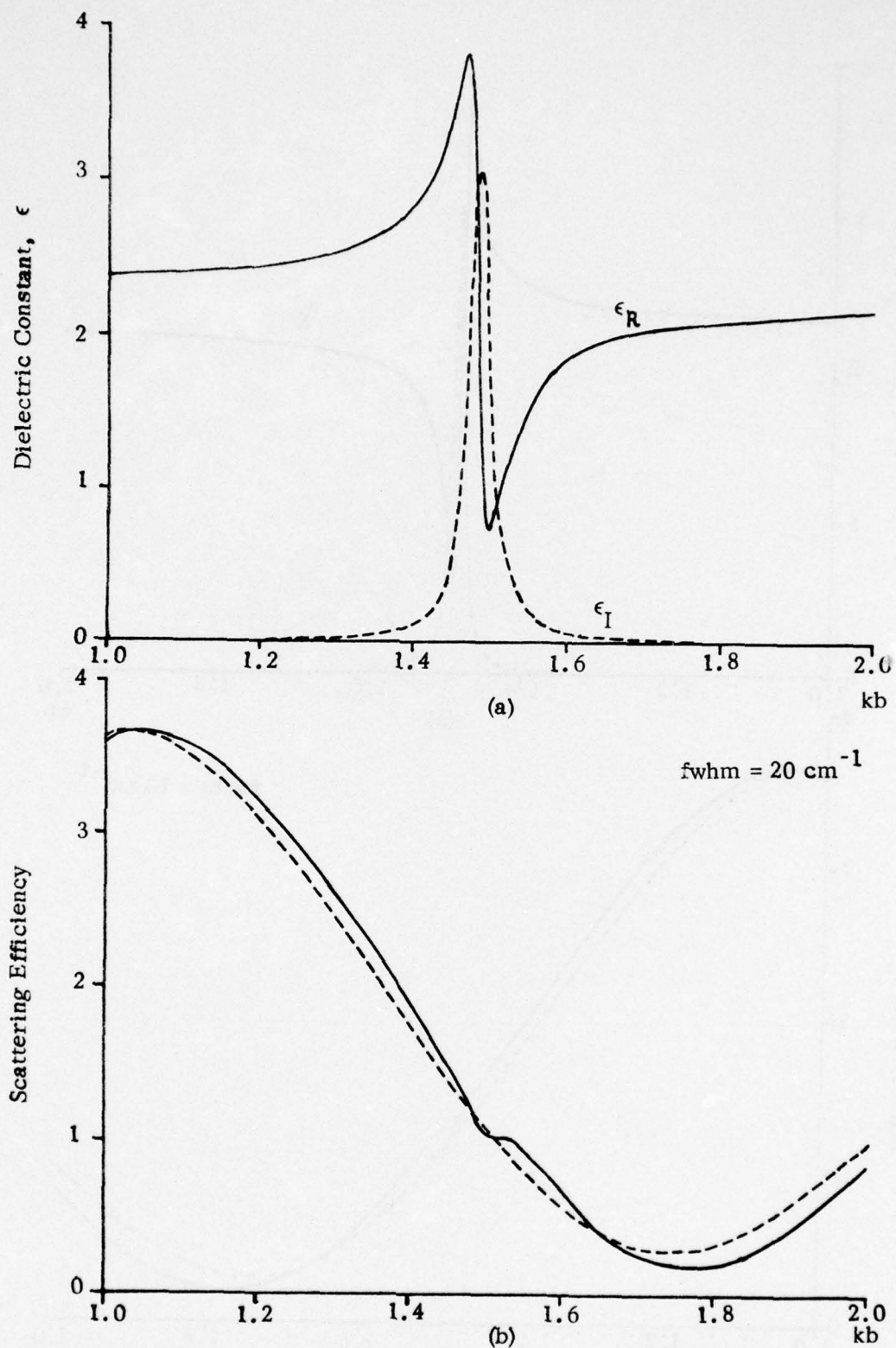


Fig. 3.33. Real part ϵ_R and imaginary part ϵ_I of the dielectric constant of a coating having a Lorentzian absorption line with a full width at half maximum of 20 cm⁻¹ (a). Scattering from a coated metallic sphere in the vicinity of the absorption line (b).

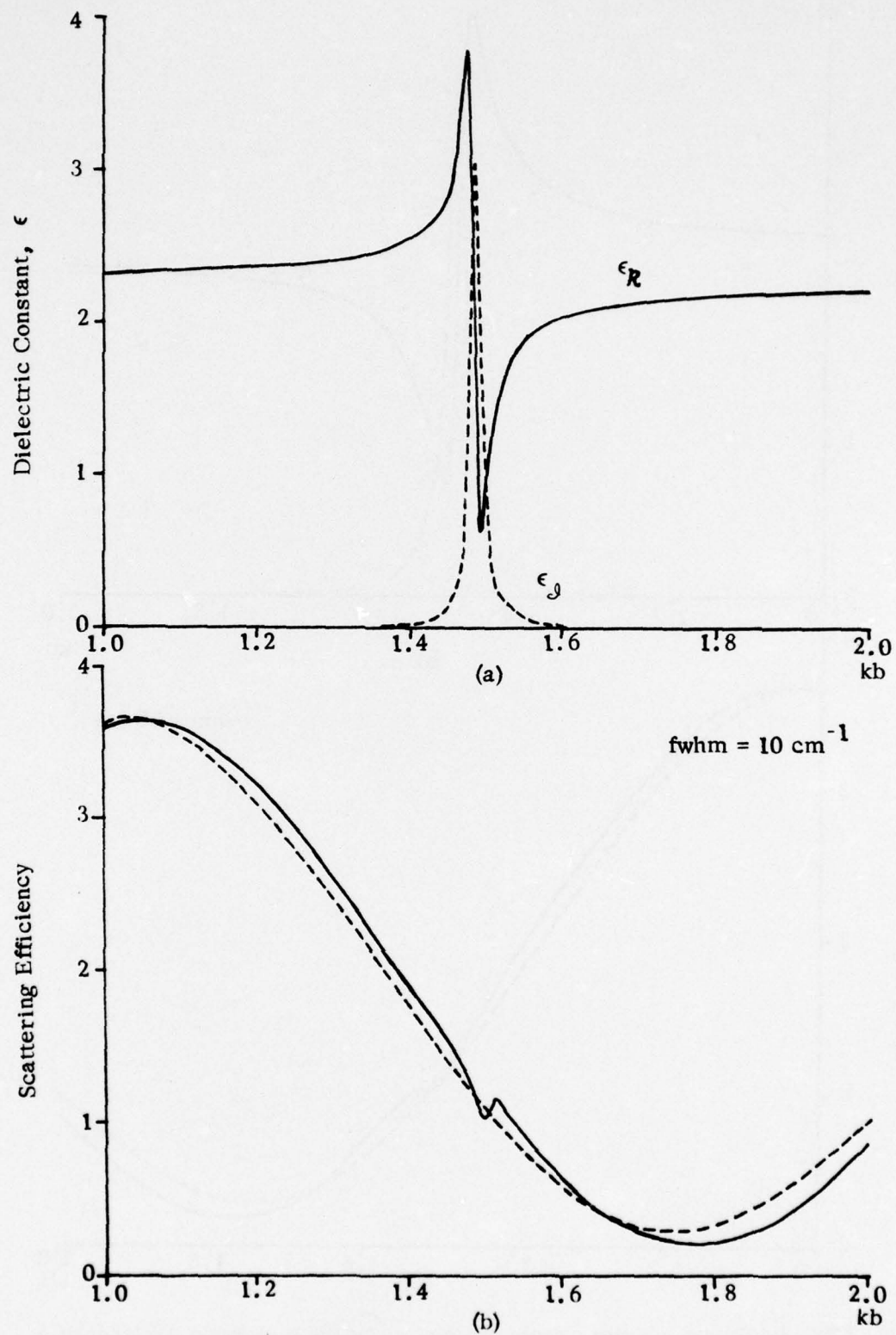


Fig. 3.34. Real part ϵ_R and imaginary part ϵ_I of the dielectric constant of a coating having a Lorentzian absorption line with a full width at half maximum of 10 cm^{-1} (a). Scattering from a coated metallic sphere in the vicinity of the absorption line (b).

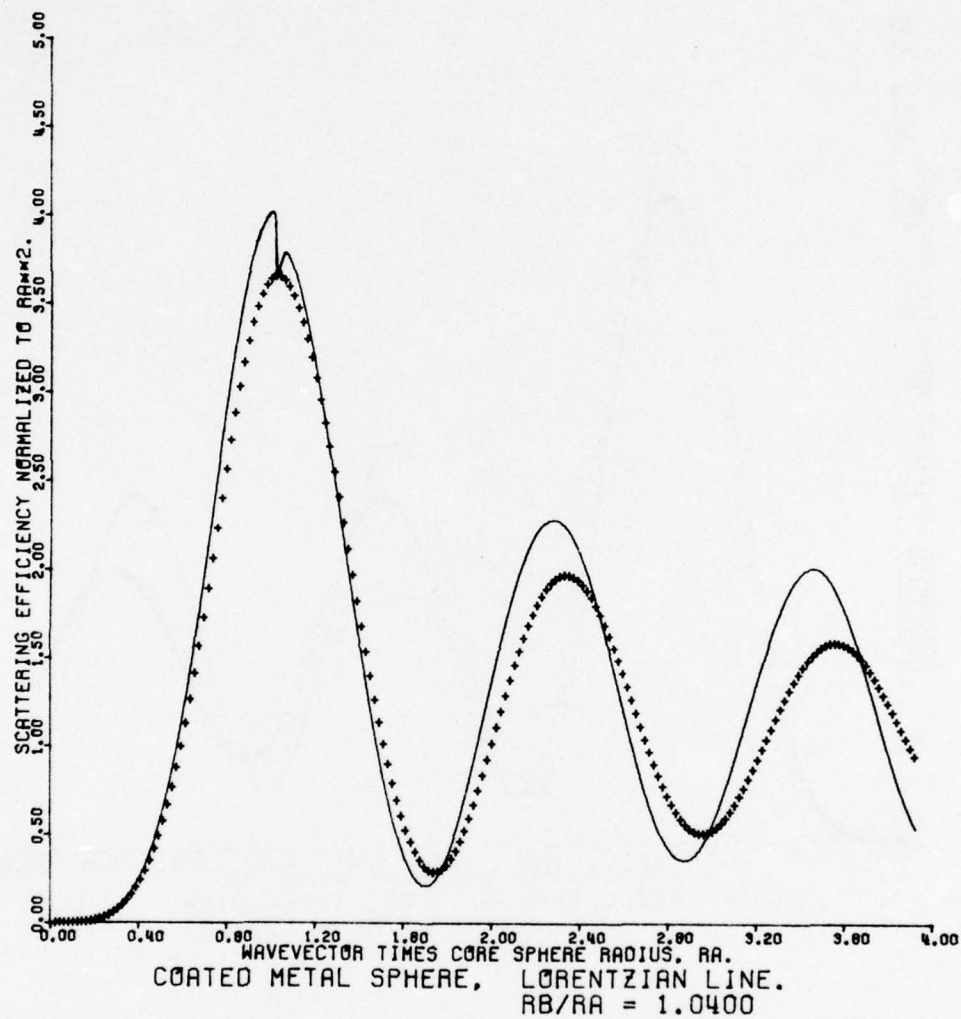


Fig. 3.35. Scattering from a coated metallic sphere having a 10 cm^{-1} fwhm absorption line at $ka = 1.01$ (solid curve). Results are normalized to the core cross-sectional area and compared to a perfectly conducting sphere of radius b (symbols).

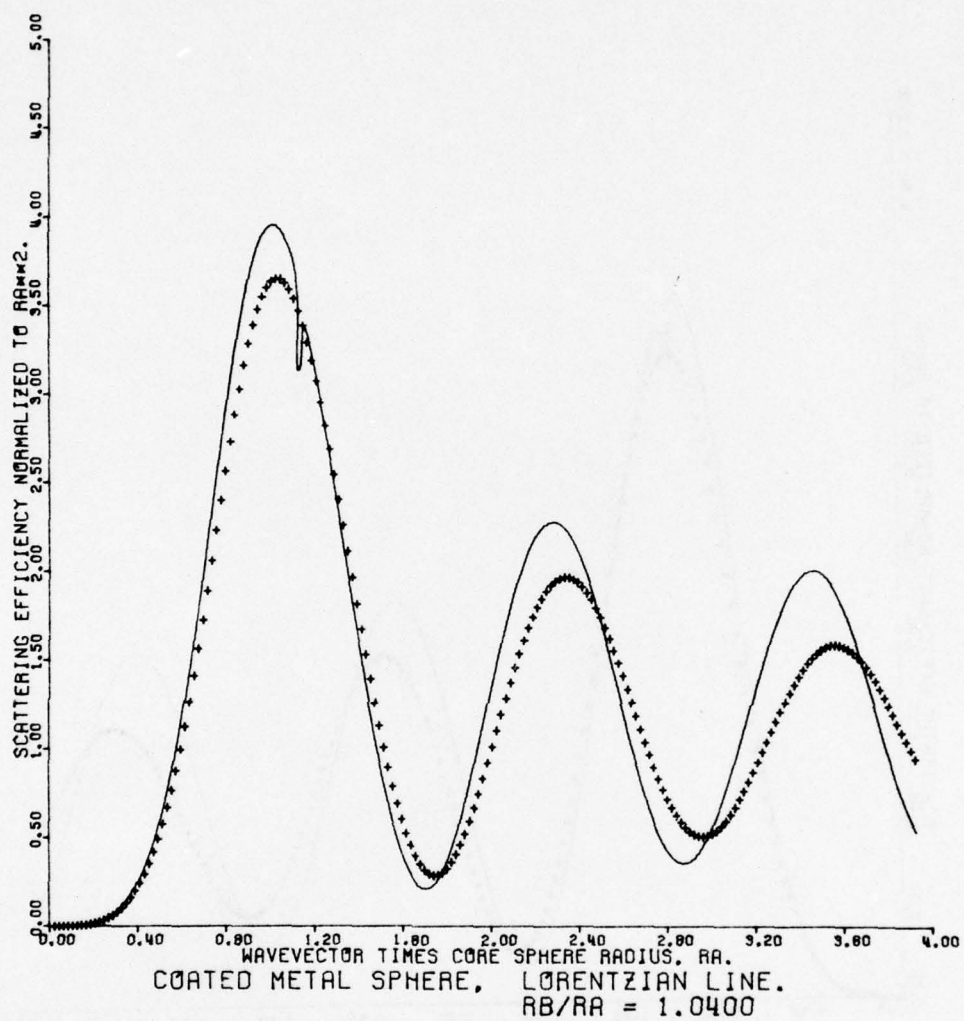


Fig. 3.36. Scattering from a coated metallic sphere having a 10 cm^{-1} fwhm absorption line at $ka = 1.12$ (solid curve). Results are normalized to the core cross-sectional area and compared to a perfectly conducting sphere of radius b (symbols).

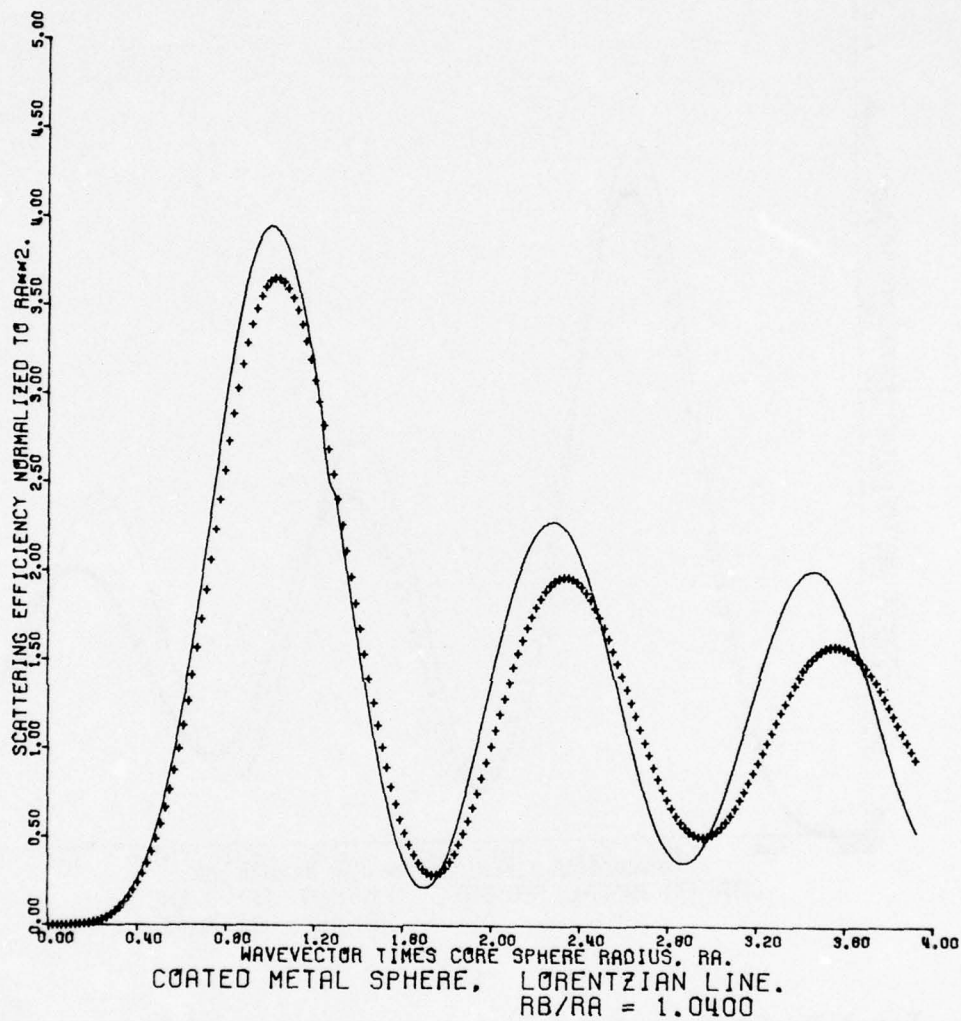


Fig. 3.37. Scattering from a coated metallic sphere having a 10 cm^{-1} fwhm absorption line at $ka = 1.26$ (solid curve). Results are normalized to the core cross-sectional area and compared to a perfectly conducting sphere of radius b (symbols).

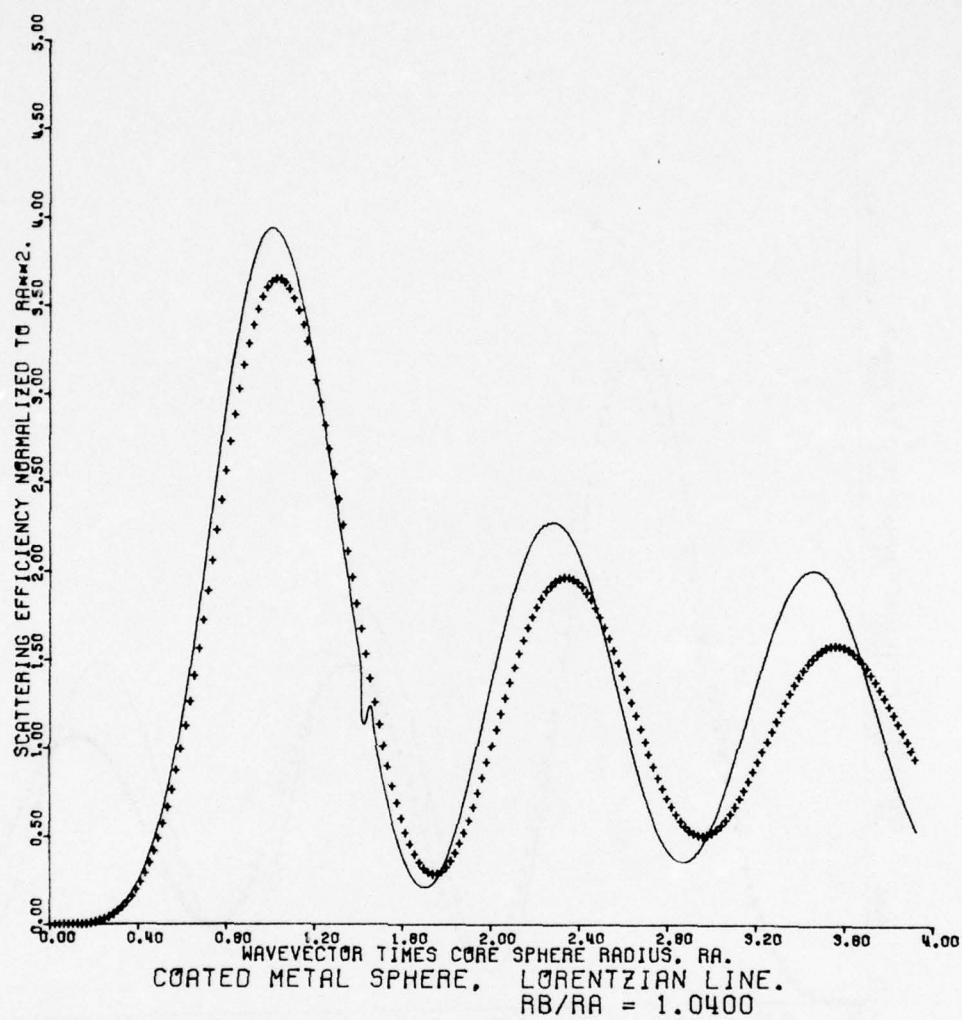


Fig. 3.38. Scattering from a coated metallic sphere having a 10 cm^{-1} fwhm absorption line at $ka = 1.43$ (solid curve). Results are normalized to the core cross-sectional area and compared to a perfectly conducting sphere of radius b (symbols).

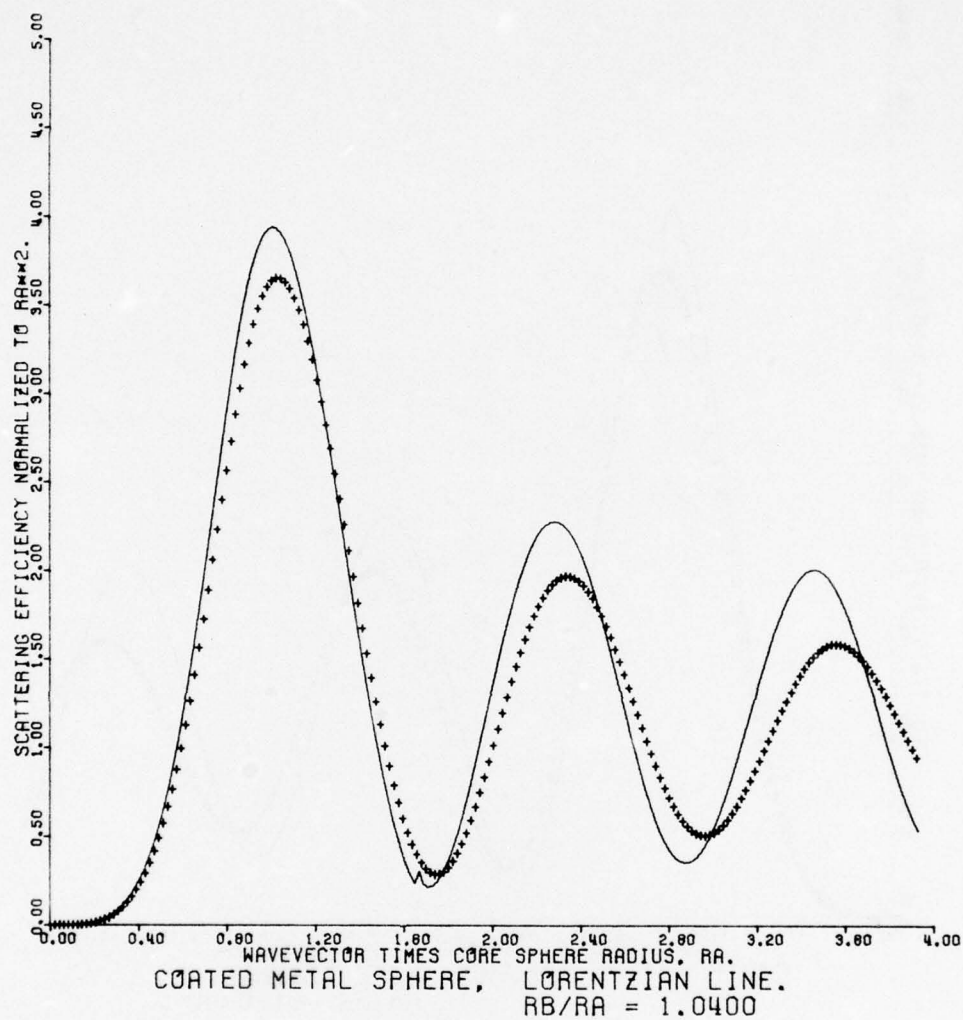


Fig. 3.39. Scattering from a coated metallic sphere having a 10 cm^{-1} fwhm absorption line at $ka = 1.65$ (solid curve). Results are normalized to the core cross-sectional area and compared to a perfectly conducting sphere of radius b (symbols).

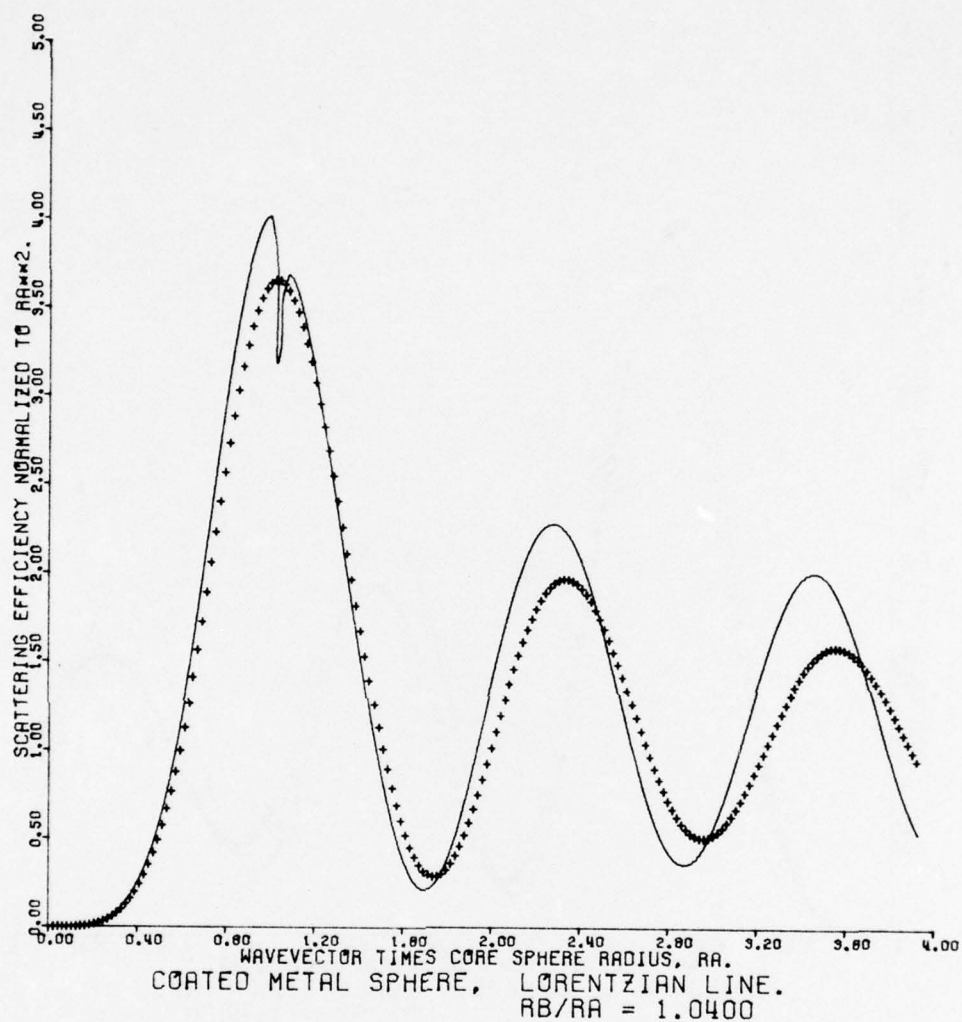


Fig. 3.40. Scattering from a coated metallic sphere having a 20 cm^{-1} fwhm absorption line at $ka = 1.01$ (solid curve). Results are normalized to the core cross-sectional area and compared to a perfectly conducting sphere of radius b (symbols).

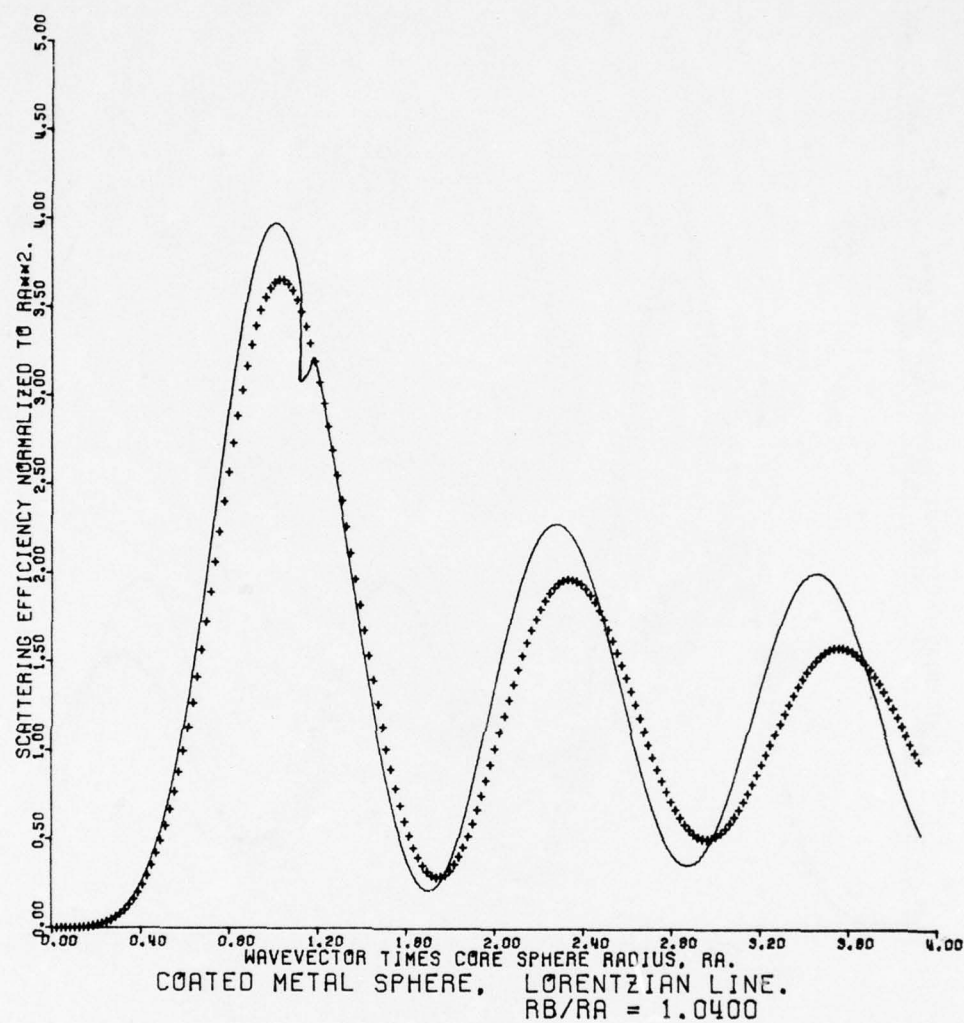


Fig. 3.41. Scattering from a coated metallic sphere having a 20 cm^{-1} fwhm absorption line at $ka = 1.12$ (solid curve). Results are normalized to the core cross-sectional area and compared to a perfectly conducting sphere of radius b (symbols).

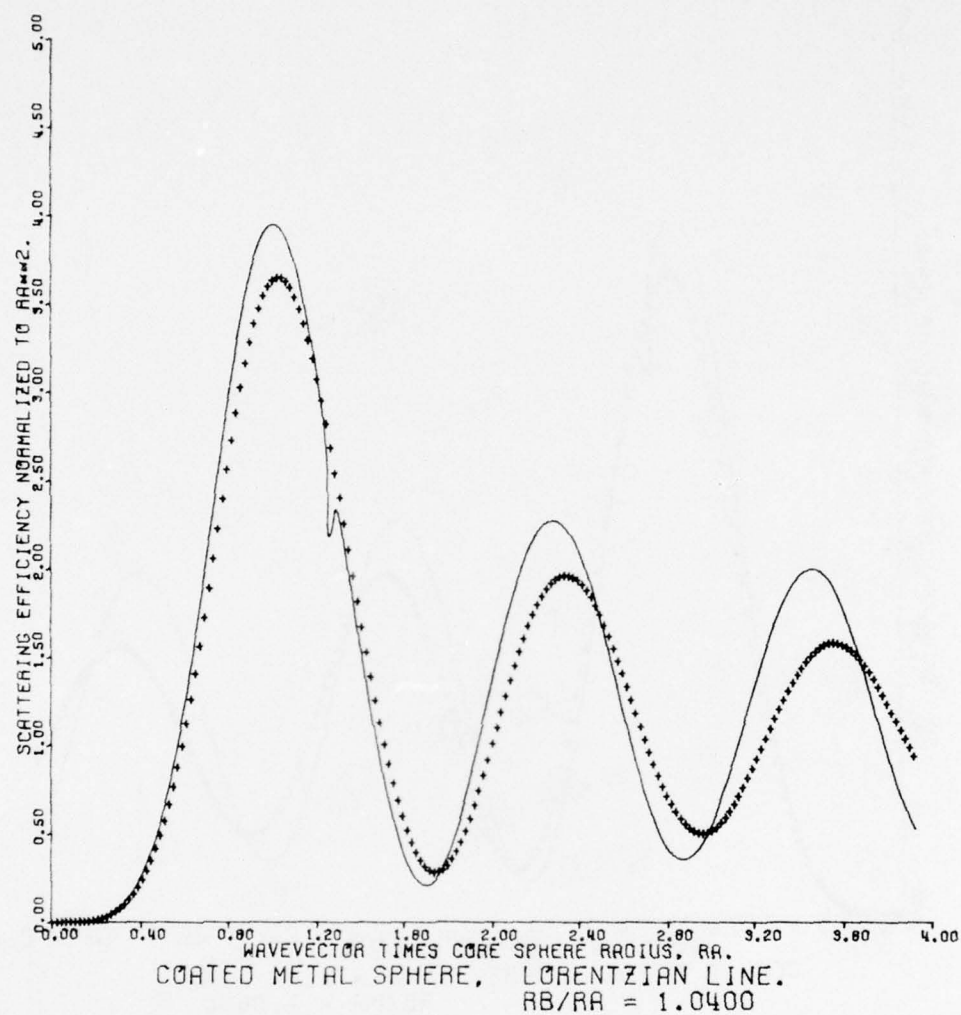


Fig. 3.42. Scattering from a coated metallic sphere having a 20 cm^{-1} fwhm absorption line at $ka = 1.26$ (solid curve). Results are normalized to the core cross-sectional area and compared to a perfectly conducting sphere of radius b (symbols).

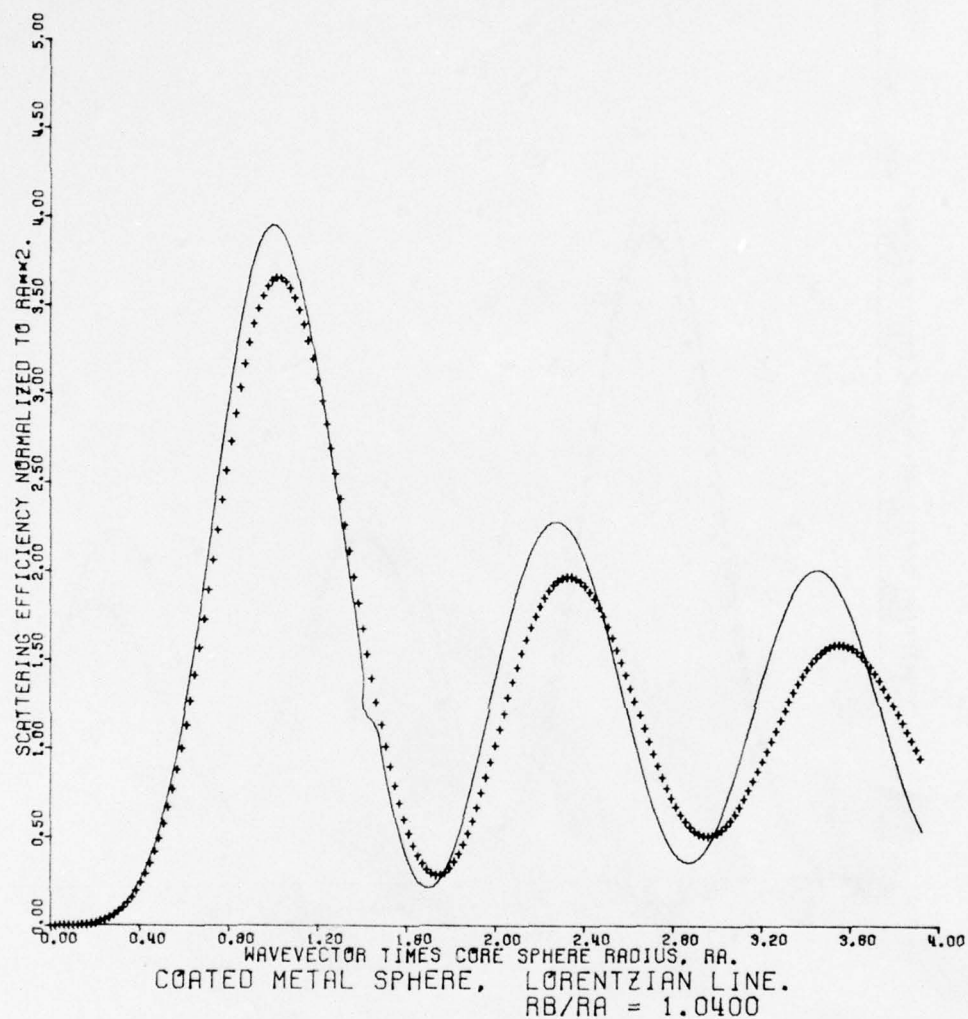


Fig. 3.43. Scattering from a coated metallic sphere having a 20 cm^{-1} fwhm absorption line at $ka = 1.43$ (solid curve). Results are normalized to the core cross-sectional area and compared to a perfectly conducting sphere of radius b (symbols).

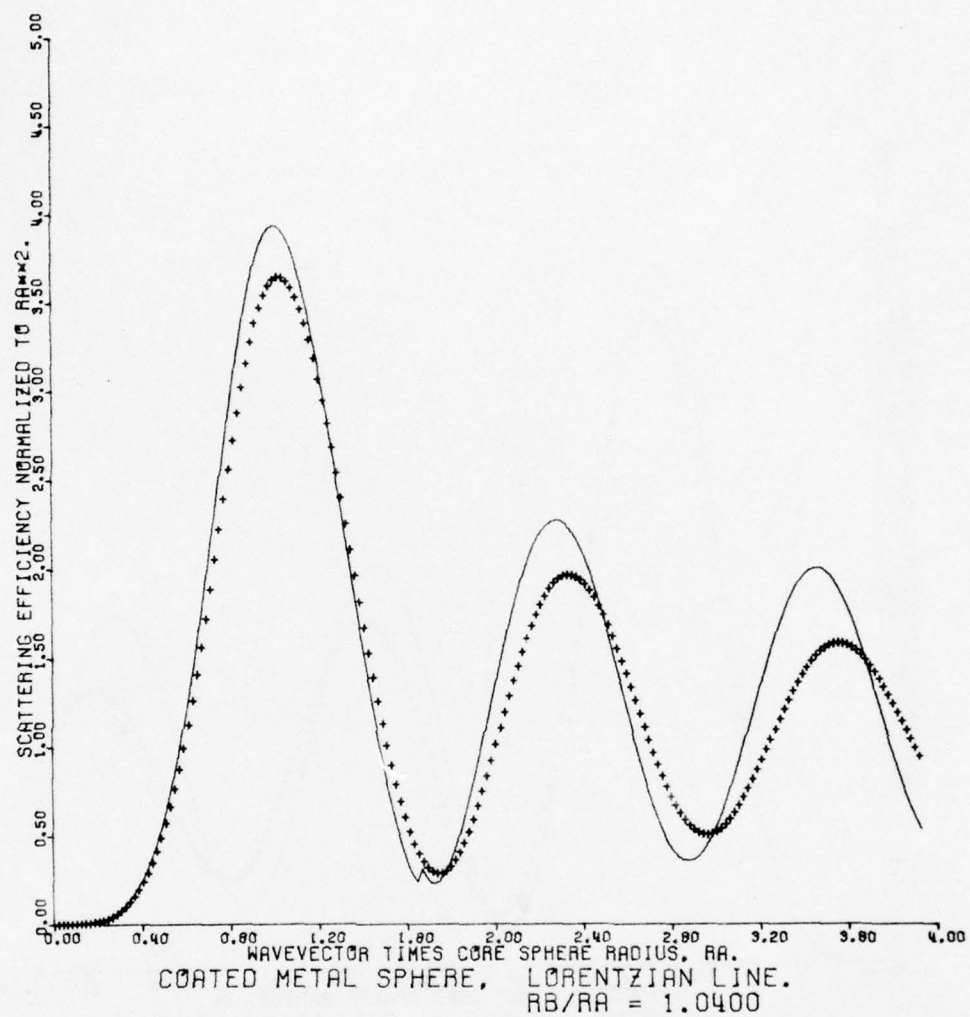


Fig. 3.44. Scattering from a coated metallic sphere having a 20 cm^{-1} fwhm absorption line at $ka = 1.65$ (solid curve). Results are normalized to the core cross-sectional area and compared to a perfectly conducting sphere of radius b (symbols).

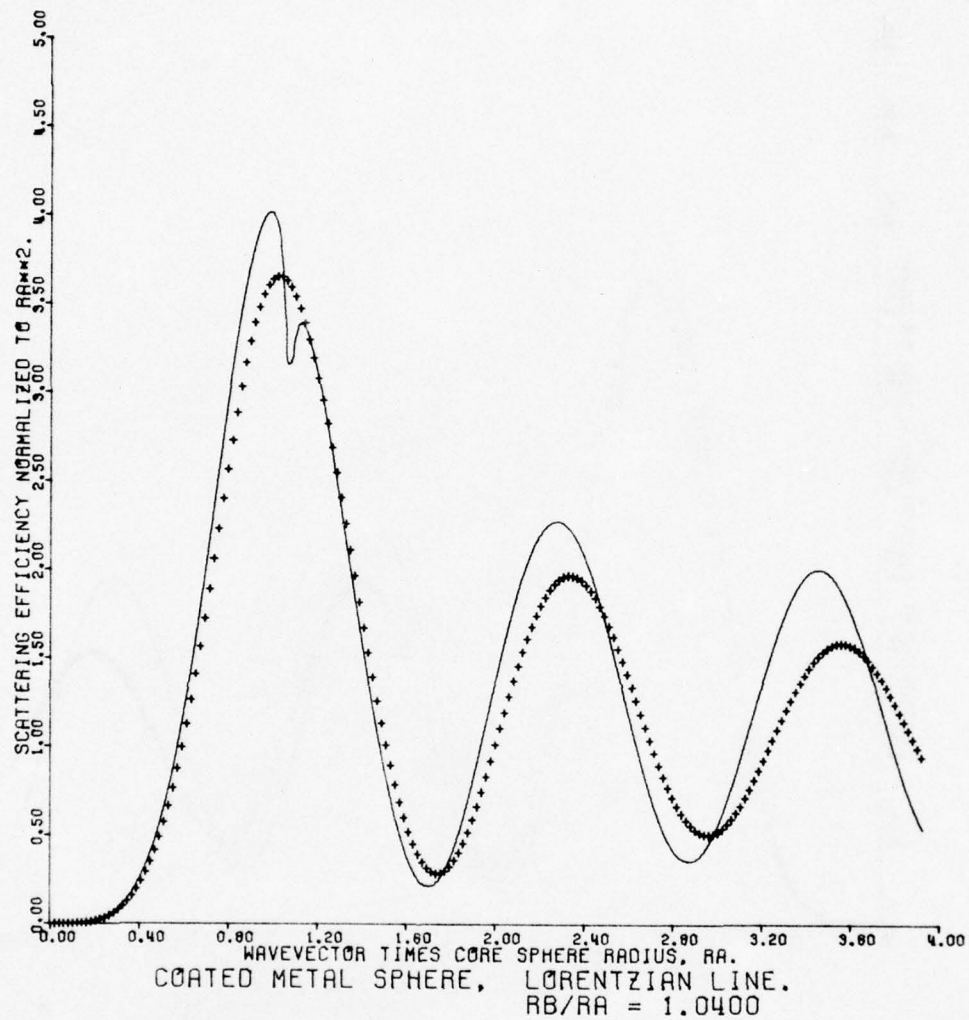


Fig. 3.45. Scattering from a coated metallic sphere having a 50 cm^{-1} fwhm absorption line at $ka = 1.01$ (solid curve). Results are normalized to the core cross-sectional area and compared to a perfectly conducting sphere of radius b (symbols).

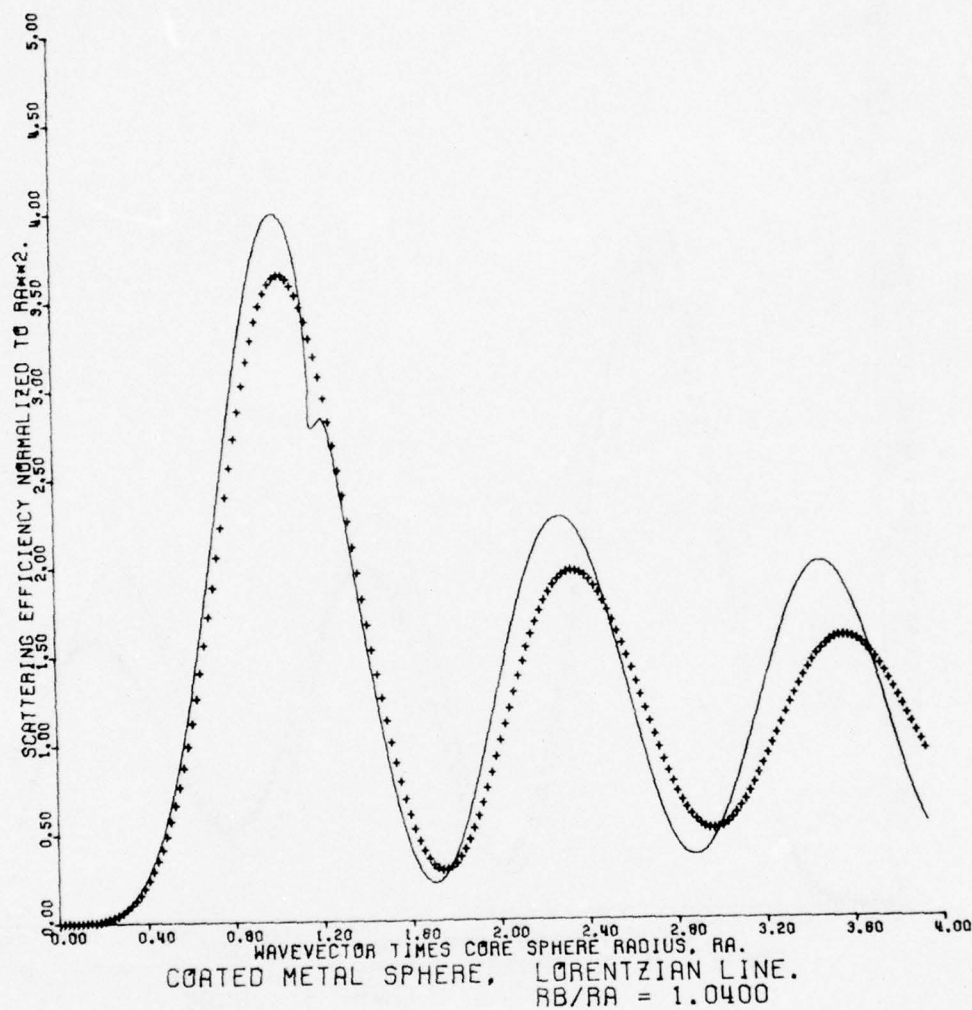


Fig. 3.46. Scattering from a coated metallic sphere having a 50 cm^{-1} fwhm absorption line at $ka = 1.12$ (solid curve). Results are normalized to the core cross-sectional area and compared to a perfectly conducting sphere of radius b (symbols).

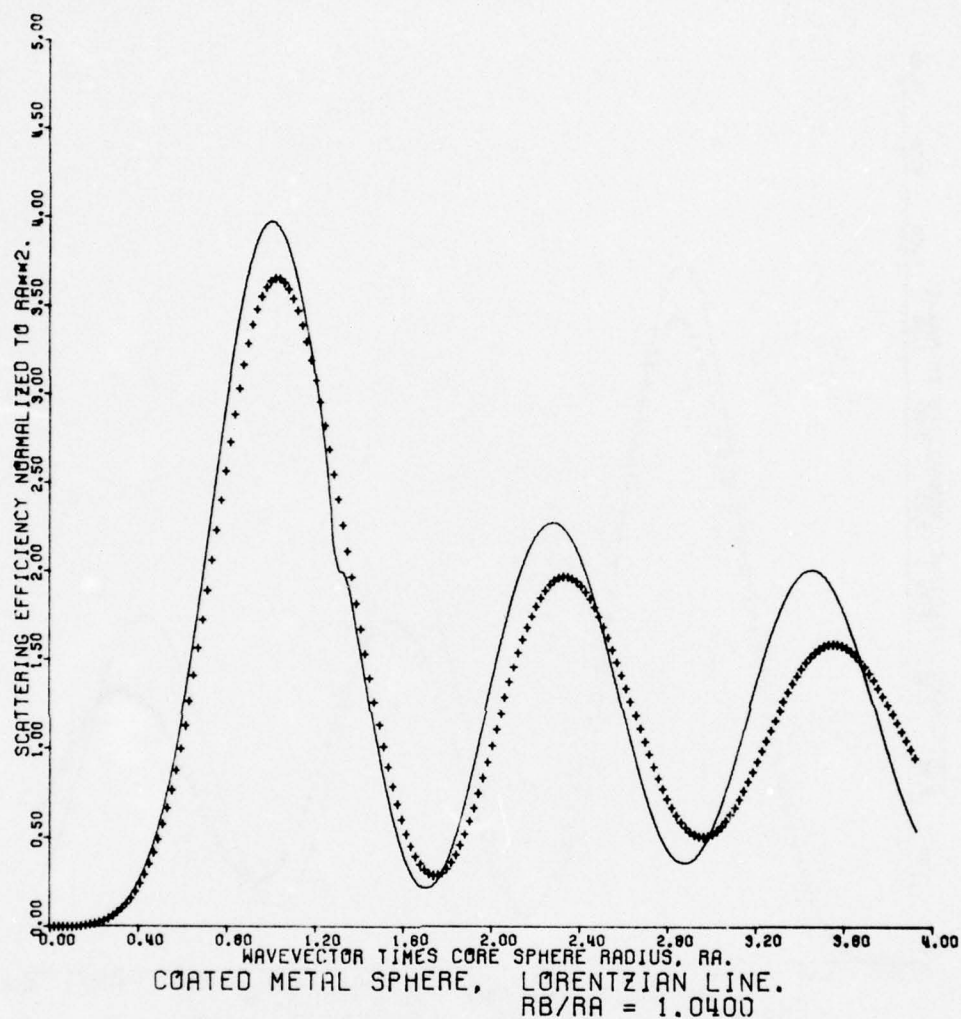


Fig. 3.47. Scattering from a coated metallic sphere having a 50 cm^{-1} fwhm absorption line at $ka = 1.26$ (solid curve). Results are normalized to the core cross-sectional area and compared to a perfectly conducting sphere of radius b (symbols).

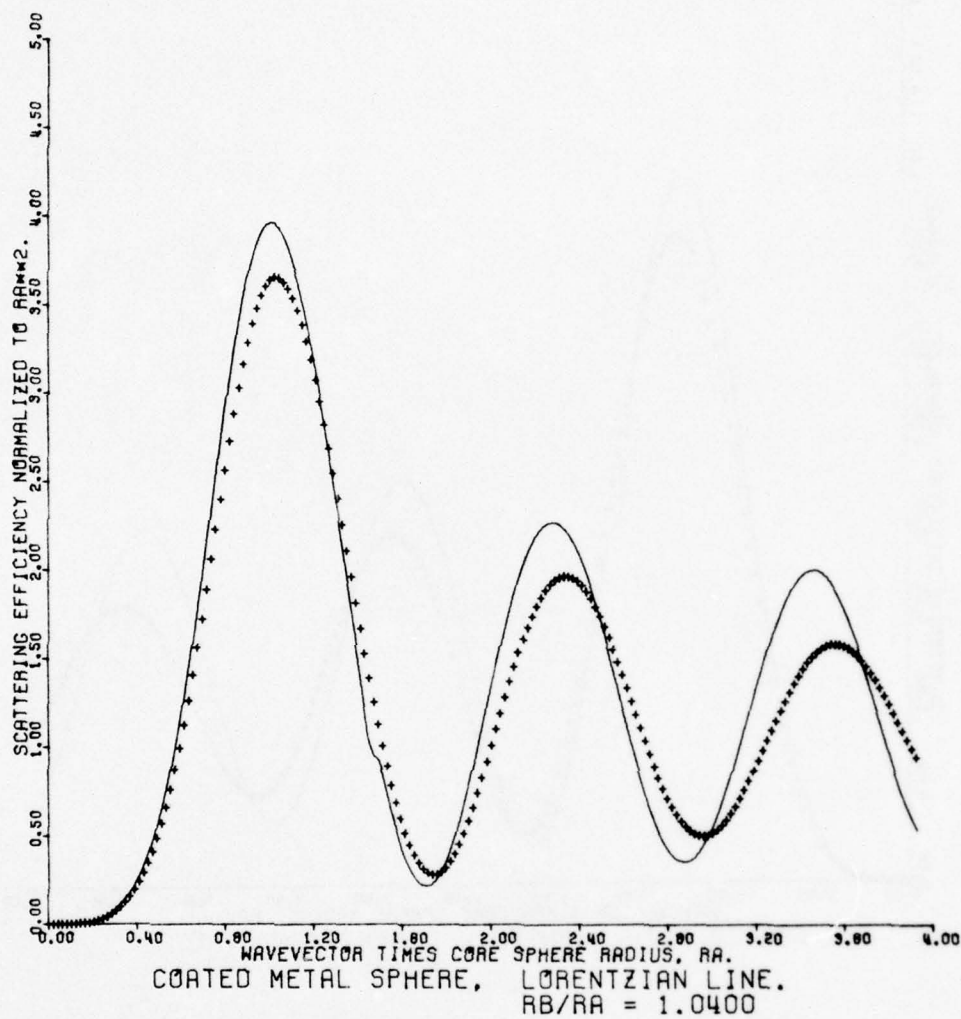


Fig. 3.48. Scattering from a coated metallic sphere having a 50 cm^{-1} fwhm absorption line at $ka = 1.43$ (solid curve). Results are normalized to the core cross-sectional area and compared to a perfectly conducting sphere of radius b (symbols).

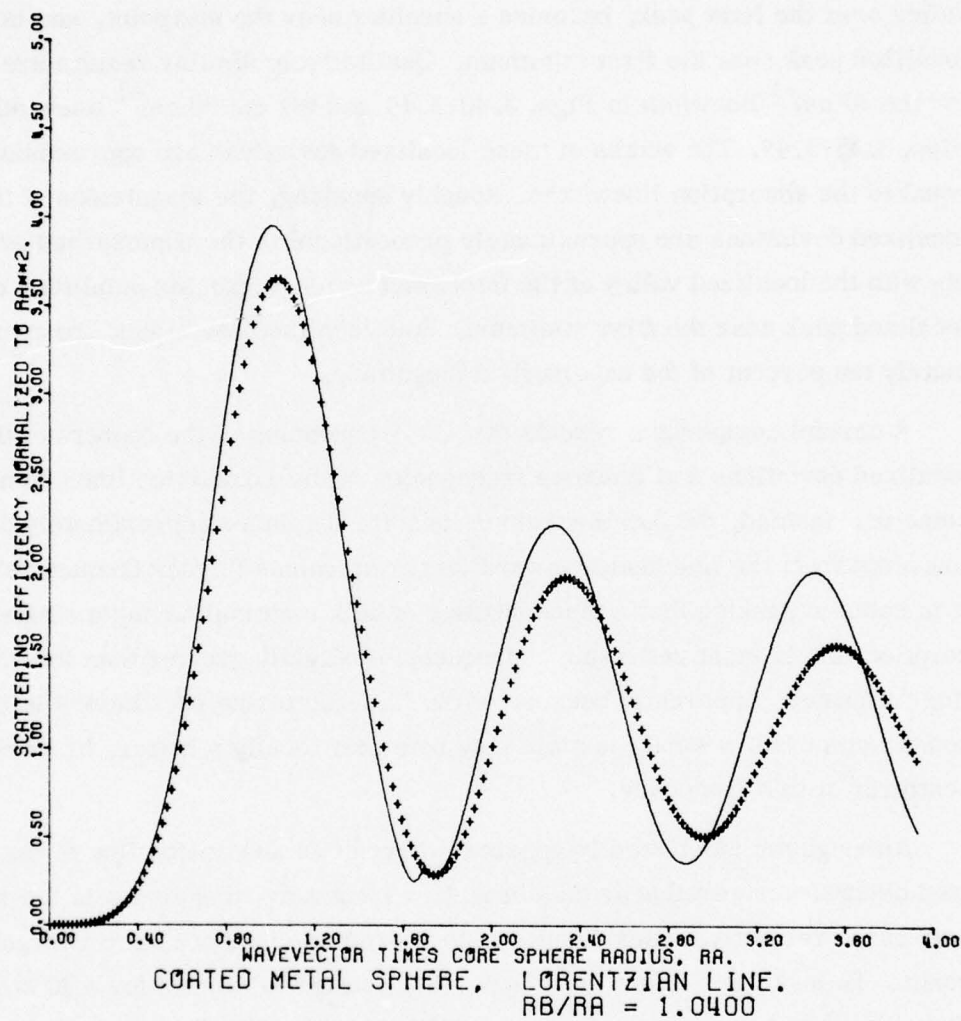


Fig. 3.49. Scattering from a coated metallic sphere having a 50 cm^{-1} fwhm absorption line at $ka = 1.65$ (solid curve). Results are normalized to the core cross-sectional area and compared to a perfectly conducting sphere of radius b (symbols).

The effect of the absorption-line frequency on the scattering is similar for all the linewidths. First consider the 10 cm^{-1} linewidth results shown in Figs. 3.35-3.39. The localized perturbation from the absorption line is a localized valley near the first peak, becomes a shoulder near the midpoint, and is a localized peak near the first minimum. Qualitatively similar results are given for the 20 cm^{-1} linewidth in Figs. 3.40-3.44 and for the 50 cm^{-1} linewidth in Figs. 3.45-3.49. The widths of these localized deviations are approximately equal to the absorption linewidths. Roughly speaking, the magnitudes of the localized deviations are approximately proportional to the unperturbed scattering with the localized valley at the first peak having a greater amplitude than the localized peak near the first minimum. Both localized deviations are approximately ten percent of the unperturbed magnitude.

A careful comparison reveals that the frequencies of the centers of the localized deviations and resonant frequencies of the Lorentzian lines do not coincide. Instead, the localized deviations are displaced approximately one linewidth from the line center toward larger ka values (higher frequencies). It is noted in passing that a plane surface of bulk material having a single absorption line is most reflecting at frequencies slightly greater than the absorption frequency. Apparently because of the Mie-scattering oscillations in the scattering curve, a small particle may be either locally a better, or worse, scatterer at this frequency.

Although the most readily apparent effect of an absorption line is the localized deviation centered near the absorption frequency, dispersion in the real part of the refractive index results in less dramatic changes over a larger range. To make this effect more apparent, scattering curves for a 10 cm^{-1} linewidth absorption line in the very thick coating having the radius ratio 1.4 are shown in Figs. 3.50 and 3.51. When these curves are carefully compared to Figs. 3.28 and 3.29 for the same thickness nondispersive coating having the same refractive index in the visible, it is seen that the coated-sphere curves cross the perfectly conducting sphere curves at slightly different positions.

The above results demonstrate that strongly absorbing Lorentzian absorption lines in sufficiently thick coatings have an observable effect on the scattering,

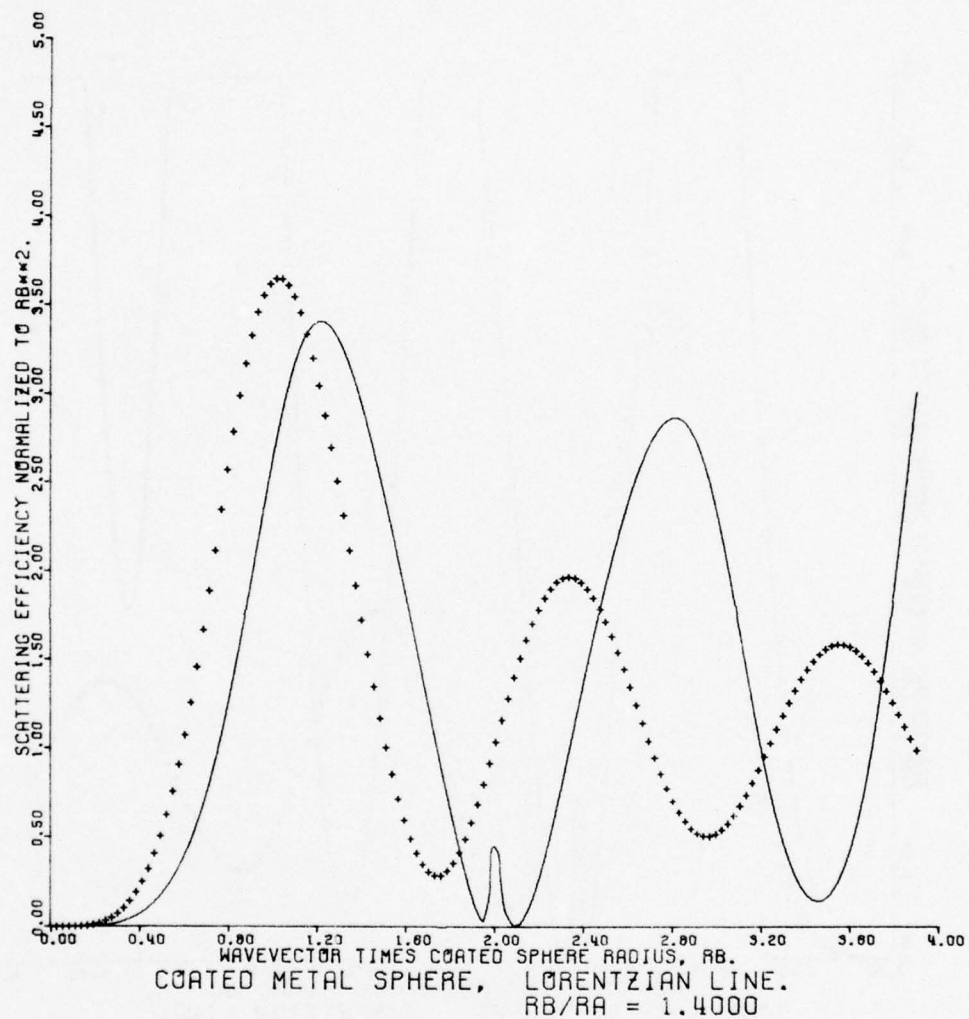


Fig. 3.50. Scattering from a coated metallic sphere having a 10 cm^{-1} fwhm absorption line (solid curve). Results are normalized to the total cross-sectional area and compared to a perfectly conducting sphere of radius b (symbols).

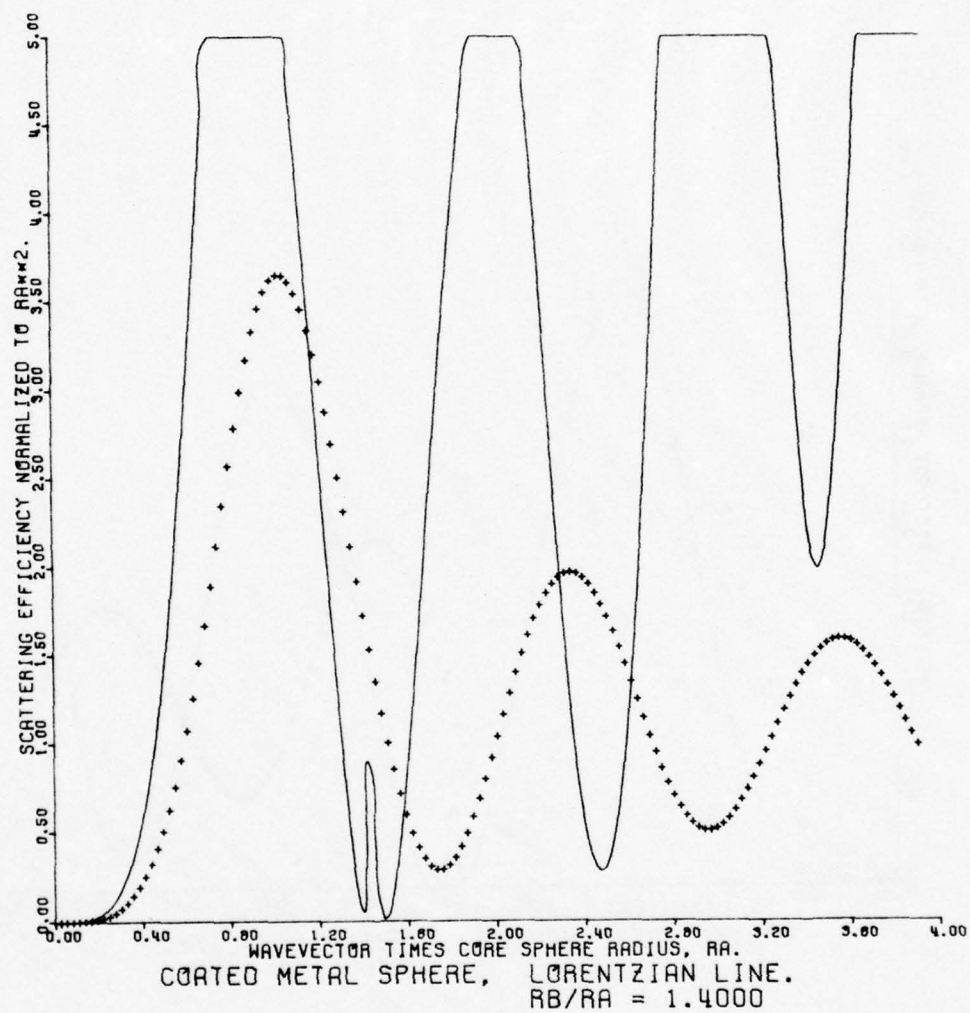


Fig. 3.51. Scattering from a coated metallic sphere having a 10 cm^{-1} fwhm absorption line (solid curve). Results are normalized to the core cross-sectional area and compared to a perfectly conducting sphere of radius a (symbols).

with the deviations from a smooth curve being highly visible since they are localized. With the relatively thick coatings having radius ratios 1.04 and 1.4, the magnitudes of the localized deviations are comparable to the differences between nondispersive coatings and uncoated spheres. Effects from thinner coatings and less absorbing lines are expected to be less severe.

The real and imaginary parts of the complex refractive index $m = n - ik$ of an actual metal oxide are plotted in units of ka in Figs. 3.52 and 3.53, respectively.²⁹ Two approaches can be taken to put these optical constants in a form for use by the computer in calculating the scattering from a metallic particle coated with this material: First, the imaginary part of the refractive index can be fit by a superposition of several Lorentzian lines. The correct dispersive behavior of the Lorentzian lines should automatically reproduce the real part of the refractive index. This set of Lorentzian lines can then be put in analytic form in a subroutine of the computer program. Secondly, one can simply tabulate the refractive index at the ka points where the scattering is calculated. Since many Lorentzian lines are needed to fit the optical constants in Figs. 3.52 and 3.53, the second approach was taken in calculating the following results.

The scattering from a metal-oxide coated, metallic sphere is shown in Fig. 3.54 as a function of ka for a radius ratio of $b/a = 1.04$. On the average, the scattering is similar to that from a sphere coated with a nondispersive coating of the same thickness. However, there are four narrow, localized valleys in the scattering curve: two of small amplitude at the ka values of 0.76 and 1.00 and two of large amplitude at the ka values of 1.39 and 1.43. The positions and magnitudes of these localized valleys do not correlate well with the positions and magnitudes of the absorption peaks. Time did not permit a detailed study of this effect. It appears that the localized effects of dispersion on the scattering may be most severe when the real part of the refractive index is small and the imaginary part is large. A possible explanation of the large magnitude, localized valleys is that the small real part of the refractive index allows much of the incident radiation to penetrate the coating. This radiation is then absorbed by the large imaginary part of the refractive index. Any future studies of this effect should also consider the possibilities of subtle resonance effects in the Mie scattering or an effective, localized horizontal displacement of the scattering

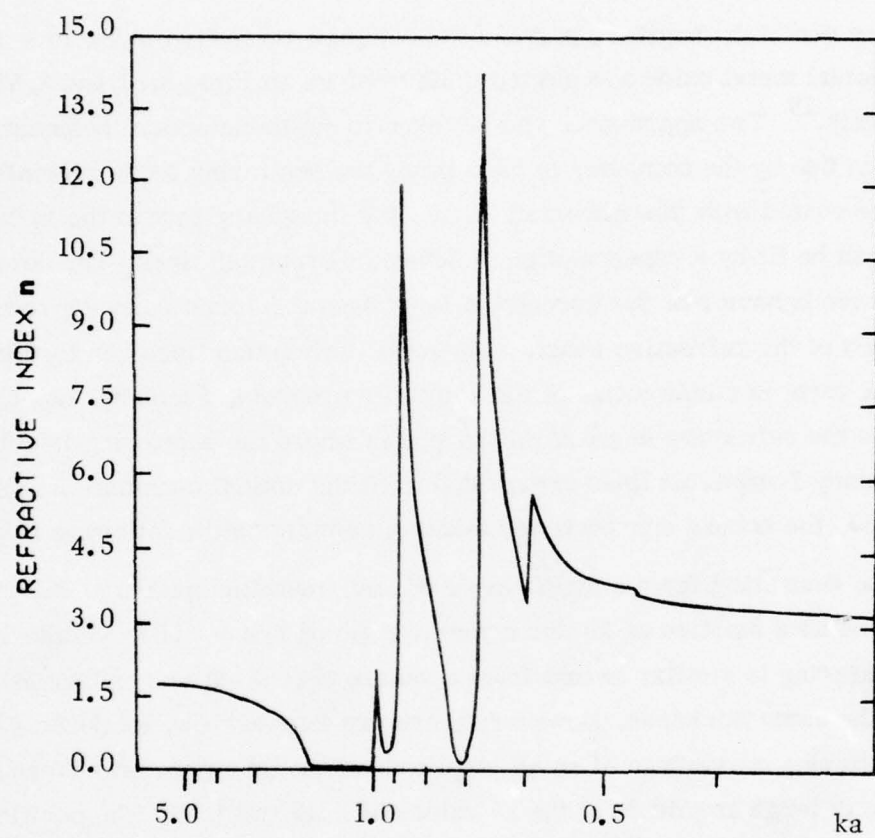


Fig. 3.52. Real part n of the refractive index of a metal-oxide coating.

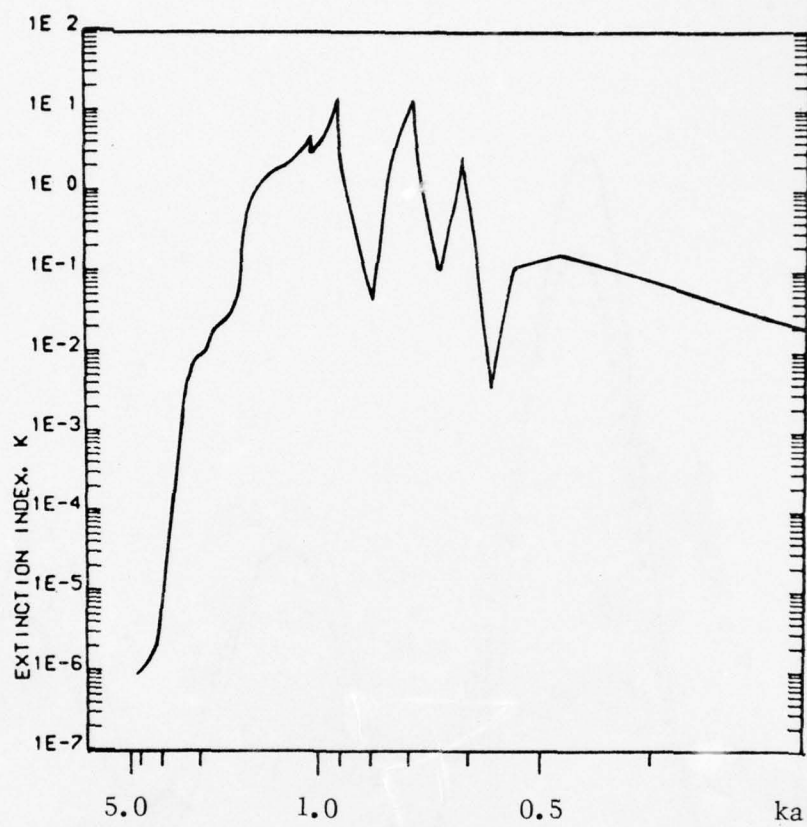


Fig. 3.53. Imaginary part k of the refractive index of a metal-oxide coating.

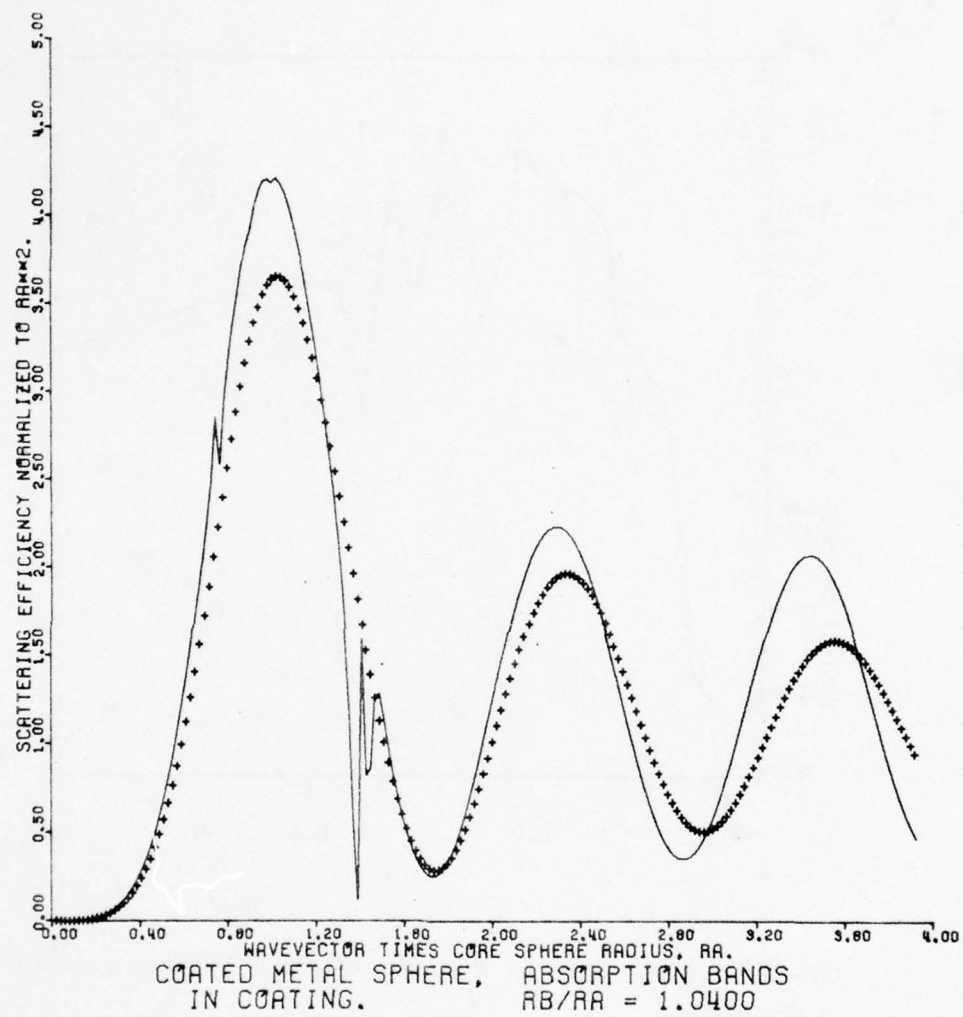


Fig. 3.54. Scattering from a metallic sphere coated with a metal-oxide coating.

at such points. A small, localized horizontal displacement in a rapidly varying portion of the scattering curve can result in a large vertical displacement.

Recall that a similar effect was observed above for a single Lorentzian line where it was observed that the center of the localized deviation in the scattering curve was slightly displaced toward higher frequencies. In this region approximately one linewidth above the resonant frequency, the real part of the refractive index passes through a minimum while the imaginary part is slowly varying and relatively small.³⁰

The real and imaginary parts of the refractive index of an absorbing dielectric material are plotted in Figs. 3.55 and 3.56.²⁹ Particles of this material, smaller in size than the primary particles, may be useful as spacer particles to prevent contact and cohesion of the primary particles. The scattering from the homogeneous dielectric spheres is plotted as a function of ka in Fig. 3.57. The ka range in this figure is smaller than previous figures, extending only to the first peak, because the wavelength range was kept constant and a smaller particle radius was used. In this region the scattering from the dielectric spheres is less efficient than from metallic spheres of the same size. There is one localized step in the otherwise slowly varying scattering curve at the ka value of 0.32. At this point, the real part of the refractive index is slowly varying but the imaginary part drops abruptly from one slowly varying value to another.

E. Summary and Conclusions of Scattering Study

Scattering from spheres is typically presented as a plot of the scattering efficiency as a function of ka , where $k = 2\pi/\lambda$ is the propagation constant of the radiation, λ is the radiation wavelength, and a is the sphere radius. In previous sections, scattering from coated spheres has been presented both in terms of the core radius a and total radius of the core plus the coating thickness b . The plot of the scattering for a metallic sphere is an oscillating curve having peaks near the ka values of 1.0, 2.3, 3.6, etc., with the peaks decreasing in amplitude as ka increases. There is no simple method for calculating the scattering when ka is of the order of unity. In this region it is necessary to use the

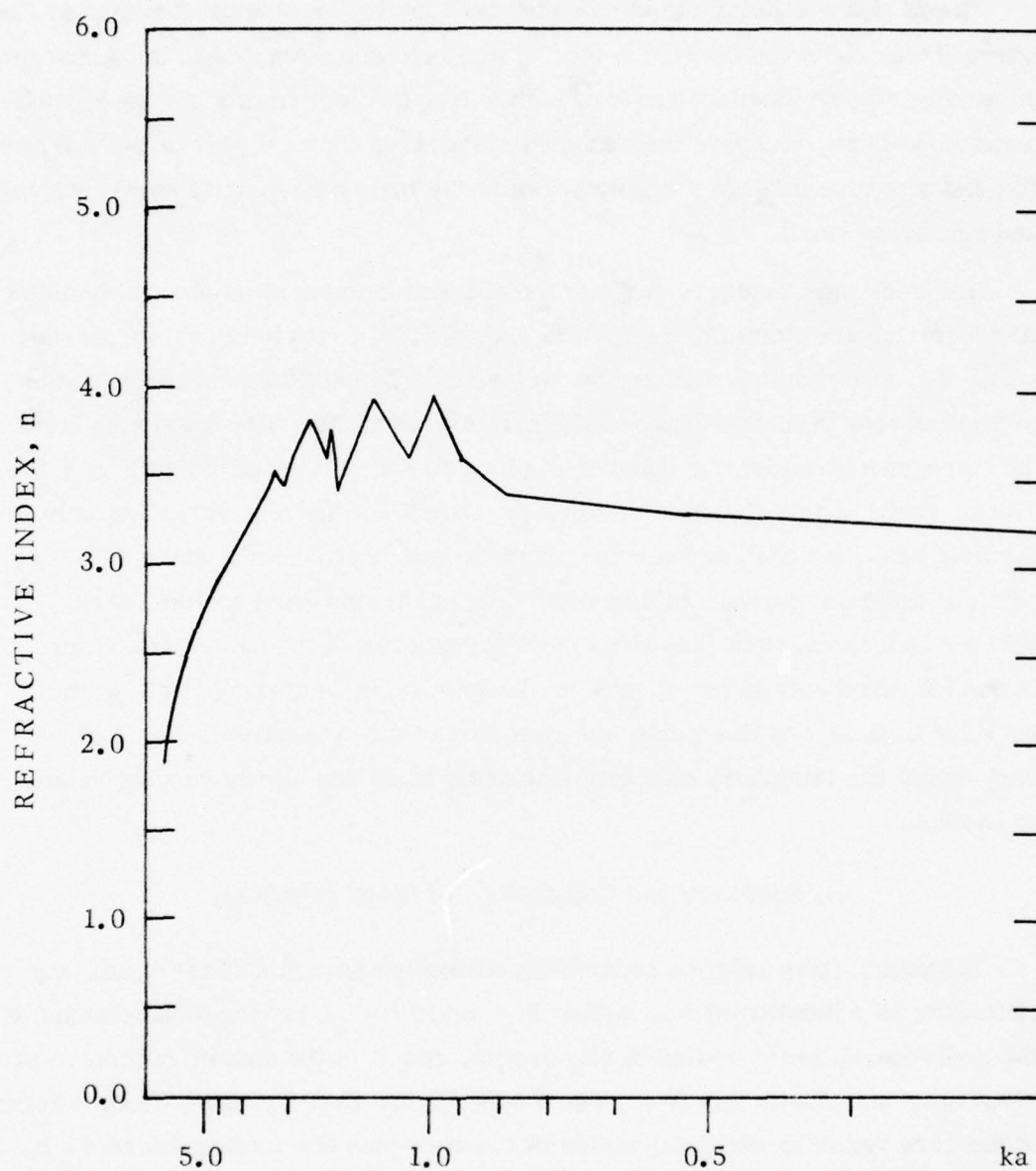


Fig. 3.55. Real part n of the refractive index of an absorbing dielectric material.

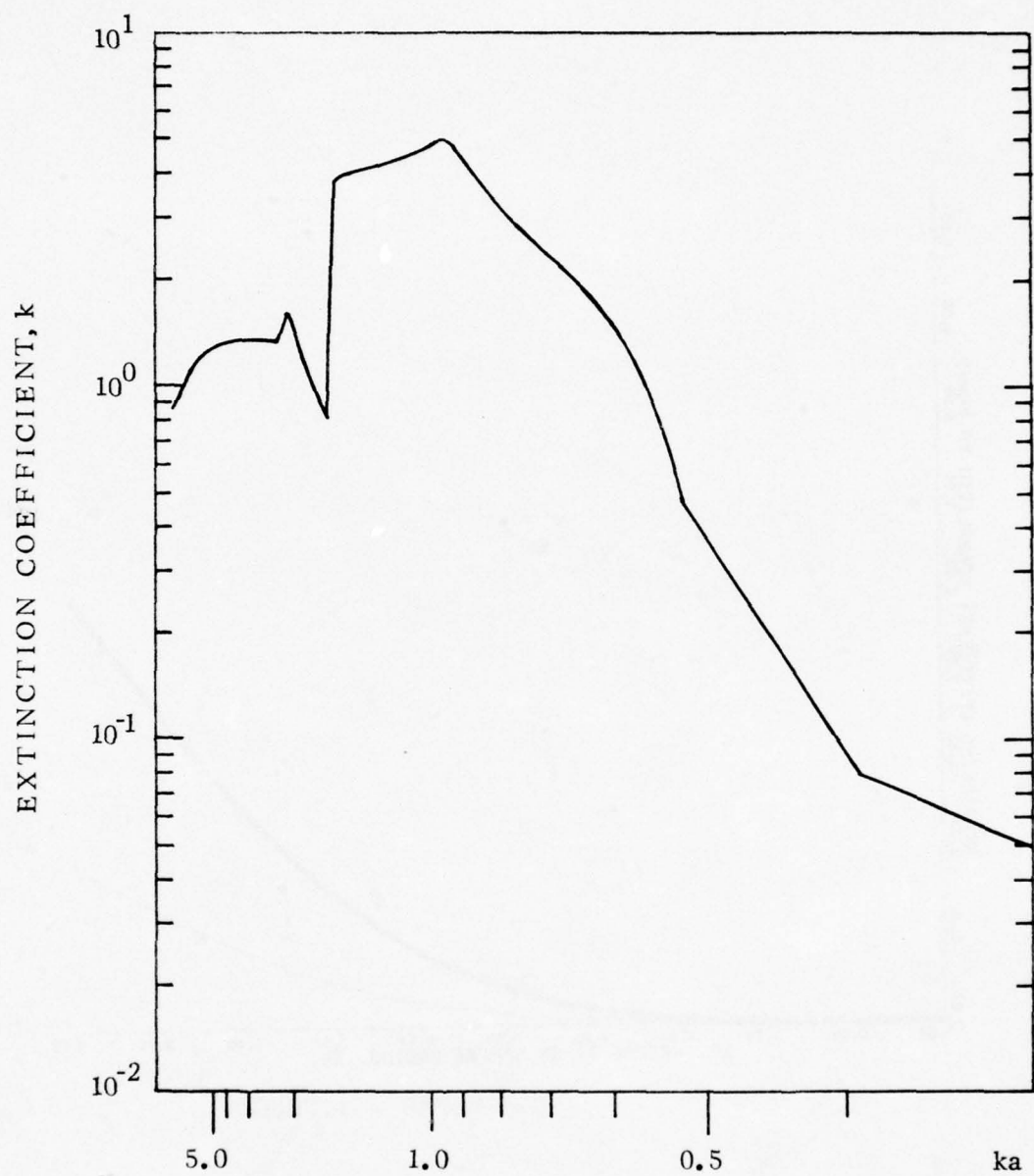


Fig. 3.56. Imaginary part k of the refractive index of an absorbing dielectric material.

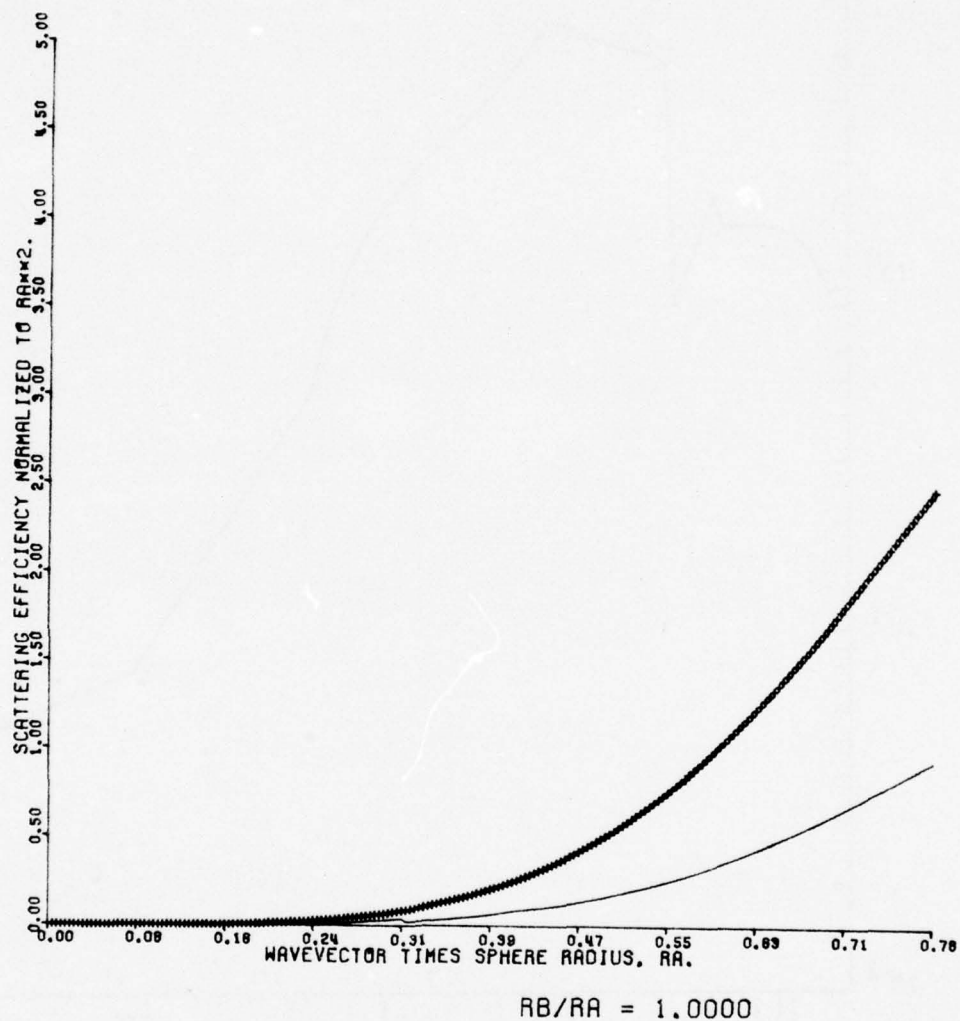


Fig. 3.57. Scattering from a small, homogeneous sphere of absorbing dielectric material.

complicated Mie-theory-series solution. This is in contrast to the simple approximations of geometrical optics and Rayleigh scattering (first term in Mie series) that can be made in the limits of very large and very small ka values, respectively.

Mie-scattering results for perfectly conducting spheres can be used as limiting approximations for scattering from coated and uncoated metallic spheres. However, for the determination of the effects of coatings on the scattering of a metallic sphere, this limit cannot be used because the effects of the coatings are often smaller than the differences in the scattering between actual metallic spheres and perfectly conducting spheres. The Mie-theory calculations performed in this study may be the first such calculations for an actual metal. These results for coated and uncoated metallic spheres have been compared qualitatively and quantitatively to scattering from perfectly conducting spheres.

With an uncoated metallic sphere, the positions of the maxima and minima in the oscillations of the scattering curve agree well with those of a perfectly conducting sphere. The amplitude of the oscillations is greater for an actual metal than for a perfect conductor, with the differences becoming greater with increasing ka . The maximum difference occurs at the first two minima where the scattering curve of the metallic sphere is approximately ten percent below that of a perfectly conducting sphere. The mean difference in the region between the first two peaks is four percent.

For coated spheres having coating refractive indices greater than approximately 1.6, the scattering is qualitatively similar to that from a perfectly conducting sphere having a radius equal to the total of the metallic core radius plus the coating thickness. With coating refractive indices less than this value, scattering from the coated sphere is better approximated by that from a perfectly reflecting sphere having the core radius. These respective approximations are obvious in the limits of a perfectly reflecting coating (infinite refractive index) and of a vacuum coating (refractive index of unity). The small value of the refractive index at the cross-over point is surprising in view of the small, bulk reflectivity of such a coating. In both comparisons the scattering curves for the coated, metallic sphere and the appropriate radius perfectly conducting

sphere are approximately in-phase, having maxima and minima at nearly the same positions. The amplitudes of the coated, metallic sphere curves are greater than those of the corresponding perfectly reflecting sphere curves with the difference increasing with increasing ka .

With coating thicknesses and refractive indices greater than those of current interest, waveguide modes can be set up in the dielectric coatings. In coatings where this occurs, these modes result in large magnitude, narrow spikes in the scattering curve at large ka values.

To investigate the effects of the coatings quantitatively, the root-mean-square percent deviation (RMS%) between the coated sphere scattering and that from the uncoated metallic sphere core was calculated for the ka region between the first two peaks in the scattering curve. With thin coatings that have a ratio of the coated sphere radius to the core radius less than approximately 1.04, the RMS% deviation is approximately linear in the coating thickness at a fixed refractive index. For coatings having refractive indices less than 4.0, the RMS% deviation is less than 0.3% for a radius ratio of 1.0004, less than 3% for the radius ratio 1.004, and less than 30% for the radius ratio 1.04.

With nondispersive absorbing coatings, the scattering results are qualitatively and quantitatively the same as those for nondispersive transparent coatings having the same magnitude refractive indices, except for small quantitative differences at small magnitude indices.

Actual absorbing coating materials have dispersive absorption bands. The effect of dispersive absorption on the scattering was first studied using a model coating having a single Lorentzian-shaped absorption line of varying linewidths and varying frequencies. The use of a Lorentzian line guarantees the correct dispersive behavior of the refractive index. In this study the coating thickness was held constant at a radius ratio of 1.04 and the absorption coefficient at the line center was held constant at 10^4 cm^{-1} . Three absorption linewidths (10 cm^{-1} , 20 cm^{-1} , and 50 cm^{-1}) were examined at five frequencies equally spaced in wavelength between the first maximum and the first minimum on the scattering curve. The absorption lines resulted in localized deviations in the scattering curve located near the resonant frequency of the Lorentzian line and having approximately

the same width as the absorption line. A close examination reveals that the localized deviation is displaced in frequency approximately one linewidth toward the high frequency side of the absorption line at the point where the real part of the refractive index is a minimum.

The shape of the localized deviation is primarily dependent on the frequency of the absorption line and is dependent to a lesser extent on the linewidth. The results for the 10 cm^{-1} linewidth are representative: At the first maximum in the scattering curve the absorption line results in a localized valley of approximately 10 cm^{-1} linewidth. Near the midpoint between the first maximum and the first minimum, the localized deviation becomes a shoulder in the scattering curve. A localized peak is observed for frequencies near the first minimum. The magnitudes of the localized deviations are approximately proportional to the local value of the scattering curve. With the radius ratio of 1.04 and the absorption coefficient of 10^4 cm^{-1} used, both the local valley at the first maximum and the local peak at the first minimum have a magnitude of approximately ten percent of the value of the scattering curve at these positions for all absorption linewidths.

The localized deviations from absorption bands in an actual metal-oxide coating were also investigated. It is observed that magnitudes of the localized deviations in the scattering curve do not correlate well with the peaks in the absorption coefficient of the coating. Rather, the most severe localized effects appear to occur when the real part of the refractive index is small and the imaginary part is large.

Scattering from homogeneous dielectric particles smaller in size than the primary particles was also examined. On the average, the scattering is less efficient than from the same size metallic particle. There is one localized valley in the scattering curve at a point where the real part of the refractive index is small and slowly varying and the imaginary part changes abruptly from one slowly varying value to another.

With the 1.04 radius ratio and the absorption coefficient of 10^4 cm^{-1} used in the study of the Lorentzian absorption lines, the magnitudes of the localized

deviations are comparable to those from nondispersive coatings of the same thickness. However, in contrast to nondispersive coatings where the deviations are spread over large ka ranges, the deviations caused by absorption lines are more visible because they are localized. These effects are expected to be less severe with thinner coatings and smaller absorption coefficients and more severe with thicker coatings and larger absorption coefficients. The localized effects of the absorption lines may be ameliorated somewhat in practical situations where there is a distribution of sphere sizes. In this case some smoothing is expected from the fact that the localized deviation from a fixed wavelength absorption line may be a local valley for one size and a local peak for another size yielding partial cancellation.

REFERENCES

1. C. Orr, Jr., Particulate Technology (MacMillan, New York, 1966).
2. R. J. Good, in Treatise on Adhesion and Adhesives, edited by R. L. Patrick (Marcel Dekker, New York, 1967).
3. F. P. Bowden and D. Tabor, The Friction and Lubrication of Solids, Vol. I and II (Oxford, New York, 1964); Friction (Anchor Press, Doubleday, New York, 1973).
4. E. Rabinowicz, Friction and Wear of Materials (Wiley, New York, 1965).
5. J. Skelton, Science 190, 15 (1975).
6. D. A. Zimon, Adhesion of Dust and Powder (Plenum, New York, 1969).
7. F. M. Fowkes, "Contact Angle, Wettability, and Adhesion," Vol. 43 of Advances in Chemistry Series, edited by R. F. Gould (American Chemical Society, Washington, D. C., 1964).
8. Force equation from T. Gillespie and G. D. Rose, J. Colloid Interface Sci. 26, 246 (1968). Following this paper are several other notes in response to an incorrect treatment by T. Gillespie and W. J. Settineri, J. Colloid Interface Sci. 24, 199 (1967).
9. (a) J. C. Melrose, A. I. Ch. E. Journal 12, 986 (1966).
(b) J. C. Melrose and G. C. Wallick, J. Phys. Chem. 71, 3676 (1967).
10. P. F. Scholander, Am. Sci. 60, 584 (1972).
11. A. T. Hayward, Am. Sci. 59, 434 (1971).
12. R. C. Reid, Am. Sci. 64, 146 (1976).
13. M. H. Zimmermann, Sci. Am. 208, 133 (1963).
14. C. D. Hendricks, in Electrostatics and its Applications (Wiley-Interscience, New York, 1973).
15. W. R. Harper, Contact and Frictional Electrification (Oxford, New York, 1967).

16. H. L. Green and W. R. Lane, Particulate Clouds: Dusts, Smokes, and Mists (Von Nostrand, Princeton, 1957).
17. D. Langbein, Theory of Van der Waals Attraction (Springer-Verlag, New York, 1974).
18. R. J. Roark, Formulas for Stress and Strain (McGraw-Hill, New York, 1965).
19. A. N. Wright, *Nature* 215, 953 (1967).
20. D. H. Maylotte and A. N. Wright, to be published in Discussions of the Faraday Soc. First Joint Meeting with Bunsengesellschaft and Societé Chemie Physique, Cambridge, England, September (1974).
21. B. L. Weigand, Third Conference on High Power Infrared Laser Window Materials, Vol. III, 769 (1974).
22. A. S. Akmatov, Molecular Physics of Boundary Friction (Israel Program for Scientific Translations, Jerusalem, 1966).
23. M. Kerker, The Scattering of Light and Other Electromagnetic Radiation (Academic, New York, 1969). The notation in this reference is used in this report.
24. Another useful reference on scattering is H. C. van de Hulst, Light Scattering by Small Particles (Wiley, New York, 1957).
25. The theory of Mie scattering is also considered in J. Stratton, Electromagnetic Theory (McGraw-Hill, New York, 1941) and M. Born and E. Wolf, Principles of Optics (Pergamon, Oxford, 1959).
26. M. Abramowitz and I. A. Stegun, Handbook of Mathematical Functions, AMS 55 (National Bureau of Standards, Washington, D. C., 1964).
27. H. Scharfman, *J. Appl. Phys.* 25, 1352 (1954).
28. J. Rheinstein, *IEEE Trans. Antennas Propagation* AP-12, 334 (1964); AP-13, 983 (1965).
29. M. E. Whitson, Aerospace Corp. Report No. SAMSO-TR-75-131, Vol. I (1975).
30. F. Wooten, Optical Properties of Solids (Academic, New York, 1972), pp. 46-50.

APPENDIX A. DESCRIPTION OF THE SUBROUTINES AND THEIR FUNCTION

Listings of the computer codes may be found in Appendix D.

SCATER: Main program. The main program has four nested loops. The outermost loop is executed NCASES times. It is normally used to run sequences of spheres of different radii, but may also be used to control the plotting of each case or to vary the range over which the RMS% deviation is computed. The next loop is executed MVM times and is used to initialize the refractive index formulas. The third loop varies ka from zero to 4.0. The refractive indices are evaluated at each wavelength by calls to COREM1 and COAT1, and then all the various arguments of the Riccati-Bessel functions are formed. The next section evaluates the psi and chi Riccati-Bessel functions by calls to INITAL which in turn calls PSI, PSI910, and FORWAD.

The innermost loop completes the computation of the Riccati-Bessel functions by calls to RECURR and sums the scattering coefficients of orders 1-10 to get the scattering amplitudes. Upon leaving the innermost loop the scattering is computed and the wavelength range has been covered, the RMS% deviation is computed by calls to SUMSQ, and the results are plotted by calls to LFARGE and PLOTTT.

PSI910: generates $\psi_9(z)$ and $\psi_{10}(z)$ from the sine-cosine polynomials (3.28) and (3.29) for large arguments.

PSI: generates $\psi_9(z)$ and $\psi_{10}(z)$ from the power series (3.30) for small arguments.

FORWAD: is used to generate ψ_1 - ψ_8 by backwards recursion from ψ_9 and ψ_{10} , or to generate χ_3 - χ_{10} by forward recursion from χ_1 and χ_2 .

RECURR: computes the zeta functions and all function derivatives of any given order V , between one and ten, and then computes the V th order scattering coefficients for the core and coated spheres. Common area REX passes arguments and function values between RECURR and SCATER.

SUMSQ: calculates the RMS% deviations between the coated-sphere gain curve and the perfectly conducting or core-sphere gain curves, over a specified range of ka and kb :

$$\text{RMS \% deviation} = 100 \sqrt{\sum_{i=KI}^{i=KF} \left[\left(G1(i) - G2(i) \right) / G2(i) \right]^2} .$$

COATM2: entries COAT1 and COREM1. COATM2 is a user-supplied routine that provides the dispersion relations for the core and coating refractive indices. For each pair of radii (or each value of MV in the range $1 \leq MV \leq MVM$), SCATER makes a call to COATM2 before each run through its range of wavelengths. This call should be used to initialize the dispersion relations of the core and coating for that particular run. Subsequently SCATER makes successive calls to COAT1 and COREM1 for the complex, double precision values of M2 and M1 at each wavelength.

Four routines already exist and can serve as models. (See Appendix D for listings.) One, COAT, provides for linear dispersion in the real and imaginary parts of the refractive indices, while another, COAL, provides for a Lorentzian absorption line in the coating material with linear dispersion in the core. Numerical tables for realistic complex refractive indices are used in COAS for a metal-oxide coating, and in COAC for a solid dielectric sphere.

LFARGE: entry PLOTTT. There is one call to LFARGE for each set of axes. Calls to LFARGE(NCK) give:

NCK = 1; initializes plotter by a call to PINIT.

NCK = 1 or 2; reads cards containing x and y axis lengths, variable ranges, plot scale factors and axis and graph titles. Then axes and titles are plotted.

A call to PLOTTT is made for every data curve to be plotted. Any number of curves may be placed on one set of axes. The last call to PLOTTT for a given set of axes also controls the advance to the next plot if NTG = 2, and closes the plotter data set on the last call of a complete run by setting NTG = NENDPL = 2.

Note that the plotter routine may change the data arrays given to it. Presently, if y-axis array elements have magnitudes outside the range of the y axis drawn by the previous call to LFARGE, the offending elements are truncated to the nearest limit. Further, the plotter routines require storage of the minimum value plotted

on the axis and the number of units per inch to be stored near the end of the arrays. Normally, if all elements are plotted, those data are stored in the last two array elements which are reserved for that purpose. Additional explanation may be found in the comments in LFARGE in the listing of Appendix D.

The routines called by LFARGE are standard CALCOMP software and descriptions may be found in the manufacturer's plotter manuals. There are three exceptions:

- PINIT(XX): initializes the plotter output on Fortran device number XX, and writes a user ID on the plot.
- DFACT: sets both plot scale factors.
- ENPLT: closes plotter output file and plots user ID.

APPENDIX B. INPUT DATA CARD DESCRIPTION

This appendix describes the input data cards required by the computer program SCATER and its subroutines. Included are card ordering, variables read, and Fortran formats, as well as a description of the function of the variables in the program and a sample data card set.

On some of the data cards, blank formats, such as "10X," are specified to allow the user to identify the variable on the data card by its name, a mnemonic or its format.

CARD	VARIABLES	FORMAT
<u>Cards 1-5:</u>	COMENT	(20A4)

These cards, which can contain alphanumeric characters, provide a five-line descriptive title for each run. They may be left blank but cannot be omitted.

<u>Card 6:</u>	NCASES	(10X, I4)
----------------	--------	-----------

This card contains the number of different pairs of radii, (a,b), to be studied in the run.

The user must provide one set of all the following cards for each pair of radii, NCASES sets in all.

<u>Card 7:</u>	RA, RB	2(10X, D24. 17)
----------------	--------	-----------------

Reads core and coated sphere radii.

<u>Card 8:</u>	MVM, NPLOT, KI, KF	4(10X, I4)
----------------	--------------------	------------

MVM is the number of different refractive indices or materials to be run for this pair of radii.

NPLOT controls the flow of data to the plotter: plots if NPLOT = 0, no plot if NPLOT = 1.

KI, KF is a pair of integers used by subroutine SUMSQ. SUMSQ finds the RMS% deviation of the gains over a range of ka whose upper and lower bounds are APLOT(KI) and APLOT(KF), respectively.

••

The user must supply one set of all the following cards for each material-MVM sets for each pair of radii.

Card 9: RM1, SRM1, EM1, SEM1 (7X, D13.6)

Card 10: RM2, SRM2, EM2, SEM2 (7X, D13.6)

These cards are read by subroutine COATM2 to provide the initialization constants for complex slope-intercept dispersion relations for the core and coating. If the user supplied a different subroutine for calculating the refractive indices, the number and format of these cards could change.

•••

The following cards are read by subroutine LFARGE to provide data to the plotter. They are provided only if NPLOT = 1. There are two sets of these cards for each material or refractive index. The first set is for a plot of G_{∞} and G_{coated} vs ka , while the second is for a plot of G_{∞} and G_{coated} vs kb .

Card 11: LABELX (15A4)

60 character alphanumeric title for the x axis.

Card 12: LABELY (15A4)

60 character alphanumeric title for the y axis.

Card 13: LABELG, LABELH 2(10A4)

Two line, 80 character alphanumeric title for the graph.

Card 14: XMIN, XMAX, SIDEX, XFCT, YMIN, (8G10)
YMAX, SIDEY, YFCT

The first four variables refer to the x axis and the second four to the y axis. We describe the x-axis variables only since the y-axis variables have the equivalent meanings.

YMIN, XMAX are the minimum and maximum values of the x variable written on the x axis.

SIDEX is the length of the x axis in inches.

XFCT is a scaling factor that multiplies the x dimension of graphs, titles, and axes.

It is suggested that if the over-all dimensions of the graph axis are significantly less than 8" x 8", this should be accomplished by making XFCT and YFCT less than unity. XFCT and YFCT reduces the sizes of titles, axes, and graphs together thus keeping them proportionate.

Also note that in most cases G_{∞} and G_{coated} have a maximum value of about 4.0 when plotted vs kb and normalized to b^2 . But G_{coated} will be larger by the ratio $(b/a)^2$ when plotted vs ka and normalized to a^2 . This should be taken into account when choosing the YMAX values if $(b/a)^2$ is significantly different from one.

Figure B.1 is a listing of a typical set of data cards for the coated-sphere scattering program when the coating has a Lorentzian absorption line. In the two columns on the right-hand side of the figure, the cards are given a sequential card number and a card-type number which refers to the card descriptions given above. The repetition of the card types is evident from the figure. Briefly, since NCASES = 2 on card #6, we have two complete data groups beginning at cards #7 and #39. On card #8, MVM = 3, so three different material subcases follow. In particular, these three sets of data cards were used to generate the graphs in Figs. 3.35-3.42 for metal cores clad with materials having different Lorentzian absorption lines. The second group beginning at card #39 has $a = 2.5$ and $b = 3.5$, so $(b/a)^2 \sim 2$ and the coated-sphere gain curve will be about twice as large as the perfectly conducting sphere curve when plotted vs ka . Therefore on card #46 we have doubled the length of the y axis in the manner suggested above.

APPENDIX C. LIST OF VARIABLES

The variables in all program segments except SCATER and RECURRE are well-defined by the subroutine descriptions (Appendix A), the input data card descriptions (Appendix B), and comment cards in the program listings (Appendix D). This appendix contains a descriptive list of the important variables used in SCATER and RECURRE other than the input variables described in Appendix B.

The names of all the Riccati-Bessel functions and their derivatives are constructed from the following mnemonic:

- 1) The first letter of the name indicates the type of Riccati-Bessel function according to:
$$\psi \rightarrow S, \chi \rightarrow X, \xi \rightarrow Z.$$
- 2) The remainder of the name is the computer name of the argument:
$$A, N, M1A, M2A, M2N.$$
- 3) The ψ and χ functions are stored in arrays whose subscript equals the order of the Bessel function.

In all other cases the order is the current value of the integer variable V .
- 4) The name is preceded by a "D" if it is the derivative of the function.

In Table C.1 all arrays are underlined and all arrays used by the plotter end in "PLT."

Table C.1. Description of program variables.

<u>Variable</u>	<u>Description</u>
KIP	= number of frequency (or wavelength) values
KEP	= dimension of plotter arrays
PI2	= 2π
I	= complex imaginary unit
ZERO	= complex zero
RA	= core sphere radius, a
RB	= coated sphere radius, b
L	= wavelength, λ
M1	= core refractive index, m_1
M2	= coating refractive index, m_2
A, DA	= $\alpha = ka$ }
N, DN	= $\nu = kb$ } second variable is complex
APLT	= ka
BPLT	= kb
M1A	= $m_1\alpha = m_1ka$
M2A	= $m_2\alpha = m_2ka$
M2N	= $m_2\nu = m_2kb$
TA	= complex sine of Bessel's function argument
TB	= complex cosine of Bessel's function argument
V	= order of the current scattering coefficient
VP1	= $V + 1$
VM1	= $V - 1$

Table C.1. Description of program variables (Continued).

<u>Variable</u>	<u>Description</u>
AN, BN	= sequentially, these become the scattering coefficients for the coated sphere and then the perfectly conducting sphere, of order V
ALN, BLN	= core scattering coefficients of order V
G	= scattering amplitude of coated sphere
GI	= scattering amplitude of perfectly conducting sphere
GAL	= scattering amplitude of core sphere
GPLT	= gain of coated sphere normalized to a^2
GIPLT	= gain of perfectly conducting sphere normalized to b^2
GALLON	= gain of core sphere normalized to b^2
GBPLT	= gain of coated sphere normalized to b^2

APPENDIX D. COMPUTER CODE LISTINGS

LISTING OF CONTROL CARD / INPUT DATA

```

REACTION=0BOTH,SEQ=MAIN0000
C SCATTER.....COATED SPHERE PLANE WAVE SCATTERING PROGRAM.
C IMPLICIT REAL*8(C,E,F,H,O-R,U-W,Y),COMPLEX*16(A,B,D,G,I,M,S,T,X,
C LAST TWO POSITIONS IN THE FOLLOWING ARRAYS ARE FOR PLOTTER ONLY.
C REAL*4 APLT(202),GPLT(202),GIPLT(202),BPLT(202),GBPLT(202),AMAX,
1 GALLON(202)
C REAL*8 A,L,N
C INTEGER*4 V,
COMMON /RX/I,M1,M2,M1A,M2A,M2N,A,AN,BN,ALN,BLN,
1 SN(10),OSN,XN(10),
2 SM1A(10),
2SM2A(10),
3XN(10),
4ZN ,OZN ,SA(10),XA(10)
C REAL*4 COMMENT(1000)
C KIP IS THE NUMBER OF FREQUENCY VALUES AND KEP IS THE DIMENSION OF
C THE PLOTTER ARRAYS, KEP = KIP*2.
DATA PI2/6.2831853071795865D+00/,KIP,KEP/200,202/,
1 ZERO/(0.0D+00,0.0D+00)/
C CALL I8V ERROR MESSAGE CONTROL TO SURPRESS UNDERFLOW PRINTOUT.
C CALL ERSET(208,0,-1,1)
1(0.0D+00,1.0D+00)
READ 1000,COVENT
1000 FORMAT(20A4)
PRINT 1004,COMMENT
1004 FORMAT(1H ,20A4/(1H ,20A4))
READ 1006,NCASES
1006 FORMAT(10X,14)
PRINT 1007,NCASES
1007 FORMAT(1H ,//1H ,NUMBER OF DIFFERENT RADII = ,I4)
NCASE=1
JUMP=1
3 READ 1001,RA,RB,MVM,NPLOT,KI,KF
1001 FORMAT(2(10X,D24.17)/4(10X,I4))
NCASE=NCASE+1
PRINT 1003,MVM ,NPLOT
1003 FORMAT(1H ,//1H ,NUMBER OF DIFFERENT COATINGS = ,I4//1H ,
1 ,TO PLOT (=0) OR NOT TO PLOT (=1): NPLOT = ,I4)
C LOOP OVER DIFFERENT REFRACTIVE INDEX VARIATIONS.
DO 5 MVE=1,MVM
DO 5 MVE=1,MVM
C INITIALIZE REFRACTIVE INDEX FORMULA.
CALL COATN2(MV)
PRINT 1002,PA,RB,MV
1002 FORMAT(1H ,//20X ,INNER RADIUS=,F7.4,10X ,OUTER RADIUS=,F7.4,
1 10X ,MV = ,I4//1H ,
2 4X ,KA ,6X ,KB ,10X ,L ,17X ,M1 ,22X ,M2 ,33X ,
3 ,SCATTERING GAIN//1H ,
4 86X ,CORE ,7X ,COATED ,10X ,INFINITY ,5X ,COATED//1H ,
5 94X ,NORMALIZED TO RA**2 ,10X ,NORMALIZED TO RB**2//1H ,
C VARIATION OVER WAVELENGTH OR WAVE VECTOR.
DO 40 LV=1,KIP
L=(4.0*KIP)/LV
C INDEX OF REFRACTION OF THE CORE.
CALL COREM1(M1,L)
C EVALUATE COATING REFRACTIVE INDEX.
CALL COAT1(M2,L)
APLT(LV)=RA/L
DA=A
NPI=12*RB/L
BPLT(LV)=N

```


LISTING OF CONISOL CARD / INPUT DATA

CARD NO

```

DN=N
W1A=M1*A
W2A=M2*A
W2N=M2*N
C COMPUTE CHI AND PSI RICCATI-BESSEL FUNCTIONS OF ALL ARGUMENTS.
CALL INITIAL(I, XN, SN, DN, 0)
CALL INITIAL(I, XA, SA, DA, 0)
C ARRAY XM2A IS USED AS A DUMMY ARRAY IN THE NEXT CALL TO INITIAL
C BECAUSE THERE ARE NO CHI FUNCTIONS FOR THE INNER SPHERE.
CALL INITIAL(I, XM2A, SM1A, M1A, 1)
CALL INITIAL(I, XM2A, SM2A, M2A, 0)
C END OF RICCATI-BESSEL FUNCTION COMPUTATION.
C ZERO SCATTERING AMPLITUDES BEFORE SUMMATION.
G=ZERO
GI=ZERO
GAL=ZERO
DO 50 V=1,10
CALL RECURR(V)
C SCATTERING AMPLITUDE OF COATED SPHERE.
G=G+(V+0.5)*(AN-BN)*(-1.0)**V
C SCATTERING AMPLITUDE OF PERFECTLY CONDUCTING SPHERE OF RADIUS RB.
AN=DSN /DZN
BN=SN(V)/ZN
GIEG(V+0.5)*(AN-BN)*(-1.0)**V
C SCATTERING AMPLITUDE OF CORE SPHERE.
GAL=GAL+(V+0.5)*(ALN-BLN)*(-1.0)**V
50 CONTINUE
C GAINS NORMALIZED TO A**2.
GPLT(LV)=(4.0/A**2)*G*DCONJG(G)
GIPLT(LV)=(4.0/A**2)*GI*DCONJG(GI)
GALLON(LV)=(4.0/A**2)*GAL*DCONJG(GAL)
C GAINS NORMALIZED TO B**2.
GBPLT(LV)=(A/N)**2*GPLT(LV)
PRINT 1005, A,N,L,M1,M2,GALLON(LV),GPLT(LV),GIPLT(LV),GBPLT(LV)
1005 FORMAT(1H,2F8.3,4X,F8.3,2(5X,2F12.4))
40 CONTINUE
C COMPUTE RMSX DEVIATIONS.
CALL SUMSQ(GPLT,GALLON,APLT,K1,KF,1)
CALL SUMSQ(GBPLT,GIPLT,BPLT,K1,KF,2)
IF(NPLOT.EQ.1) GO TO 5
C PLOT GAINS VS KA OR KB.
IF(MV.EQ.1) GO TO 6
CALL LFARGE(2)
GO TO 9
C INITIALIZE THE PLOTTER.
6 CALL LFARGE(1)
9 CALL PLOTT(1,1,APLT,GPLT,KEP,1,0,0,0,0)
AMAX=APLT(KIP)
DO 60 K=1,KIP
IF(BPLT(K).GT.AMAX) GO TO 62
60 CONTINUE
KAP=KEP
GO TO 64
62 KAP=K+1
64 CALL PLOTT(2,1,BPLT,GIPLT,-KAP,1,-1,3,0,0)
CALL LFARGE(2)
CALL PLOTT(1,1,BPLT,GBPLT,KAP,1,0,0,0,0)

```

MAIN0580
 MAIN0590
 MAIN0600
 MAIN0610
 MAIN0620
 MAIN0630
 MAIN0640
 MAIN0650
 MAIN0660
 MAIN0670
 MAIN0680
 MAIN0690
 MAIN0700
 MAIN0710
 MAIN0720
 MAIN0730
 MAIN0740
 MAIN0750
 MAIN0760
 MAIN0770
 MAIN0780
 MAIN0790
 MAIN0800
 MAIN0810
 MAIN0820
 MAIN0830
 MAIN0840
 MAIN0850
 MAIN0860
 MAIN0870
 MAIN0880
 MAIN0890
 MAIN0900
 MAIN0910
 MAIN0920
 MAIN0930
 MAIN0940
 MAIN0950
 MAIN0960
 MAIN0970
 MAIN0980
 MAIN0990
 MAIN1000
 MAIN1010
 MAIN1020
 MAIN1030
 MAIN1040
 MAIN1050
 MAIN1060
 MAIN1070
 MAIN1080
 MAIN1090
 MAIN1100
 MAIN1110
 MAIN1120
 MAIN1130
 MAIN1140
 MAIN1150

59
 60
 61
 62
 63
 64
 65
 66
 67
 68
 69
 70
 71
 72
 73
 74
 75
 76
 77
 78
 79
 80
 81
 82
 83
 84
 85
 86
 87
 88
 89
 90
 91
 92
 93
 94
 95
 96
 97
 98
 99
 100
 101
 102
 103
 104
 105
 106
 107
 108
 109
 110
 111
 112
 113
 114
 115
 116

LISTING OF CONTROL CARD / INPUT DATA

```

IF((MV.EQ.MVM).AND.(NCASE.EQ.NCASES)) JUMP=2
CALL PLOTT(2,JUMP,BPLT,GIPLT,-KAP,1,-1,3,0,0)
5 CONTINUE
IF(NCASE.LT.NCASES) GO TO 3
RETURN
END

```

CARD NO

```

MAIN1160
MAIN1170
MAIN1180
MAIN1190
MAIN1200
MAIN1210
MAIN1220

```

LISTING OF CONTROL CARD / INPUT DATA

CARD NO

```

ACTION=BOH,SEQ=INIT0000
SUBROUTINE INITIAL(I,XXXX,SSSS,MMM,J)
IMPLICIT REAL*8(C,E,F,H,O-R,U-W,Y),COMPLEX*16(A,B,D,G,I,M,S,T,X,Z)
DIMENSION XXXX(1),SSSS(1)
REEL=I*MMM
ONEI=MMM
TB=DCMPLX(DCOS(ONEI),DSIN(ONEI))
TA=-I*TB
REXP=EXP(REEL)
C CHECK TO SEE THAT EXPONENTIAL FUNCTION DOESN'T UNDERFLOW:
IT WILL UNDERFLOW IF REEL.LT.-177.3.
IF (REEL.LT.-50.0) GO TO 12
TA=TA*REXP*REXP/TA
TB=TB*REXP*REXP/TB
12 IF (J.EQ.1) GO TO 13
XXXX(1)=TA+TB/MMM
XXXX(2)=-TB+3.0*XXXX(1)/MMM
CALL FORWAD(XXXX,MMM,10,0)
13 IF (COABS(MMM).LT.20.0) GO TO 16
CALL PSI910(SSSS(9),SSSS(10),MMM,TA,TB)
GO TO 17
16 CALL PSI(SSSS( 9),MMM, 9.35)
CALL PSI(SSSS(10),MMM,10.35)
SSSS(9)=2.0*REXP*SSSS(9)
SSSS(10)=2.0*REXP*SSSS(10)
17 CALL FORWAD(SSSS,MMM,10,1)
RETURN
END
INIT0000
INIT0010
INIT0020
INIT0030
INIT0040
INIT0050
INIT0060
INIT0070
INIT0080
INIT0090
INIT0100
INIT0110
INIT0120
INIT0130
INIT0140
INIT0150
INIT0160
INIT0170
INIT0180
INIT0190
INIT0200
INIT0210
INIT0220
INIT0230
INIT0240
INIT0250
INIT0260

```


LISTING OF CONTROL CARD / INPUT DATA

```

RACIN=BOTHS,SEC=PSIN0000
SUBROUTINE PSI910(X,Y,Z,S,C)
  C = PSI9.
  X = PSI10.
  Y = PSI10.
  Z = COMPLEX ARGUMENT.
  S = SIN(Z).
  C = COS(Z).
  COMPLEX*16 X,Y,Z,C,S,Q1,Q2,Q4,Q6,Q8
  Q1=1.0D+00/Z
  Q2=Q1*Q1
  Q4=Q2*Q2
  Q6=Q4*Q4
  Q8=Q6*Q4
  X=S*(45.0-1386.0*Q2+945945.0*Q4-16216200.0*Q6+34459425.0*Q8)*Q1
  1 -C*(1.0-990.0*Q2+135135.0*Q4-4729725.0*Q6+34459425.0*Q8)
  Y=-S*(1.0-1485.0*Q2+315315.0*Q4-18918900.0*Q6+310134925.0*Q8)
  1 -654729075.0*Q8*Q2)-C*(55.0-25740.0*Q2+2837835.0*Q4
  2 -91891800.0*Q6+654729075.0*Q8)*Q1
  RETURN
END

```

CARD NO

PSIN0000	1
PSIN0010	2
PSIN0020	3
PSIN0030	4
PSIN0040	5
PSIN0050	6
PSIN0060	7
PSIN0070	8
PSIN0080	9
PSIN0090	10
PSIN0100	11
PSIN0110	12
PSIN0120	13
PSIN0130	14
PSIN0140	15
PSIN0150	16
PSIN0160	17
PSIN0170	18
PSIN0180	19

LISTING OF CONTROL CARD / INPUT DATA

```

ACTION=BOH,SEC=FORW000
SUBROUTINE FORWARD(Z,N,IND)
  INC=0: FORWARDS RECURSION.
  INC=1: BACKWARDS RECURSION.
  N=0: GIVEN OF Q.
  Q(I)=FUNCTION VALUES: I = SUBSCRIPT.
    Q(1) AND Q(2) GIVEN IF IND=0.
    Q(N) AND Q(N-1) GIVEN IF IND=1.
  Z = COMPLEX ARGUMENT.
  C=1: INQ, E=0.1) GO TO 20
  C FORWARD
    GO TO 1: I=3,N
    10 Q(I)=Q(I-1)*Q(I-1)/Z-Q(I-2)
    RETURN
  C BACKWARDS
    20 Q(I)=Q(I+1)/Z-Q(I+2)
    30 Q(I)=Q(I+3)*Q(I+1)/Z-Q(I+2)
    RETURN
  END

```

CARD-20

FORW0000
FORW0010
FORW0020
FORW0030
FORW0040
FORW0050
FORW0060
FORW0070
FORW0080
FORW0090
FORW0100
FORW0110
FORW0120
FORW0130
FORW0140
FORW0150
FORW0160
FORW0170
FORW0180
FORW0190

1 2 3 4 5 6 7 8 9 10 11 12 13 14 15 16 17 18 19 20

LISTING OF CONTROL CARD / INPUT DATA

CARD NO

```

B ACTION= BOTH, SEQ= RECU0000
C SURROUTINE RECURR(V)
C RECURR COMPUTES ZETA PICCATI-BESSEL FUNCTIONS AND ALL FUNCTION
C DERIVATIVES OF ORDER V.
C ALSO COMPUTES THE V-TH ORDER SCATTERING COEFFICIENTS FOR COATED
C AND CORE SPHERES.
C IMPLICIT REAL*8(C,E,F,H,O,R,U,W,Y), COMPLEX*16(A,B,D,G,I,M,S,T,X,Z)
C REAL*8 N,A
C INTEGER*4 V,VP1,VM1
C COMMON /REX/ I,M1,M2,M1A,M2A,M2N,A,N,AN,BN,ALN,BLN,
C SN(10),DSN,XN(10),SM1A(10),
C XM2A(10),SM2N(10),
C ZN,SA(10),XA(10)
C IF(V.EQ.10) GO TO 35
C VP1=V+1
C DSN=VP1*SN(V)/N-SN(VP1)
C DSA=VP1*SA(V)/A-SA(VP1)
C DSM1A=VP1*SM1A(V)/M1A-SM1A(VP1)
C DSM2A=VP1*SM2A(V)/M2A-SM2A(VP1)
C DSM2N=VP1*SM2N(V)/M2N-SM2N(VP1)
C DXN=VP1*XN(V)/N-XN(VP1)
C DXA=VP1*XA(V)/A-XA(VP1)
C DXM2A=VP1*XM2A(V)/M2A-XM2A(VP1)
C DXM2N=VP1*XM2N(V)/M2N-XM2N(VP1)
C GO TO 37
35 VM1=V-1
C DSN=-V*SN(V)/N+SN(VM1)
C DSA=-V*SA(V)/A+SA(VM1)
C DSM1A=-V*SM1A(V)/M1A+SM1A(VM1)
C DSM2A=-V*SM2A(V)/M2A+SM2A(VM1)
C DSM2N=-V*SM2N(V)/M2N+SM2N(VM1)
C DXN=-V*XN(V)/N+XN(VM1)
C DXA=-V*XA(V)/A+XA(VM1)
C DXM2A=-V*XM2A(V)/M2A+XM2A(VM1)
C DXM2N=-V*XM2N(V)/M2N+XM2N(VM1)
C ZN=SN(V)+1*DN(V)
C ZN=DSN+1*DXN
C ZN=DSM1A+1*DSM1A(V)
C ZN=DSM2A+1*DSM2A(V)
C ZN=DSM2N+1*DSM2N(V)
C ZN=DXN+1*DXN
C ZN=DSM1A(V)-M2*SM2A(V)*DSM1A
C ZN=DSM2A(V)-M2*SM2A(V)*DSM1A
C ZN=DSM2N(V)-M2*SM2N(V)*DSM1A
C ZN=DXN+1*DXN
C ZN=DSM1A(V)-M1*SM2A(V)*DSM1A
C ZN=DSM2A(V)-M1*SM2A(V)*DSM1A
C ZN=DSM2N(V)-M1*SM2N(V)*DSM1A
C ZN=DXN+1*DXN
C ZN=DSM1A(V)-M1*SM2A(V)*DSM1A
C ZN=DSM2A(V)-M1*SM2A(V)*DSM1A
C ZN=DSM2N(V)-M1*SM2N(V)*DSM1A
C ZN=DXN+1*DXN
C SCATTERING COEFFICIENTS FOR COATED SPHERE.
C AN=(A1*AF2-AF3*AF4)/(A1*AF5-AF3*AF6)
C BN=(B1*BF2-BF3*BF4)/(B1*BF5-BF3*BF6)
C SCATTERING COEFFICIENTS FOR CORE SPHERE.
C ALN=(SA1V)*DSM1A-M1*SM1A(V)*DSM1A/(M1*ZA*DSM1A-SM1A(V)*DZA)
C BLN=(M1*SA1V)*DSM1A-M1*SM1A(V)*DSM1A/(M1*ZA*DSM1A-SM1A(V)*DZA)
C RETURN
C END

```

RECU0000
 RECU0010
 RECU0020
 RECU0030
 RECU0040
 RECU0050
 RECU0060
 RECU0070
 RECU0080
 RECU0090
 RECU0100
 RECU0110
 RECU0120
 RECU0130
 RECU0140
 RECU0150
 RECU0160
 RECU0170
 RECU0180
 RECU0190
 RECU0200
 RECU0210
 RECU0220
 RECU0230
 RECU0240
 RECU0250
 RECU0260
 RECU0270
 RECU0280
 RECU0290
 RECU0300
 RECU0310
 RECU0320
 RECU0330
 RECU0340
 RECU0350
 RECU0360
 RECU0370
 RECU0380
 RECU0390
 RECU0400
 RECU0410
 RECU0420
 RECU0430
 RECU0440
 RECU0450
 RECU0460
 RECU0470
 RECU0480
 RECU0490
 RECU0500
 RECU0510
 RECU0520
 RECU0530
 RECU0540
 RECU0550
 RECU0560
 RECU0570

LISTING OF CONTROL CARD / INPUT DATA

CARD NO

```

ACTION=0TH,SECC=SUMS0000
SUBROUTINE SUMS0(G1,G2,A,KMIN,KMAX,N)
C SUMSC COMPUTES RMS% DEVIATION BETWEEN TWO GAIN CURVES, G1 AND G2,
C OVER THE RANGE OF KA FROM KA(KMIN) TO KA(KMAX).
C N=1: G1 = COATED SPHERE, G2 = CORE SPHERE.
C N=2: G1 = COATED SPHERE, G2 = PERFECTLY CONDUCTING SPHERE.
C DIMENSION G1(1),G2(1),A(1)
S=0.0
DO 200 I=KMIN,KMAX
200 S=((G1(I)-G2(I))/G2(I))*2+S
SE=SQRT(G1(KMAX-KMIN+1))/100.0
GO TO (1,2),N
1 PRINT 1007,S,A(KMIN),A(KMAX)
1007 FORMAT(1H,,'RMS % DEVIATION BETWEEN COATED AND UNCOATED CORE SPHER',
1E,,'E12.6/1H,
2 'OVER THE RANGE K*RA = ',E12.6,' TO ',E12.6/)
RETURN
2 PRINT 1008,S,A(KMIN),A(KMAX)
1008 FORMAT(1H,,'RMS % DEVIATION BETWEEN COATED AND PERFECTLY CONDUCTING',
1S SPHERE = ',E12.6/1H,
2 'OVER THE RANGE K*RB = ',E12.6,' TO ',E12.6/)
RETURN
END
SUMS0000
SUMS0010
SUMS0020
SUMS0030
SUMS0040
SUMS0050
SUMS0060
SUMS0070
SUMS0080
SUMS0090
SUMS0100
SUMS0110
SUMS0120
SUMS0130
SUMS0140
SUMS0150
SUMS0160
SUMS0170
SUMS0180
SUMS0190
SUMS0200
SUMS0210
SUMS0220

```

1
2
3
4
5
6
7
8
9
10
11
12
13
14
15
16
17
18
19
20
21
22

LISTING OF CONTROL CARD 7 INPUT DATA

```

BACTCN=BOTH,SEC=COAL0000
SUBROUTINE COATM2(N)
C COATM2 COMPUTES CORE AND COATING REFRACTIVE INDICES.
C COMPLEX LINEAR DISPERSION FROM SLOPE AND INTERCEPT.
C WL = WAVELENGTH.
FCOATR = COATING REFRACTIVE INDEX.
FCORER = CORE REFRACTIVE INDEX.
IMPLICIT REAL*8(A-E,O-Z),COMPLEX*16(F-H)
READ 1001,RM1,SRM1,EM1,SEM1,RM2,SRM2,EM2,SEM2
1001 FORMAT(4(7X,D13.5))
1002 FORMAT(1H //1H,M1 = (RM1 + SRM1*WL, EM1 + SEM1*WL)/1H,
2 RM1 = '.E13.6.5X',SRM1 = '.E13.6.5X',EM1 = '.E13.6.5X',
3 SEM1 = '.E13.6//1H,
4 RM2 = (RM2 + SRM2*WL, EM2 + SEM2*WL)/1H,
5 RM2 = '.E13.6.5X',SRM2 = '.E13.6.5X',EM2 = '.E13.6.5X',
6 SEM2 = '.E13.6//)
RETURN
ENTRY COAT1(FCOATR,WL)
FCOATR=DCMPLX(RM2+SRM2*WL,EM2+SEM2*WL)
RETURN
ENTRY COREM1(FCORER,WL)
FCORER=DCMPLX(RM1+SRM1*WL,EM1+SEM1*WL)
RETURN
END

```

CARD NO

COAL0000	1
COAL0010	2
COAL0020	3
COAL0030	4
COAL0040	5
COAL0050	6
COAL0060	7
COAL0070	8
COAL0080	9
COAL0090	10
COAL0100	11
COAL0110	12
COAL0120	13
COAL0130	14
COAL0140	15
COAL0150	16
COAL0160	17
COAL0170	18
COAL0180	19
COAL0190	20
COAL0200	21
COAL0210	22
COAL0220	23

LISTING OF CONTROL CARD / INPUT DATA

CARD NO

```

ACTION=BOH,SEQ=COAS0000
SUBROUTINE COATM2(N)
COATM2 COMPUTES CORE AND COATING REFRACTIVE INDICES.
COMPLEX LINEAR DISPERSION FROM SLOPE AND INTERCEPT FOR THE CORE.
TABLE LOOKUP FOR COMPLETE ABSORPTION BAND OF COATING.
AL = WAVELENGTH.
FCOATR = COATING REFRACTIVE INDEX.
FCORER = CORE REFRACTIVE INDEX.
A = REAL PART OF INDEX FOR COATING.
B = FREQUENCIES FOR REAL PART OF INDEX OF COATING.
C = FREQUENCIES FOR IMAGINARY PART OF INDEX OF COATING.
D = MINUS THE IMAGINARY PART OF THE REFRACTIVE INDEX FOR COATING.
IMPLICIT REAL*8(E,J-Z),COMPLEX*16(F-H),REAL*4(A-D)
DIMENSION A(90),B(90),C(90),D(90)
DATA A/3.1,0.77,3.087,3.12,3.136,3.192,3.240,3.385,3.578,3.905,
1 4.158,4.530,4.826,5.274,5.628,5.007,4.517,3.376,4.086,4.681,
2 5.453,6.077,6.810,7.545,8.374,9.219,9.798,10.42,11.33,11.97,
3 12.80,14.21,6.870,5.416,3.813,2.202,1.315,0.723,0.118,0.063,
4 0.161,0.467,0.878,1.828,2.396,3.044,3.299,3.988,4.395,5.066,
5 5.605,6.510,7.022,7.862,8.341,9.263,9.772,10.68,11.19,11.95,
6 6.672,5.218,4.020,2.646,1.686,1.925,0.444,0.302,0.437,
7 0.643,1.11,2.058,1.631,0.450,0.107,0.013,0.013,0.013,0.016,
8 0.187,0.529,0.736,0.911,1.081,1.214,1.346,1.477,1.627,1.688,
9 3.707,
DATA B/300.0,200.0,100.0,90.91,83.33,66.67,33.21,29.73,28.18,
1 27.02,26.72,26.38,26.15,26.01,25.82,25.59,25.19,24.72,24.43,
2 23.98,23.58,23.29,23.14,23.00,22.83,22.65,22.53,22.30,22.06,
3 21.83,21.74,21.53,21.34,21.09,20.86,20.61,20.30,19.90,19.40,
4 18.86,18.47,18.16,17.97,17.81,17.72,17.65,17.55,17.44,17.36,
5 17.27,17.05,16.85,16.73,16.41,16.06,15.91,15.85,15.77,15.71,
6 15.61,15.5,15.45,15.31,15.17,14.96,14.63,14.35,14.01,13.64,
7 13.29,12.88,12.51,12.18,11.87,11.54,11.19,10.76,10.05,8.998,
8 8.522,8.274,8.009,7.337,7.024,6.728,5.478,5.384,5.299,5.015,
9 3.948,
DATA C/3.0E-3,3.3,501E-3,6.923E-3,7.379E-3,7.958E-3,1.008E-2,
1 1.578E-1,1.085E-1,3.287E-1,2.465E-1,1.925E-1,1.423E-1,1.052E-1,5.90E-1,
2 1.345E-1,0.814E-1,5.062E-1,3.083E-1,1.437E-1,0.378E-1,0.189E-1,
3 6.443E-1,1.114E-1,1.742E-1,0.303E-1,0.189E-1,0.240E-1,0.192E-1,
4 7.574E-1,0.5638E-1,1.512E-1,1.474E-2,1.052E-1,3.057E-1,5.358E-1,
5 8.876E-1,1.3517E-1,1.345E-1,0.200E-1,0.394E-1,0.558E-1,0.980E-1,1.251E-1,
6 8.810E-1,1.9451E-1,0.7366E-1,0.4655E-1,0.408E-1,0.470E-1,0.734E-1,
7 1.073E-1,1.9451E-1,0.7366E-1,0.4655E-1,0.408E-1,0.470E-1,0.734E-1,
8 2.912E-1,0.3208E-1,0.247E-1,0.2712E-1,0.247E-1,0.2712E-1,0.247E-1,
9 3.402E-1,0.3182E-1,0.2968E-1,0.2968E-1,0.2968E-1,0.2968E-1,0.2968E-1,
1 1.798E-1,0.1591E-1,0.1407E-1,0.1705E-1,0.9665E-1,1.7265E-1,4.701E-1,
2 6.327E-2,2.827E-2,1.841E-2,1.158E-2,2.825E-2,3.866E-2,5.119E-3,
3 3.409E-3,1.1717E-3,2.338E-5,1.374E-5,7.260E-6,2.559E-6,1.014E-6,
4 1.001E-6,1.001E-6,1.001E-6,1.001E-6,1.001E-6,1.001E-6,1.001E-6,
5 1.001E-6,1.001E-6,1.001E-6,1.001E-6,1.001E-6,1.001E-6,1.001E-6,
6 1.001E-6,1.001E-6,1.001E-6,1.001E-6,1.001E-6,1.001E-6,1.001E-6,
7 1.001E-6,1.001E-6,1.001E-6,1.001E-6,1.001E-6,1.001E-6,1.001E-6,
8 1.001E-6,1.001E-6,1.001E-6,1.001E-6,1.001E-6,1.001E-6,1.001E-6,
9 1.001E-6,1.001E-6,1.001E-6,1.001E-6,1.001E-6,1.001E-6,1.001E-6,
1001 FORMAT(1H,013.6)
1002 FORMAT(1H,013.6)

```

LISTING OF CONTROL CARD / INPUT DATA

```

1  'RM1 = '.E13.6.SX.'SRM1 = '.E13.6.SX.'EM1 = '.E13.6.SX.
2  'SEM1 = '.E13.6//1
   RETURN
   ENTRY COAT1(FCOATR,WL)
   AXL=WL
   DO 10 I=1,90
   IF(B(I).LT.AXL) GO TO 12
   CONTINUE
10  EA=A(I-1)+(A(I)-A(I-1))*(AXL-B(I-1))/(B(I)-B(I-1))
12  DO 20 I=1,90
   IF(C(I).LT.AXL) GO TO 22
   CONTINUE
20  ED=D(I-1)+(D(I)-D(I-1))*(AXL-C(I-1))/(C(I)-C(I-1))
22  FCOATR=DCMPLX(EA,-ED)
25  RETURN
   ENTRY COREM1(FCORER,WL)
   FCORER=DCMPLX(RM1+SRM1*WL,EM1+SEM1*WL)
   RETURN
   END

```

CARD NO

COAS0580 59
 COAS0590 60
 COAS0600 61
 COAS0610 62
 COAS0620 63
 COAS0630 64
 COAS0640 65
 COAS0650 66
 COAS0660 67
 COAS0670 68
 COAS0680 69
 COAS0690 70
 COAS0700 71
 COAS0710 72
 COAS0720 73
 COAS0730 74
 COAS0740 75
 COAS0750 76
 COAS0760 77

CARD NO

CCAC00000
CCAC00010
CCAC00020
CCAC00030
CCAC00040
CCAC00050
CCAC00060
CCAC00070
CCAC00080
CCAC00090
CCAC00100
CCAC00110
CCAC00120
CCAC00130
CCAC00140
CCAC00150
CCAC00160
CCAC00170
CCAC00180
CCAC00190
CCAC00200
CCAC00210
CCAC00220
CCAC00230
CCAC00240
CCAC00250
CCAC00260
CCAC00270
CCAC00280
CCAC00290
CCAC00300
CCAC00310
CCAC00320
CCAC00330
CCAC00340
CCAC00350
CCAC00360
CCAC00370
CCAC00380
CCAC00390
CCAC00400
CCAC00410
CCAC00420
CCAC00430
CCAC00440
CCAC00450
CCAC00460
CCAC00470
CCAC00480
CCAC00490
CCAC00500
CCAC00510
CCAC00520
CCAC00530

LISTING OF CONTROL CARD / INPUT DATA

```

3 ACTION=BOH,SELEFAR0000
SURROUTINE LFARGE(NCK)
DIMENSION X(1),Y(1),TITLE(40),LABELX(15),LABELY(15),LABELG(10),
1 LABELH(10)
EQUIVALENCE (TITLE(1),LABELX(1)),(TITLE(15),LABELY(1)),(TITLE(31),
1 LABELG(1))
DATA BLANK/ ' ',CS/0.1/ SET NCK=1 THE FIRST TIME THROUGH.
C NCK IS THE PLOT INDICATOR. SET NCK TO ANY INTEGER .GE. 2 AFTER THAT UNLESS NENDPL HAS BEEN
C SET TO 2 ON THE PREVIOUS GRAPH. IN WHICH CASE YOU MUST SET NCK=1.
C READ 10,LABELX,LABELY,LABELG,LABELH
READ 10,FORMAT(15A4/15A4/10A4,10A4)
READ 20,XMIN,XMAX,SIDEX,XFCT,YMIN,YMAX,SIDEY,YFCT
20 FORMAT(8G10)
IF(NCK.GE.2) GO TO 25
CALL PLOT(21)
25 CALL PLOT(0.0,0.8,-3)
CALL OFACT(XFCT,YFCT)
C PRINT GRAPH TITLE.
1=40
70 IF(LABELH(1/4).NE.BLANK) GO TO 71
1=1-4
IF(1.NE.0) GO TO 70
GO TO 72
71 XTITLE=(SIDEX-1*0.19)/2.0
72 1=40
100 IF(TITLE(30+1/4).NE.BLANK) GO TO 101
1=1-4
IF(1.NE.0) GO TO 100
GO TO 102
101 XTITLE=(SIDEX-1*0.19)/2.0
102 1=60
C DRAW X-AXIS.
DO 103 1=1,14
IF(TITLE(16-11).NE.BLANK) GO TO 104
103 1=1+4
104 CALL AXIS(0.0,0.0,0.0,TITLE(1),1,SIDEX,0.0,XMIN,(XMAX-XMIN)/SIDEX)
C DRAW Y-AXIS.
1=60
DO 105 1=1,14
IF(TITLE(31-11).NE.BLANK) GO TO 106
105 1=1-4
106 CALL AXIS(0.0,0.0,0.0,TITLE(16),1,SIDEY,90.0,YMIN,(YMAX-YMIN)/SIDEY)
RETURN
ENTRY PLOTT(NTG,NENDPL,X,Y,ISZ,INC,KAP,INTEG,CVAL)
NENDPL IS THE ENDPLOT INDICATOR. SET NENDPL=1 UNTIL THE FINAL
GRAPH AND THEN SET NENDPL=2.
NTG IS THE NEXT GRAPH INDICATOR. SET NTG=2 IF THIS IS
THE LAST GRAPH ON THIS SET OF AXES OR IF NENDPL=2.
X AND Y ARE THE DATA ARRAYS TO BE PLOTTED ON THE X AND Y AXES.
1=1 NPTS BE THE NUMBER OF POINTS PLOTTED; THEN,
ISZ IS THE DIMENSION OF THE X AND Y ARRAYS *WHICH MUST BE OF THE
FORM: NPTS*INC+1.
IF KAP IS NOT ZERO LOOK IN THE MANUAL BECAUSE YOU HAVE TO BE CAREFUL
THAT THE X AND Y ARRAYS HAVE DIMENSIONS OF NPTS*INC+1 AND
XMIN WOULD BE IN POSITION ISZ-INC.

```

CARD NO

1 LFAR0000
2 LFAR0010
3 LFAR0020
4 LFAR0030
5 LFAR0040
6 LFAR0050
7 LFAR0060
8 LFAR0070
9 LFAR0080
10 LFAR0090
11 LFAR0100
12 LFAR0110
13 LFAR0120
14 LFAR0130
15 LFAR0140
16 LFAR0150
17 LFAR0160
18 LFAR0170
19 LFAR0180
20 LFAR0190
21 LFAR0200
22 LFAR0210
23 LFAR0220
24 LFAR0230
25 LFAR0240
26 LFAR0250
27 LFAR0260
28 LFAR0270
29 LFAR0280
30 LFAR0290
31 LFAR0300
32 LFAR0310
33 LFAR0320
34 LFAR0330
35 LFAR0340
36 LFAR0350
37 LFAR0360
38 LFAR0370
39 LFAR0380
40 LFAR0390
41 LFAR0400
42 LFAR0410
43 LFAR0420
44 LFAR0430
45 LFAR0440
46 LFAR0450
47 LFAR0460
48 LFAR0470
49 LFAR0480
50 LFAR0490
51 LFAR0500
52 LFAR0510
53 LFAR0520
54 LFAR0530
55 LFAR0540
56 LFAR0550
57 LFAR0560
58 LFAR0570

LISTING OF CONTROL CARD 7 INPUT DATA

```

C      INC IS THE INCREMENT USED IN SCANNING THROUGH THE ARRAYS.
C      KAP IS THE MODE INDICATOR.
C      IF KAP=LT.0, A SYMBOL IS SPOTTED EVERY K*INC-TH POINT.
C      IF KAP=0, A LINE IS DRAWN CONNECTING EVERY INC-TH POINT.
C      IF KAP=GT.0, A LINE IS DRAWN CONNECTING EVERY INC-TH POINT.
C      AND A SYMBOL OF AN INDICATOR NUMBER PRINTED AT THE END OF
C      EACH GRAPH.
C      CVAL IS THE SYMBOL INDICATOR. IT MAY BE AN INTEGER FROM 0 TO 13.
C      SEE THE MANUAL FOR THE KEY TO THE SYMBOLS.
C      ISGN=ISZ/IABS(ISZ)
C      ISZ=IABS(ISZ)
C      X(ISZ-INC)=XMIN
C      X(ISZ)=(XMAX-XMIN)/SIDEY
C      Y(ISZ-INC)=YMIN
C      Y(ISZ)=(YMAX-YMIN)/SIDEY
C      IIZ=-(ISZ-INC-1)*ISGN
C      IIZ=IABS(IIZ)
C      PREVENT OUT-OF-BOUNDS VALUES OF Y-COORDINATE.
C      DO 110 I=1,IIZ
C      IF(Y(I).GT.YMAX) Y(I)=YMAX
C      IF(Y(I).LT.YMIN) Y(I)=YMIN
C      110 CONTINUE
C      DRAW GRAPH.
C      152 CALL FLINEX(X,Y,IIZ,INC,KAP,INTE0)
C      IX=ISZ/4+111
C      IY=ISZ/4+111
C      I11=I11+2
C      ND=2
C      IF (ABS(CVAL).GT.99.0) ND=-1
C      IF (ABS(CVAL).LT.(1.0).AND.ABS(CVAL).GT.(0.0001))
C      ND=3-IF(X(ALOG10(ABS(CVAL))))
C      PRINT NUMBER, CVAL, ON GRAPH.
C      CALL NUMBER(X(I11)/X(I12),Y(I11)/Y(I12),CS,CVAL,0.0,ND)
C      160 IF (NTG.EQ.2) GO TO 200
C      RETURN
C      200 CALL DFACT(1.0,1.0)
C      CALL PLOT(SIDEY+5.0,-0.8,-3)
C      IF (NENDPL.EQ.2) GO TO 250
C      RETURN
C      250 CALL ENPLT(-4.0,0.0)
C      RETURN
C      END

```

CARD NO

59
60
61
62
63
64
65
66
67
68
69
70
71
72
73
74
75
76
77
78
79
80
81
82
83
84
85
86
87
88
89
90
91
92
93
94
95
96
97
98
99
100
101